Control Allocation of Flexible Aircraft for Load Alleviation

by

John H. Hansen

A dissertation submitted in partial fulfillment
of the requirements for the degree of
Doctor of Philosophy
(Aerospace Engineering)
in the University of Michigan
2021

Doctoral Committee:

Professor Carlos E. S. Cesnik, Co-Chair
Professor Ilya V. Kolmanovsky, Co-Chair
Professor Bogdan Epureanu
Professor Daniel J. Inman

John H. Hansen

hansenjh@umich.edu

ORCID iD: 0000-0001-7986-3172

2021

ACKNOWLEDGMENTS

I would like to thank my co-advisors, Professors Carlos E. S. Cesnik and Ilya V. Kolmanovsky for their support and guidance throughout this process. Thank you to my fellow graduate students and post-doctoral researchers for helping me with my questions, especially Dr. Molong Duan, for your ideas, insights, and encouragement for my thesis research.

Thank you to my parents, who encouraged me to grow and learn throughout my life. Thank you to my in-laws, for accepting me into their family and especially to my mother-in-law for stepping in to help our family while my wife received her kidney transplant. Thank you, also, to my sister-in-law's family, who welcomed us to move-in next door and made our entire time in Ann Arbor more enjoyable and adventurous.

My deepest thanks go to my wife, who always embraced me with love and compassion. You supported me through hard times and inspired me to do my best in this program. To my children, I am forever grateful for your love and support, which enriches my life in countless ways.

TABLE OF CONTENTS

CHAPTER

LIST OF FIGURES

LIST OF TABLES

LIST OF APPENDICES

LIST OF ABBREVIATIONS

CA	Control Allocator
CFR	Code of Federal Regulations
GLA	Gust Load Alleviation
GTA	Generic Transport Aircraft
INS	Inertial Navigation System
LA	Load Alleviation
LIDAR	Light Detection and Ranging
LPV	Linear Parameter-Varying
LTI	Linear Time-Invariant
MLA	Maneuver Load Alleviation
MOPs	Measures of Performance
MPC	Model Predictive Control
MVS	Maneuver Vertical Stretched
PI	Proportional-Integral
P/PI	Proportional/Proportional-Integral
QP	Quadratic Programming
UM/NAST	University of Michigan's Nonlinear Aeroelastic Simulation Toolbox

ABSTRACT

As wing designs aim for higher aerodynamic efficiency, the underlying aircraft structure becomes more flexible, requiring additional features to alleviate the loads encountered from gusts and maneuvers. While alleviating loads, it is desirable to minimize the deviations from the original flight trajectory.

In this work, a dynamic control allocation method which exploits redundant control effectors for maneuver and gust load alleviation is proposed for flexible aircraft. The control architecture decouples the two objectives of load alleviation and rigid body trajectory tracking by exploiting the null space between the input and the rigid body output. A reduced-dimensional null space input is established, which affects the flexible output (but not the rigid body output) when passed through a null space filter to generate incremental control signals. This null space input is determined to maintain the flexible output of the aircraft within specified values, thereby achieving load alleviation.

A receding horizon approach to generate the trajectory of the null space input is developed based on linear aircraft models. This receding horizon approach then informs a model predictive control-based control allocator function which can be used as an add-on scheme to a nominal controller. Numerical simulations are used to illustrate the operation of this load alleviation system based on linear models, linear parameter-varying models, and nonlinear models. It is shown that the proposed load alleviation system can successfully avoid the violation of load bounds in the presence of both gust disturbances and maneuvers and with minimal effect on the trajectory tracking performance.

A case study to characterize the proposed load alleviation system identified limits of its applicability to nonlinear aircraft and resulted in recommendations for its design parameters. The load alleviation system developed and demonstrated in this work can be applied to aircraft with wing flexibility high enough that the vertical wingtip deflection is around 28-34% of half-span in cruise and the first out-of-plane bending frequency is around 1.05-1.15 Hz. The case study also showed that a preview horizon of 1-2 seconds provides a good compromise for handling both low-frequency maneuvers and high-frequency gust disturbances.

CHAPTER 1

Introduction

An aircraft in flight uses a balance of four principal forces to maintain stable flight: lift, weight, thrust, and drag. Weight is a result of gravitational forces between the aircraft and the earth and is always directed toward the earth. Thrust can be produced by propellers or jets to propel the aircraft forward and its direction is aligned with the mounting of the thrust devices. Forward airspeed produces aerodynamic forces of lift and drag on the aircraft. Lift is directed normal to the surface of the wing and drag is directed opposite of the airspeed direction. As aircraft are designed for increased fuel efficiency, high aspect ratio wings and lightweight structures emerge as key features. The higher aspect ratio increases lift and reduces induced drag. A reduction of drag means that less thrust (and less fuel) is needed to maintain airspeed in flight. Using a lightweight structure results in less overall weight for the aircraft. A reduction of weight means that less lift is needed to keep the aircraft airborne. However, these key features often result in increased structural flexibility.

An aircraft maneuvers in flight by intentionally manipulating the balance of the four principal forces and three principal moments, aligned with the roll-, pitch-, and yaw-axes. For example, deflecting a control surface in the tail can produce a pitching moment to raise the nose of the aircraft, increasing the lift produced by the wings resulting in an increase in altitude. Maneuvering performance is a distinguishing feature of an aircraft and is defined to meet mission objectives for the aircraft through its design and flight controllers.

Gust disturbances also influence the forces and moments of the aircraft in flight, in an unintentional manner. A gust disturbance represents transient shifts in the freestream velocity of the air mass through which the aircraft is flying. These shifts are generally changes in the direction of the freestream velocity. For example, an upward gust disturbance would increase the angle of attack between the wind and the orientation of the airfoil of the wing, which would temporarily increase the lift, altering the flight dynamics.

A key challenge arising from the high-efficiency design is the higher resulting lift forces (loads) when the aircraft undergoes aggressive flight maneuvers or encounters gusts. The lightweight structure of the aircraft may have a lower threshold for deformation or fatigue which increases the probability of structural failure in flight.

The overall lifting force produced by a wing typically has an elliptical shape along the span of the wing, as seen by the yellow shape in Fig. 1.1. The lifting force is highest at the root of the wing and decreases slowly when moving toward the wing tip. Closer to the wing tip, the lifting forces decreases quickly to a value of zero lift at the tip of the wing. This lifting force deforms the wing, bending it upward, and produces a bending moment at the root of the wing, where the structure is attached to the fuselage (for a conventional aircraft design).

Existing methods to alleviate the maneuver and gust loads on aircraft are referred to as Maneuver Load Alleviation (MLA) and Gust Load Alleviation (GLA). One common technique for alleviating wing loads is to manipulate the shape of the lifting forces along the span of the wing [1]. The lifting forces near the root of the wing can be increased while the lifting forces near the wing tip are decreased. This adjustment of forces can be balanced so that the same total lifting force results, but that the effective location of that force is closer to the wing root, as seen by the blue shape in Fig. 1.1. This results in an overall reduction of the wing root bending moment and a reduction

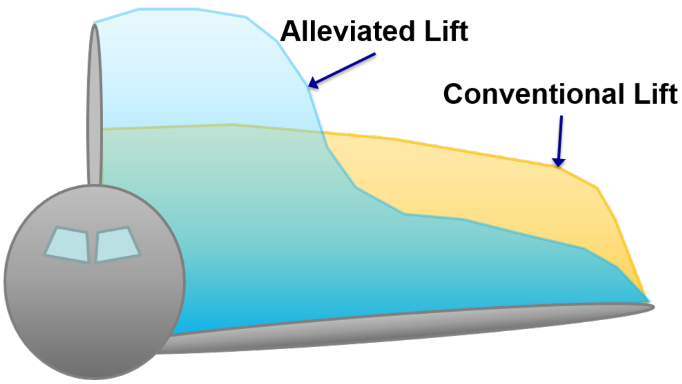

Figure 1.1: Portrayal of the load alleviation technique to shift the lifting forces along the span of the wing

of the stress at the wing root. Therefore, load alleviation may allow maneuvers which otherwise would have exceeded the critical stress limits of the structure. Load alleviation not only prevents structural failure from overloading, it can also reduce fatigue effects. This decreases the frequency of required maintenance and structural inspection, decreasing the operational cost of the aircraft over its life cycle.

While load alleviation helps to preserve the structural integrity of an aircraft and is the primary objective of this work, a secondary objective is to maintain the aircraft maneuvering performance and trajectory tracking as designed, according to the aircraft mission. Fulfilling the primary objective while ignoring the secondary objective may result in adverse effects on the maneuvering performance and trajectory tracking, further leading to a degradation of handling qualities or even mission failure.

1.1 Previous Work

This section provides a review of previous research efforts which are relevant to the goal of load alleviation. These efforts show that there are many methods to approach this situation, including both hardware and software. Each of these methods has their own qualities and benefits.

1.1.1 Hardware Methods of Load Alleviation

With respect to airworthiness, considerations for wing loads began to appear between the 1930's to 1950's [2]. Patents for MLA systems were granted as early as 1949 [3] and additional studies of MLA and GLA through the 1970's [1, 4] allowed for integration of such systems in operational aircraft. Early operational examples of LA methods involving additional hardware or dedicated control surfaces include the fuselage mode control system on the B-1 Lancer and the closed-loop GLA system on the B-2 Spirit [5].

More recently, Guo et al. [6] proposed a design for a passive gust alleviation device at the wing tip of a high altitude sensor aircraft in 2012. The device consisted of a rigid wing section mounted to each wing tip by means of a torque spring and a rotation shaft. Setting the rotation shaft axis in front of the aerodynamic center, the device twists nose down to alleviate the aerodynamic force in response to a gust load. Optimization of the design variables showed that a 17% reduction of wingtip oscillation could be achievable. Later in 2016, a wind tunnel model based on this design was tested with a scaled model of the wing for the sensor aircraft, showing that a maximum 9.4% reduction of wingtip oscillation can be achieved [7]. When coupled with aeroelastic tailoring of the wing, a maximum 28.5% reduction could be achieved.

Fonte et al. [8] proposed a wing tip device with a trailing edge control surface for active control of loads due to maneuvers and gusts. The control surface deflections are optimized to reduce loads in trim and provide a general load reduction for maneuvers. The GLA controller reduces wing loads by more than the increase from the addition of the wing tip device. Therefore, their active wingtip extension can be a technique to increase the wing span and fuel efficiency without affecting the wing internal loads.

Nguyen et al. [9, 10, 11] proposed a variable camber flap control system installed along almost the entire span of the wing to optimize lift and drag performance through all phases of flight. This same system has been developed over several years, with applications in load alleviation [12], flutter suppression [13], and ride quality [14]. The design has also been used to construct a wind tunnel model [15] which has been tested at the University of Washington [16].

Including such hardware solutions in the design phase is preferred, instead of the sustainment phase of an aircraft life cycle. Adding new hardware to existing aircraft requires structural redesign, additional manufacturing and testing, which may come at high cost. Therefore, software solutions exploiting the existing control effectors are appealing.

1.1.2 Software Methods of Load Alleviation

Early software methods of MLA systems symmetrically deflected the wing control surfaces (e.g., ailerons, flaps) based on aircraft normal acceleration to reduce structural loads [1]. The Active Lift Distribution Control System designed to reduce structural fatigue of the wings on the C-5 Galaxy is an early example of a software-based MLA system [17]. An MLA efficiency study by Yang et al. [18] found that the efficient deflection is down for inboard control surfaces and up for outboard ones. This moves the wing load toward the fuselage of a conventional transport aircraft, reducing the bending moment at the root of the wing. Similar to MLA, GLA also uses the control surfaces to reduce the load, but it may not lead to symmetric deflections. Also, GLA typically requires a faster response to unanticipated dynamic loads [19]. To enable more effective use of multiple control surfaces for LA, advanced control approaches have been proposed.

Dillsaver et al. [20] proposed a GLA system for very flexible aircraft using linear quadratic gaussian control techniques. This system reduced the peak wing curvatures by an average of 47% using numerical simulations of the aircraft response to a stochastic gust. The system also worked with a pitch controller to track commands while simultaneously minimizing wing deflections, reducing peak curvatures by an average of 56%. For cases with specific constraints on the wing deflection, a reference governor was recommended.

Li et al. [21] proposed an adaptive MLA system which used two recurrent neural networks. One neural network was used to identify the aeroelastic model of the aircraft and its open loop response for a given maneuver. The other neural network was used to alleviate the wing-root bending moment while maintaining the same response for angle of attack and load factor. This was accomplished by a cost function which included penalties for differences in the rigid body response and for control surface deflection. The tuned system achieved as much as a 49% reduction in bending moment, with minimal changes to the rigid body trajectory during the maneuver.

Yagil et al. [22] used a two-step approach to GLA by first constraining wing deformation of a highly flexible aircraft to within linear limits in steady trimmed flight. This was accomplished by determining optimal control surface deflections for steady flight while also allowing sufficient control margin for an active controller. The second step used $\mathcal{H}_\infty$ loop shaping for the control of the dynamic response to gusts.

Model Predictive Control (MPC) is another control design method which directly uses an explicit and separately identifiable model of the system to predict the dynamics of the system from a current state for a relatively short time horizon [23]. This prediction helps provide context to choose the best control action for the current time (e.g., through optimization by minimizing a cost function). This design also provides a systematic way to explicitly handle constraints on inputs and states of the system [24], which is of particular interest for the purposes of LA. Additional benefits and challenges of using MPC for LA are presented in [25], along with a thorough discussion of previous work.

Haghighat et al. [26] proposed an MPC framework with a unified objective of aircraft stabilization and GLA. This framework showed the potential of MPC to reduce loads caused by gust disturbances, but did not use preview information of the disturbance nor explicit load constraints.

Wang et al. [27] developed a novel model order reduction method to represent key structural and flight dynamics of a flexible aircraft using only 7 states (99.5% decrease from 1566 states). This nonlinear reduced order model was then used for nominal predictions to support a nonlinear MPC control design for GLA. The large reduction of the aircraft model in [27] facilitates running this nonlinear MPC control system in real time.

Early approaches to GLA used gust angle measurements at the nose of the aircraft in order to tailor the aircraft response to the gust [28]. More recently, Light Detection and Ranging (LIDAR) devices have been proposed to measure atmospheric disturbances meters ahead of an aircraft in order to provide a forecast for the control system. An early flight test campaign of such a system observed reliable gust measurements up to 50 meters in front of the aircraft [29]. Giesseler et al. [24] showed that employing LIDAR with a 50-meter measurement capability can effectively support MPC implementation. Their proposed system significantly reduced loads at relevant structural stations while respecting constraints on input ranges and rates. Recent advances such as the direct detection pulsed doppler LIDAR have helped increase gust measurement ranges up to 300 meters in front of the aircraft [30, 31].

The above methods either allow or ignore the effects of the load alleviation system on the flight trajectory tracking. Therefore, an alternate approach for handling multiple objectives is desirable.

1.1.3 Control Allocation Methods for Load Alleviation

One enabling characteristic for LA is that the aircraft must have more control inputs than the number of rigid body degrees of freedom, which are controlled to follow specific trajectories. This redundancy is referred to as over-actuation, and allows the control inputs to be utilized to handle multiple objectives using control allocation techniques. The control allocation structure is usually comprised of two stages: The first stage is a high-level controller, which guarantees the desirable output (e.g., flight trajectory tracking). The second stage is a detailed allocator satisfying a secondary objective (e.g., load alleviation) [32].

Control allocation literature categorizes the dynamic system's input redundancy as either strong or weak. A system has strong input redundancy when it is possible to inject an arbitrary signal in certain input directions without affecting the state response of the plant. A system has weak input redundancy when the arbitrary signal does not affect the steady-state output of the system [33], making weak input redundancy a subset of strong input redundancy. Strong input redundancy can also be thought of as when the number of control inputs exceeds the number of internal states used to define the system dynamics. Likewise, for weak input redundancy, the number of control inputs exceeds the number of controlled outputs.

Control allocation methods that exploit strong input redundancy have been previously proposed for the control of rigid aircraft [34]. Frost et al. [35] introduced a flight control framework with optimal control allocation using load constraints and load feedback. Miller and Goodrick [36] proposed a control allocation framework which accounts for tracking performance, trim condition enforcement, and critical load limiting. These control allocation methods based on strong input redundancy assume a static relationship between the load and the control inputs and may not be effective in regulating dynamic loads with pronounced transient characteristics as in flexible or very flexible aircraft. For this purpose, control allocation methods that exploit weak input redundancy are needed.

Toward this end, Gaulocher et al. [37] proposed a method to design a new control allocation law for an existing nominal flight controller using optimized dynamic trajectories. The authors used MPC and a prescribed maneuver to solve the dynamic optimal control allocation problem offline, considering structural load limits and actuator saturation while respecting the desired flight dynamics. A new control allocation law was then synthesized using a frequency-domain identification method based on the results from the offline optimization. This resulted in a heuristic system which performed nearly optimally and was only initially demonstrated using lateral maneuvers.

Pereira et al. [38] proposed two control system designs using MPC for MLA. One design directly provided a control allocation signal based on state feedback and load constraints. A second design used MPC to manipulate actuators pre-assigned to load alleviation and the reference commands before they were sent to a linear quadratic regulator controller in the inner loop. Both designs used cost functions which included portions to minimize control use along with tracking error. Results reduced wing bending by at least 30-40%, depending on wing stiffness, and successfully enforced bending constraint.

Hashemi and Nguyen [39] proposed a two-part control system for longitudinal command tracking that includes an adaptive control component to reduce maneuver loads. One controller handles the trajectory tracking while a secondary adaptive controller focuses on reducing the resultant maneuver loads. The secondary controller utilizes an output feedback model reference adaptive control framework and dedicated control surfaces to reduce bending moment, but unfortunately disrupts the trajectory tracking performance.

As shown by this last example, the above methods still include some sort of trade off between trajectory tracking performance and load alleviation. This occurs because these methods do not explicitly exploit the structure of input redundancy to decouple the two objectives of load alleviation and trajectory tracking.

Cocetti et al. [40] proposed a dynamic input allocator which directly exploits the input redundancy of a system for the purpose of input optimization. In this architecture, the dynamic input allocator works in the same control loop as a nominal controller to find the most suitable input trajectory based on certain performance criteria (e.g., energy minimization or saturation avoidance), while maintaining the same system output.

Duan and Okwudire [41, 42] developed an energy-optimal dynamic control allocation method for multi-input, multi-output LTI over-actuated systems using an optimal subspace which exploits the weak input redundancy of the system. This optimal subspace establishes an internal relationship within the null space between reference commands and desired output within which optimal control inputs can be found. Duan and Okwudire used matrix fraction description and spectral factorization to define a causal and stable proxy which measures the deviation from the optimal subspace. Then, optimal control trajectories were found by minimizing the proxy using $\mathcal{H}_\infty$ synthesis. This resulted in significant improvements of energy efficiency without affecting system outputs. The proposed method was designed to improve performance during prescribed mechanical processes (e.g., as in additive manufacturing) which led to solutions based on the entire duration of the process. In order to apply this method to a more dynamic process (e.g., aircraft maneuvers and gust encounters) may require a method to shape the solution in a transient way. This method was also limited by linear assumptions and did not consider robustness.

1.2 Literature Analysis and Features of This Dissertation

The load alleviation system developed in this work is designed so that it can be added to an existing aircraft. Additionally, the LA system is intended to complement, rather than replace, the nominal aircraft flight controller which has been tuned to provide the best performance for mission objectives. The available approaches for aircraft load alleviation can be distinguished by the use of additional hardware (or purpose-specific hardware) or just using existing hardware. In order to avoid the additional costs from structural analysis that come along with adding new hardware, a strictly software-based approach is pursued.

Within the software-based approaches, many methods reduced loads at the expense of aircraft flight performance (e.g., [20, 22, 26, 39]), which could degrade the aircraft's ability to meet mission objectives. This degradation of performance can be reduced by control allocation techniques based on multi-objective optimization, such as [35, 36, 38]. However, these techniques still involve a trade-off between load alleviation and flight performance because the two objectives are contained within the same cost function used for optimization. This trade-off can be avoided by using dynamic control allocation techniques to directly exploit the input redundancy of the aircraft and decouple the objectives of load alleviation and flight performance.

In this dissertation, a unified dynamic control allocation method for both MLA and GLA in weakly input redundant flexible aircraft is proposed. This method augments the nominal control system of the aircraft and exploits the aircraft's redundant control effectors. It is based upon the proxy-based optimal dynamic control allocation method developed by Duan and Okwudire [41, 42] and addresses the limitations identified by the authors. This work is distinct from the architecture proposed in [40] in that it is designed for a system with two distinct output types, where the control allocator exploits the null space of one output type (in the primary control loop) in order to control the other output type using an auxiliary control loop. In this way, the control architecture decouples the two objectives of load alleviation and rigid body trajectory tracking. It is assumed that a desired maneuver trajectory and the gust profile for the near future are known a priori (e.g., through measurements with a LIDAR for the gust). This assumption facilitates the development of a unified LA solution for both maneuver and gust loads.

The concept is first implemented with a full-knowledge preview of an aircraft maneuver. A receding horizon approach is then developed to increase robustness and accommodate gust disturbances and maneuvers with limited preview. A parameter-varying control allocation method is also developed to accommodate aircraft dynamics variability with flight conditions. The receding horizon control allocation approach is then used to inform an MPC-based control allocator function, which operates as an add-on scheme to a nominal controller and facilitates the implementation of the proposed approach in nonlinear model simulations.

The feasibility of the proposed method is investigated through numerical simulations on a model of a stiffened X-HALE aircraft [43] (shown in Fig. 1.2) and the Generic Transport Aircraft (GTA) [44]. The boundary of applicability of the proposed linear model-based LA system is characterized through simulations with nonlinear aircraft models. This characterization showed a limit with respect to the aircraft stiffness and resulted in a recommendation for a time preview horizon.

Figure 1.2: X-HALE aircraft developed at University of Michigan

1.3 Dissertation Outline

The LA system investigated in this dissertation is developed using a step-by-step approach, starting with the treatment based on linear system models and assumptions, and then increasing in nonlinearity and complexity. This approach provides a conservative way to prepare the system for eventual application to a more realistic aircraft representation. The remainder of this dissertation is organized as follows:

Chapter 2 presents the theoretical background used as a foundation for the development of the system presented in this work. It begins by presenting a generalized aircraft model, including the influence of gust disturbances and the separation of rigid body outputs and flexible outputs. Next is a discussion of input redundancy, delineating the distinction between systems that are strongly input redundant or weakly input redundant. Following that, the models used for gust disturbance representation are introduced.

Chapter 3 presents the theoretical development of the LA system developed in this work. It clarifies the primary and secondary objectives of the system, which are load alleviation and trajectory tracking, respectively. The derivation of the null space filter is presented, which constitutes the mechanism for meeting the secondary objective. Then the formulation of the Quadratic Programming (QP) problem is presented, which is used to meet the primary objective. As the next step, this initial LA system is enhanced, adding a method to alleviate the loads from gust disturbances on the aircraft. The enhancement also reframes the QP formulation so that it can be used over a limited preview horizon, which recedes as time moves forward. To accommodate aircraft dynamics variations with flight conditions, modifications needed to adapt the LA system for use with LPV models are considered. Several issues encountered in extending the proposed approach to the LPV setting are addressed. Finally, modifications which support the implementation of the proposed LA system on high fidelity aircraft models are developed. They enable the LA system to operate as an add-on scheme to a nominal controller in nonlinear dynamic simulations.

Chapter 4 presents numerical results which illustrate each step of the development of the proposed LA system. The two aircraft models used for numerical simulations of the LA system are described (i.e., the X-HALE and the GTA). Each aircraft model is described generally, and then in more detail for the flight conditions used to investigate the feasibility of the LA system concept. Numerical results are then presented as a proof of the proposed LA system. As the system is enhanced to account for gust loads and to utilize a limited preview with a receding horizon, additional numerical results show the effect of these features. Further numerical simulation results are used to show the efficacy of the modifications made to the system to accommodate its implementation based on LPV models. Finally, numerical results are reported from nonlinear dynamic simulations with the X-HALE and GTA nonlinear models.

Chapter 5 presents a case study used to characterize the limits of applicability of the LA system based on a linear model when applied to a nonlinear aircraft system. Specifically, the effects of aircraft flexibility level, preview horizon length, and load alleviation level on the performance of the LA system are considered.

Finally, Chapter 6 provides a summary of the dissertation, of the main conclusions and of the key benefits of the LA system. Recommendations are given for future work.

CHAPTER 2

Theoretical Background

This chapter presents the theoretical background used as a foundation for the development of the system introduced in this work. It begins by presenting a generalized aircraft model, including the influence of gust disturbances and the separation of rigid body outputs and flexible outputs. Next is a discussion of input redundancy, delineating the distinction between systems that are strongly input redundant or weakly input redundant. Following that, the models used for gust disturbance representation are introduced.

2.1 Aircraft Dynamic Modeling in the Presence of Structural Flexibility

Consider a flexible aircraft with n_u control inputs, including all control surfaces and thrusters. The aircraft is in free flight, with external inputs coming from a pilot or operator for maneuvers, and environmental disturbances, such as wind gusts. Assume the spatial dimension of the aircraft is relatively small compared to the gust ($< 10\%$); the gust is thus considered to be constant along the wingspan [45] and is represented by disturbances from longitudinal, lateral, and vertical directions, i.e., $g \in \mathbb{R}^3$. The values of the inputs for maneuvers and gust disturbances are assumed to be known a priori over a given preview horizon T_p, which may be shorter than the total maneuver time T_{man}. The outputs of the system include n_r rigid body outputs y_r (e.g., roll, pitch, yaw angles and their rates), and n_f flexible outputs y_f, which reflect structural deformation (e.g., curvature, bending moment, or load factor). It is assumed that there are more individual control input variables than rigid body outputs ($n_u > n_r$). The aircraft is initially in straight, level, unaccelerated flight, and its dynamics near this flight condition are represented by a LTI model with state-space representation,

$$\begin{cases} \dot{x}(t) = Ax(t) + B_u u(t) + B_g g(t), \\ y_r(t) = C_r x(t), \\ y_f(t) = C_f x(t). \end{cases} \tag{2.1}$$

The internal state $x \in \mathbb{R}^{n_x}$ of this system is comprised of the rigid body and flexible states of the aircraft. The system is assumed to be strictly proper (i.e., there are no feed through terms from input to output). Transfer function matrices are also used to represent this LTI system, i.e.,

$$\begin{bmatrix} y_f \\ y_r \end{bmatrix} = \underbrace{\begin{bmatrix} G_{fu}(s) & G_{fg}(s) \\ G_{ru}(s) & G_{rg}(s) \end{bmatrix}}_{G(s)} \begin{bmatrix} u \\ g \end{bmatrix}. \tag{2.2}$$

Here, $G_{fu}(s)$ and $G_{fg}(s)$ describe the dynamics of the flexible output of $G(s)$ from control inputs $u(s)$ and gust inputs $g(s)$, respectively. Likewise, $G_{ru}(s)$ and $G_{rg}(s)$ describe the dynamics of the rigid output of $G(s)$ from $u(s)$ and $g(s)$, respectively.

For very flexible aircraft, The degree of nonlinearity in structural dynamics of the aircraft may be so large that the linear assumptions used in the linearization process have a very small region of validity. In such cases, a nonlinear aircraft model is used; the dynamics and output have the following representation:

$$\begin{cases} \dot{x}(t) = f(x, u, g, t), \\ y_r(t) = h_r(x, t), \\ y_f(t) = h_f(x, t). \end{cases} \tag{2.3}$$

As with the linear representation, the internal state of this system is comprised of the rigid body and flexible states of the aircraft and the system is assumed to be strictly proper (i.e., there are no feed through terms from input to output).

2.2 Input Redundancy in Flexible Aircraft

Input redundancy can be either strong or weak. For a system with strong input redundancy [33], the control effector matrix B_u in Eq. (2.1) has a nontrivial null space, i.e.,

$$Ker\left(B_u\right) \neq 0. \tag{2.4}$$

In flexible aircraft, the inclusion of the structural dynamics usually results in more states than control inputs, and Eq. (2.4) is not satisfied. In such a case, the notion of weak input redundancy [33, 42, 46] with respect to rigid body outputs can be used. Weak input redundancy with respect to rigid body outputs holds if

$$Ker\left(G_{ru}\left(j\omega\right)\right) \neq 0, \text{ for all } \omega. \tag{2.5}$$

In flexible aircraft with weak input redundancy a desired rigid body output trajectory can be realized by multiple different selections of control input combinations. However, the various input selections may result in different trajectories for the flexible outputs. Consequently, weak input redundancy is exploited to achieve the two objectives of (1) alleviating loads caused by maneuvers and gusts while (2) maintaining desired trajectory tracking of the rigid body outputs.

2.3 Gust Model

There are two general ways to model wind gusts: discrete and continuous. The influence of the gust on the aircraft model is prescribed by the gust influence matrix B_g, as in Eq. (2.1). For a gust assumed to come from only one direction, the B_g matrix would have a single column. For a gust coming from any direction, B_g has three columns corresponding to longitudinal, lateral, and vertical gust components.

2.3.1 Discrete Gust Model

The discrete gust model treats the gust as a deterministic disturbance to the system with finite temporal distribution [20]. A typical example of a discrete gust is represented by the "1−cosine" profile disturbance to aircraft velocity. In the time domain, the discrete gust model is given by

$$g(t) = \frac{U_0}{2}\left[1 - \cos\left(\frac{2\pi t}{t_{\text{gust}}}\right)\right] \tag{2.6}$$

for $0 \leq t \leq t_{\text{gust}}$, where the peak gust velocity amplitude is U_0 and the duration of the gust cycle is t_{gust}. The resultant signal defines the amplitude of the gust disturbance and is used as an input $g(t)$ in Eqs. (2.1) and (2.2).

The "1−cosine" profile gust disturbance is prescribed for standard airworthiness certification in Title 14 of the Code of Federal Regulations (CFR) part 25 (Transport Category Airplanes) [47]. Section 25.341 details standards for gust and turbulence loads and uses a discrete gust model in the spatial domain, i.e.,

$$g(t) = \frac{U_{ds}}{2}\left[1 - \cos\left(\frac{\pi s}{H}\right)\right], \tag{2.7}$$

for $0 \leq s \leq 2H$. In this model, s is the distance penetrated into the gust, U_{ds} is the design gust velocity in equivalent airspeed, and H is the gust gradient, which is the distance along the airplane flight path for the gust to reach its peak velocity. The guidance on using an appropriate value for the gust gradient is to try several values from 30 to 350 feet to find the value providing a critical response. Section 25.341 also contains expressions to define U_{ds}, i.e.,

$$U_{ds} = U_{ref} F_g \left(\frac{H}{350} \right)^{1/6}, \tag{2.8}$$

where U_{ref} is the reference gust velocity in equivalent airspeed, which is defined by the flight altitude, and F_g is the flight profile alleviation factor. The appropriate value for F_g is found by linear interpolation between the value at sea level and a value of 1.0 at the maximum operating altitude. The F_g value at sea level is given by the following expression [47]:

$$\begin{aligned} F_g &= 0.5(F_{gz} + F_{gm}) \\ \text{where :} & \\ F_{gz} &= 1 - \tfrac{Z_{mo}}{250000}, \\ F_{gm} &= \sqrt{R_2 \tan(\pi R_1/4)}, \\ R_1 &= \tfrac{\text{maximum landing weight}}{\text{maximum take−off weight}}, \\ R_2 &= \tfrac{\text{maximum zero fuel weight}}{\text{maximum take−off weight}}, \end{aligned} \tag{2.9}$$

and Z_{mo} is the maximum operating altitude of the aircraft. For numerical demonstrations presented in this work, the assumed values of the above variables will be declared when appropriate.

2.3.2 Continuous Gust Model

For a continuous gust model, the gust velocity is modeled as a stochastic process with a known power spectral density (PSD) [20]. Two commonly used continuous gust models are the Dryden model and the von Kármán model. The gust velocity PSD for the vertical and lateral directions of the Dryden model [2] is given by

$$\Phi(\Omega) = \sigma_w^2 \frac{L_t}{\pi} \left[\frac{1 + 3L_t^2\Omega^2}{(1 + L_t^2\Omega^2)^2} \right] \tag{2.10}$$

while the gust velocity PSD for the von Kármán model is given by

$$\Phi(\Omega) = \sigma_w^2 \frac{L_t}{\pi} \left[\frac{1 + \frac{8}{3}(1.339 L_t\Omega)^2}{[1 + (1.339 L_t\Omega)^2]^{11/6}} \right]. \tag{2.11}$$

For each of these functions, σ_w is the root mean square gust velocity, L_t is the turbulence length, and Ω is the spatial frequency. Between these two models, the von Kármán model gives a better fit to observed data and is the standard model used for commercial aircraft development. However, the Dryden model is mathematically convenient as it admits a low order realization. A time history of the gust velocity is generated by applying Gaussian white-noise as an input to the Dryden or von Kármán models [2]. This time history is then used as as input $g(t)$ in Eqs. (2.1) and (2.2). MATLAB and Simulink have functions that generate Dryden or von Kármán gust disturbances depending on aircraft velocity, altitude, and the direction cosines matrix [48, 49].

CHAPTER 3

Theoretical Development of Load Alleviation System

This chapter presents the theoretical development of the LA system. It clarifies the primary and secondary objectives of the system, which are load alleviation and trajectory tracking, respectively. A combination of a null space filter and QP-based null-space trajectory generation based on a linear model provide a starting basis to meet these objectives. This LA system is then enhanced to address nonlinearities. It concludes with steps to enable the LA system to run on top of a nominal controller for nonlinear dynamic simulations.

3.1 Overall System Architecture and Objectives

The block diagram of the proposed system which accomplishes load alleviation through control allocation is shown in Fig. 3.1. Assume the flexible aircraft G is controlled to track a specified trajectory $r(t) \in \mathbb{R}^{n_r}$, $0 \leq t \leq T_p$, for its rigid body outputs, where T_p is the preview horizon. The tracking is realized through a nominal controller, C, which uses only the rigid body output y_r for feedback, and generates a n_u-dimensional control input u_0. Note that this nominal controller C directly generates control effector commands and thus can for instance aggregate a typical flight controller [50, 51], which generates required forces and moments and nominal control allocation. The

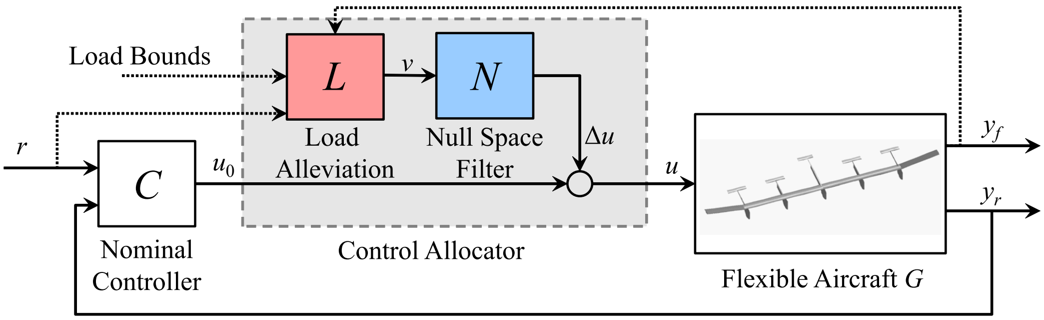

Figure 3.1: Block diagram of load alleviation through control allocation architecture

reference commands provided to the nominal controller, along with the y_r feedback signal, produce a controlled rigid output trajectory, $y_r(t) \in \mathbb{R}^{n_r}$, $0 \leq t \leq T_p$ and a flexible output trajectory, $y_f(t) \in \mathbb{R}^{n_f}$, $0 \leq t \leq T_p$.

Note that the model of the flexible aircraft, G, has a large state dimension to represent aeroelastic behavior. Consequently, a weak input redundancy, described in Section 2.2, is used to inform the design of control allocation for load alleviation. Weak input redundancy holds when the dimension of the control input, n_u, exceeds the dimension of the reference command, n_r, and Eq. (2.5) is satisfied. This provides an opportunity to control the flexible outputs of the system y_f without affecting tracking performance (i.e., the relationship between r and y_r).

The implementation of our control allocation framework is based on two steps: (i) the offline generation of a null space filter, which is designed so that the control input increment Δu produced as an output of this null space filter does not affect the rigid body output y_r, and (ii) online generation of a null space variable trajectory v which is an input to the null space filter and enforces the bounds on y_f using a preview of the trajectory of the flexible output with the nominal controller. As Fig. 3.1 illustrates, these two functions are realized through two highlighted blocks N and L. This Control Allocator (CA) incrementally adds Δu to the u_0 signal from the nominal controller, which simplifies the design and tuning process.

3.1.1 Null Space Filter Design

The proposed CA generates a control input increment signal, Δu, and adds it to the output, u_0, from the existing nominal controller to inform the control input for the aircraft, i.e.,

$$u = u_0 + \Delta u. \tag{3.1}$$

Assuming a linear model for the aircraft, we consider the transfer function representation for its input-output behavior in the form $[y_r; y_f] = [G_{ru}(s); G_{fu}(s)]u$. Subsequent developments also assume zero initial conditions. The null space filter is designed to ensure that the introduction of the Δu signal still results in $G_{ru}(s)u = G_{ru}(s)u_0$, i.e.,

$$G_{ru}(s)\Delta u = 0. \tag{3.2}$$

Note that $G_{ru}(s)$ used in the subsequent control allocation procedure is a transfer function matrix and not a static matrix, as is common in the existing control allocation literature for strongly input redundant systems. Therefore, to achieve invariant rigid body response, the trajectory of Δu needs to be determined for the full maneuver rather than statically. Note also that $G_{ru}(s)$ is a fat transfer function matrix as $n_u > n_r$, and $n_e = n_u - n_r$ is defined as the level of input redundancy. Accordingly, u can be decomposed into n_r principal control inputs u_p and n_e extra control inputs u_e. Since input channels can always be re-ordered, one may assume that the first n_r inputs are the principal control inputs, i.e.,

$$G_{ru}(s) = \begin{bmatrix} G_p(s) & G_e(s) \end{bmatrix}, \; u = \begin{bmatrix} u_p^{\mathrm{T}} & u_e^{\mathrm{T}} \end{bmatrix}^{\mathrm{T}}. \tag{3.3}$$

Note that $G_p(s)$ is a square transfer function matrix of dimension $n_r \times n_r$ and is assumed to be invertible While $G_e(s)$ is of dimension $n_r \times n_e$.

Based on Eq. (3.3), one approach to generate a control increment Δu that achieves the objective in Eq. (3.2) is by defining a dynamic system, with an arbitrary n_e-dimensional signal v as its input, as follows

$$\Delta u = \begin{bmatrix} G_p^{-1}(s)G_e(s) \\ -I \end{bmatrix} v. \tag{3.4}$$

The signal v will be referred to as the null space variable. Since there is usually no guarantee that $G_p^{-1}(s)G_e(s)$ is stable, Eq. (3.4) is transformed into a different format, such that all the unstable dynamics are only reflected in the zero dynamics [41]. To accomplish this, $G_p^{-1}(s)G_e(s)$ is expressed using its matrix fractional description [52], i.e.,

$$G_p^{-1}(s)G_e(s) = N_G(s)D_G^{-1}(s), \tag{3.5}$$

where $N_G(s)$ and $D_G(s)$ are transfer function matrix polynomials. Then, an additional square minimal phase denominator transfer function matrix polynomial, $D_0(s)$, is generated to ensure the stability of the null space filter. This leads to the following definition of the null space filter:

$$\Delta u = \underbrace{\begin{bmatrix} -N_G(s)D_0^{-1}(s) \\ D_G(s)D_0^{-1}(s) \end{bmatrix}}_{N(s)} v. \tag{3.6}$$

With Δu generated by Eq. (3.6), it follows that

$$
\begin{aligned}
G_{ru}(s)\Delta u &= \begin{bmatrix} G_p(s) & G_e(s) \end{bmatrix} \begin{bmatrix} -N_G(s)D_0^{-1}(s) \\ D_G(s)D_0^{-1}(s) \end{bmatrix} v \\
&= \underbrace{\left[-G_p(s)N_G(s) + G_e(s)D_G(s)\right]}_{=0} D_0^{-1}(s)v \\
&= 0,
\end{aligned}
\tag{3.7}
$$

i.e., Eq. (3.2) holds and the output of the null space filter, $N(s)$, added to the nominal input, u_0, will not affect the rigid body outputs, independently of the selection of the signal, v.

Note that the choice of $N_G(s)$, $D_G(s)$ and $D_0(s)$ is nonunique. Usually $D_0(s)$ is selected in the form of a lowpass filter such that the control effort redistribution only happens at low frequencies where the model is relatively accurate. Additionally, $N(s)$ should have minimal resonant peaks within the designed bandwidth. To achieve this, $D_0(s)$ is selected to be a diagonal transfer function matrix polynomial, i.e.,

$$
D_0\left(s\right) = \mathrm{diag}\left\{d_1\left(s\right),\ d_2\left(s\right),\ \ldots,\ d_{n_e}\left(s\right)\right\}. \tag{3.8}
$$

Note that each $d_i(s)(i = 1, 2, \ldots, n_e)$ serves as the common denominator of the ith column of $N_G(s)$ and $D_G(s)$, thus can be generated by averaging corresponding columns. Defining this average to be φ_i for each column, i.e.,

$$
\varphi_i\left(s\right) = \frac{1}{n_u}\left(\sum_{k=1}^{n_y} N_G^{(k,i)}\left(s\right) + \sum_{k=1}^{n_e} D_G^{(k,i)}\left(s\right)\right),\ \ \left(i = 1, 2, \ldots, n_e\right), \tag{3.9}
$$

where superscript $^{(k,i)}$ indicates the element in the kth row and the ith column in a transfer function matrix. Accordingly, $d_i(s)$ is selected as

$$
d_i\left(s\right) = \varphi_{mp,i}\left(s\right)\left(\frac{s^2}{\omega_0^2} + 2\frac{\zeta}{\omega_0}s + 1\right), \tag{3.10}
$$

where $\varphi_{mp,i}(s)$ is the minimal phase transformation of $\varphi_i(s)$ obtained by reflecting right half plane zeros of $\varphi_i(s)$ to their mirror locations in the left half plane. The additional second-order polynomial in Eq. (3.10) ensures that $N(s)$ is strictly proper, and sets the control allocation bandwidth to ω_0.

3.1.2 Maneuver Load Alleviation

With the null space filter in place, the Δu signal generated as its output will not affect the rigid body output $y_r(t)$ (i.e., $G_{ru}(s)\Delta u = 0$). The null space variable signal, $v(t)$, can now be generated to affect the flexible output $y_f(t)$. As shown in Fig. 3.1, the load alleviation calculation uses a preview of the reference signal, $r(t)$, $0 \leq t \leq T_p$, along with an LTI model of the flexible aircraft with the nominal controller to generate a predicted trajectory of the flexible output, $y_f(t)$, $0 \leq t \leq T_p$. Then, the load alleviation calculation uses this predicted trajectory of $y_f(t)$ and the given bounds, y_f^- and y_f^+, to generate $v(t)$. The following derivation shows this process.

Firstly, the closed loop rigid output response of the flexible aircraft with its nominal controller (in a negative feedback loop) is calculated as

$$\begin{aligned} y_r &= G_{ru}(s)[u_0 + \Delta u] \\ &= G_{ru}(s)C(s)[r - y_r] \\ &= [I + G_{ru}(s)C(s)]^{-1}G_{ru}(s)C(s)r. \end{aligned} \tag{3.11}$$

Secondly, the response of the flexible output is calculated as

$$\begin{aligned} y_f &= G_{fu}(s)[u_0 + \Delta u] \\ &= G_{fu}(s)[C(s)(r - y_r) + N(s)v]. \end{aligned} \tag{3.12}$$

Then, inserting Eq. (3.11) into Eq. (3.12) yields

$$\begin{aligned} y_f \quad &= \underbrace{G_{fu}(s)C(s)\left[I-(I+G_{ru}(s)C(s))^{-1}G_{ru}(s)C(s)\right]}_{H_{fr}(s)} r \\ &+ \underbrace{G_{fu}(s)N(s)}_{H_{fv}(s)} v, \end{aligned} \tag{3.13}$$

where $H_{fr}(s)$ and $H_{fv}(s)$ are transfer functions which represent the combined response from the reference signal and the null space variable signal. Eq. (3.13) can be converted into the following state space representation:

$$\begin{aligned} \dot{x}_{\mathrm{CL}}(t) &= A_{\mathrm{CL}}x_{\mathrm{CL}}(t) + B_{r,\mathrm{CL}}r(t) + B_{v,\mathrm{CL}}v(t) \\ y_f(t) &= C_{f,\mathrm{CL}}x_{\mathrm{CL}}(t). \end{aligned} \tag{3.14}$$

Let $y_f(t)$, $t \geq 0$, denote the output of the system in Eq. (3.14) assuming zero initial conditions. We can decompose it as

$$y_f(t) = y_{fr}(t, r(\cdot)) + y_{fv}(t, v(\cdot)), \tag{3.15}$$

where y_{fr} is the component of the flexible output from the reference signal and y_{fv} is the component of the flexible output from the null space variable signal. The assumption of zero initial conditions is reasonable when the maneuver starts from a trim state, such as straight, level, unaccelerated flight.

With this expression for the flexible output, one can now set conditions on the null space variable to ensure that $\Delta u(t)$ affects $y_f(t)$ so that it lies within bounds y_f^- and y_f^+ for the entire preview time, $0 \leq t \leq T_p$:

$$y_f^- \leq y_f(t) \leq y_f^+ \Leftrightarrow \tag{3.16}$$

$$y_{fv}(t, v(\cdot)) \geq y_f^- - y_{fr}(t, r(\cdot)),\; y_{fv}(t, v(\cdot)) \leq y_f^+ - y_{fr}(t, r(\cdot)). \tag{3.17}$$

Now $v(t)$ can be found so that the 2-norm of $v(t)$ is minimized subject to the constraints given by Eq. (3.17). Note that $y_{fr}(t, r(\cdot))$ in Eq. (3.17) can be computed by simulation of the model of the flexible aircraft with the nominal controller. To determine the minimum 2-norm v which satisfies constraints (3.17), we use a discrete-time approximation. Let T_s be the discrete sampling time and

$$\begin{aligned}
\mathbf{v}^{(k)} &= \begin{bmatrix} v^{(k)}(0) & v^{(k)}(T_s) & \cdots & v^{(k)}(n_T T_s) \end{bmatrix}^{\mathrm{T}}, & k &= 1, 2 \ldots, n_e, \\
\mathbf{y}_{fv}^{(i)} &= \begin{bmatrix} y_{fv}^{(i)}(0, v(\cdot) & y_{fv}^{(i)}(T_s, v(\cdot)) & \cdots & y_{fv}^{(i)}(n_T T_s, v(\cdot)) \end{bmatrix}^{\mathrm{T}}, & i &= 1, 2 \ldots, n_f, \\
\mathbf{y}_{fr}^{(i)} &= \begin{bmatrix} y_{fr}^{(i)}(0, r(\cdot) & y_{fr}^{(i)}(T_s, r(\cdot)) & \cdots & y_{fr}^{(i)}(n_T T_s, r(\cdot)) \end{bmatrix}^{\mathrm{T}}, & i &= 1, 2 \ldots, n_f,
\end{aligned} \tag{3.18}$$

where $n_T = \lceil T_p / T_s \rceil$ denoted the number of samples required to cover the preview horizon T_p. Then, assuming v is constant between samples, it follows that

$$\begin{aligned}
\underbrace{\begin{bmatrix} \mathbf{y}_{fv}^{(1)} \\ \vdots \\ \mathbf{y}_{fv}^{(n_f)} \end{bmatrix}}_{\mathbf{y}_{fv}} &= \underbrace{\begin{bmatrix} \mathbf{H}_{fv}^{(1,1)} & \cdots & \mathbf{H}_{fv}^{(1,n_e)} \\ \vdots & \ddots & \vdots \\ \mathbf{H}_{fv}^{(n_f,1)} & \cdots & \mathbf{H}_{fv}^{(n_f,n_e)} \end{bmatrix}}_{\mathbf{H}_{fv}} \underbrace{\begin{bmatrix} \mathbf{v}^{(1)} \\ \vdots \\ \mathbf{v}^{(n_e)} \end{bmatrix}}_{\mathbf{v}}, \\
\mathbf{H}_{fv}^{(i,k)} &= \begin{bmatrix} h_{fv}^{(i,k)}(0) & 0 & 0 & 0 \\ h_{fv}^{(i,k)}(T_s) & h_{fv}^{(i,k)}(0) & 0 & 0 \\ \vdots & \vdots & \ddots & 0 \\ h_{fv}^{(i,k)}(n_T T_s) & h_{fv}^{(i,k)}((n_T - 1) T_s) & \cdots & h_{fv}^{(i,k)}(0) \end{bmatrix},
\end{aligned} \tag{3.19}$$

where $\left\{ h_{fv}^{(i,k)}(0),\ h_{fv}^{(i,k)}(T_s), \ldots,\ h_{fv}^{(i,k)}(n_T T_s) \right\}$ is the impulse response of $H_{fv}^{(i,k)}(s)$ [53]. In discrete-time, the problem of determining the null space variable trajectory, $v(t)$, reduces to a QP problem:

$$
\begin{aligned}
\min_{\mathbf{v}} \quad & \mathbf{v}^{\mathrm{T}}\mathbf{v}, \\
\text{s.t.} \quad & \mathbf{H}_{fv}\mathbf{v} \leq y_f^+ - \mathbf{y}_{fr}, \\
& -\mathbf{H}_{fv}\mathbf{v} \leq -y_f^- + \mathbf{y}_{fr}.
\end{aligned}
\tag{3.20}
$$

Note that no a priori guarantees of feasibility of Eq. (3.20) can be given; the constraints can be relaxed with slack variables to ensure that Eq. (3.20) is always feasible. Furthermore, basis functions can be exploited to represent v, thereby potentially reducing the computational load.

Note that the above approach assumes complete a priori knowledge of the reference and any other external inputs for the entire maneuver time. Hence it is referred to as the "full preview" approach. This assumption may not be realistic for maneuvers lasting longer than a few seconds, especially when considering the stochastic nature of maneuvering flight and gust disturbances, therefore, a more robust approach is desired for such circumstances. Such a robust approach is developed in Section 3.2.

3.2 Enhancement of Load Alleviation System for Gust Disturbances and Limited Preview

The methods developed in Section 3.1.2 can be further enhanced with the capability to account for gust disturbances, along with aircraft maneuvers. As depicted in Fig. 3.2, now a combination of reference command, $r(t)$, and gust disturbance, $g(t) \in \mathbb{R}^3$, from longitudinal, vertical, and lateral directions is considered. As described above, these external inputs affect the rigid output trajectory, $y_r(t)$, which is controlled by the nominal controller, and the flexible output, $y_f(t)$, which is not controlled by the nominal controller.

In what follows, an approach to including gust disturbances into our load alleviation system is described. Then a receding horizon approach is proposed to improve

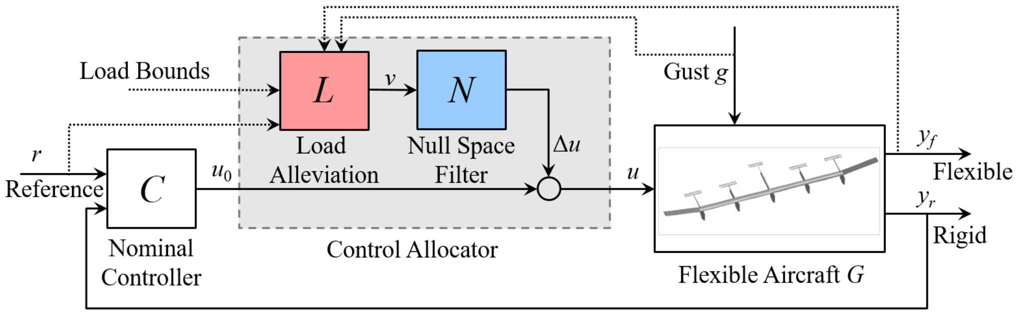

Figure 3.2: Block diagram of load alleviation through control allocation architecture, including gust disturbances

the robustness of the load alleviation system to the uncertainty in the preview of the reference command and gust disturbance. With the receding horizon implementation, the preview horizon used for optimization can be shorter than the maneuver time ($T_p < T_{\text{man}}$), and chosen so that it provides a more accurate preview. The robustness is improved as the solution is recomputed at discrete time instants.

3.2.1 Inclusion of Gust Disturbance for Load Alleviation

To include gust disturbances, the same null space filter design is adopted but the procedure to compute the trajectory of the null space variable v is modified as the gust disturbance is included as an additional external input. The preview of the gust is assumed to be available over the preview horizon which can be generated using, e.g., LIDAR [29]. Beginning with an analysis of the response of the rigid body output and flexible output, Eqs. (3.11) and (3.12) become:

$$\begin{aligned} y_r &= G_{ru}(s)[u_0 + \Delta u] + G_{rg}(s)g \\ &= G_{ru}(s)C(s)[r - y_r] + G_{rg}(s)g \\ &= [I + G_{ru}(s)C(s)]^{-1}G_{ru}(s)C(s)r \\ &\quad + [I + G_{ru}(s)C(s)]^{-1}G_{rg}(s)g, \end{aligned} \tag{3.21}$$

where g is the Laplace transform of the gust input and $G_{rg}(s)$ is the transfer function from the gust to the rigid body output (as in Eq. (2.2)), and

$$\begin{aligned} y_f &= G_{fu}(s)\left[u_0 + \Delta u\right] + G_{fg}(s)g \\ &= G_{fu}(s)\left[C(s)\left(r - y_r\right) + N(s)v\right] + G_{fg}(s)g, \end{aligned} \tag{3.22}$$

where $G_{fg}(s)$ is the transfer function from the gust to the flexible output. Inserting Eq. (3.21) into Eq. (3.22) yields

$$\begin{aligned} y_f &= \underbrace{G_{fu}(s)C(s)\left[I - (I + G_{ru}(s)C(s))^{-1}G_{ru}(s)C(s)\right]}_{H_{fr}(s)} r \\ &+ \underbrace{\left[G_{fg}(s) - G_{fu}(s)C(s)(I + G_{ru}(s)C(s))^{-1}G_{rg}(s)\right]}_{H_{fg}(s)} g \\ &+ \underbrace{G_{fu}(s)N(s)}_{H_{fv}(s)} v. \end{aligned} \tag{3.23}$$

The state space representation corresponding to Eq. (3.23) has the following form,

$$\begin{aligned} \dot{x}_{\mathrm{CL}}(t) &= A_{\mathrm{CL}}x_{\mathrm{CL}}(t) + B_{r,\mathrm{CL}}r(t) + B_{g,\mathrm{CL}}g(t) + B_{v,\mathrm{CL}}v(t), \\ y_f(t) &= C_{f,\mathrm{CL}}x_{\mathrm{CL}}(t), \end{aligned} \tag{3.24}$$

where x_{CL} includes states from the aircraft model, the nominal controller, and the null space filter. Let $y_f(t)$, $0 \le t \le T_p$, denote the trajectory of the flexible output corresponding to the specified initial condition $x_{\mathrm{CL}}(0)$, and inputs $r(t)$, $g(t)$, and $v(t)$, $0 \le t \le T_p$, and computed from Eq. (3.24). To pave the way for the receding horizon implementation in Section 3.2.2, zero initial conditions are no longer assumed. Note that by linearity,

$$y_f(t) = y_{f_0}(t, x_{\mathrm{CL}}(0)) + y_{fr}(t, r(\cdot)) + y_{fg}(t, g(\cdot)) + y_{fv}(t, v(\cdot)), \tag{3.25}$$

where y_{fr}, y_{fg}, y_{fv} designate the flexible output responses to zero initial condition and $r(t)$, $g(t)$, and $v(t)$, respectively (with other inputs set to zero in each case). The y_{f_0} designates the initial condition response (with zero inputs) of the system in

Eq. (3.24). The load bounds on $y_f(t)$ can now be written as constraints on $y_{fv}(t, v(\cdot))$:

$$\begin{aligned}
&y_f^- \leq y_f(t) \leq y_f^+ \Leftrightarrow \\
&y_{fv}(t, v(\cdot)) \geq y_f^- - y_{f0}(t, x_{\mathrm{CL}}(0)) - y_{fr}(t, r(\cdot)) - y_{fg}(t, g(\cdot)), \\
&y_{fv}(t, v(\cdot)) \leq y_f^+ - y_{f0}(t, x_{\mathrm{CL}}(0)) - y_{fr}(t, r(\cdot)) - y_{fg}(t, g(\cdot)).
\end{aligned} \tag{3.26}$$

Just as in Section 3.1.2, one can look for an input $v(t)$ with minimum 2-norm subject to these constraints, convert this problem to discrete-time, and ultimately to a QP problem.

3.2.2 Receding Horizon Implementation

The receding horizon approach is intended to provide a more robust way to handle maneuvers lasting longer than a few seconds as well as preview uncertainty. The approach assumes that accurate a priori knowledge of reference and gust inputs is available over a limited preview horizon T_p (e.g., a few seconds or less). The minimum norm trajectory for $v(t)$ is calculated over the preview horizon subject to the constraints in Eq. (3.26) by solving a QP problem. However, only the first few elements of the solution sequence are applied to the system (this shorter time interval is referred to as the implementation horizon $T_i < T_p$). For example, the k^{th} computation interval spans $kT_i \leq t \leq kT_i + T_p$ and the solution from kT_i to $(k+1)T_i$ is implemented. In this way, the entire maneuver over the time interval $[0, T_{\text{man}}]$ requires at least $\lceil T_{\text{man}}/T_i \rceil$ implementation horizons. For each k^{th} implementation horizon, the initial state $x_{\mathrm{CL}}(kT_i)$ is assumed to be known (e.g., estimated by an observer).

As in the full preview approach, to find the optimal $v(t)$, a QP-based formulation is used. However, rather than minimizing the 2-norm of $v_k(t)$ over the preview horizon, better results were obtained when the objective function to be minimized was chosen as the square of the 2-norm of the difference $\Delta v_k(t)$ relative to an assumed null space variable trajectory $v_{a,k}(t)$. That is,

$$v_k(t) = v_{a,k}(t) + \Delta v_k(t), \tag{3.27}$$

for $kT_i \leq t \leq kT_i + T_p, k = 0, 1, 2, \dots,$ where the minimum 2-norm solution is sought for $\Delta v_k(t)$ is subject to the imposed constraints. The nominal trajectory of $v_{a,k}(t)$ for $k = 0$ is zero and for $k \geq 1$ is informed by the trajectory of $v_{k-1}(t)$ as follows

$$v_{a,k}(t) = \begin{cases} v_{k-1}(t + T_i), & kT_i \leq t \leq kT_i + T_p - T_i, \\ \tilde{v}_{a,k}(t), & kT_i + T_p - T_i \leq t \leq kT_i + T_p, \end{cases} \tag{3.28}$$

where $\tilde{v}_{a,k}(t)$ is a linear function of time with boundary values $v_{k-1}((k-1)T_i + T_p)$ and zero.

When discretizing the problem, filtering Δv_k with $H_{fv}(s)$ is represented by the multiplication of Toeplitz matrix $\mathbf{H}_{fv}$ and $\mathbf{\Delta v}_k$ (sampled $\Delta v_k(t)$ arranged in a single-column vector), as detailed in Section 3.1.2. The flexible output components over the k^{th} calculation interval are also sampled and arranged in single-column vectors $\mathbf{y}_{f0,k}$, $\mathbf{y}_{fr,k}$, $\mathbf{y}_{fg,k}$ and $\mathbf{y}_{fv_a,k}$. Therefore, in order to find the optimal $\Delta v_k(t)$ to control the flexible output for each implementation interval, the QP problem becomes:

$$\begin{aligned} \min_{\mathbf{\Delta v}_k} \quad & \mathbf{\Delta v}_k^{\mathrm{T}} \mathbf{\Delta v}_k, \\ \text{s.t.} \quad & \mathbf{H}_{fv} \mathbf{\Delta v}_k \leq y_f^+ - \mathbf{y}_{f0,k} - \mathbf{y}_{fr,k} - \mathbf{y}_{fg,k} - \mathbf{y}_{fv_a,k}, \\ & -\mathbf{H}_{fv} \mathbf{\Delta v}_k \leq -y_f^- + \mathbf{y}_{f0,k} + \mathbf{y}_{fr,k} + \mathbf{y}_{fg,k} + \mathbf{y}_{fv_a,k}. \end{aligned} \tag{3.29}$$

As noted in Section 3.1.2, there is no guarantee of feasibility of Eq. (3.29), however, in practice the constraints can be relaxed with slack variables to ensure feasibility. The computational load for the QP problem increases with the number of redundant control effectors n_e and the chosen time duration of the preview horizon T_p. However, choosing a shorter T_p may not ensure recursive feasibility.

3.3 Adapting the Load Alleviation System for Use with Parameter-Varying Systems

When applying the LA system proposed in this work to a more realistic aircraft representation, one must consider nonlinear structural and flight dynamics that are not captured by a linearization of the aircraft model about a single equilibrium point. For example, the static structural deformation may be different at airspeeds higher or lower than the equilibrium airspeed, resulting in a bias error. This type of bias error may result in violations of structural constraints in the physical aircraft, while the constraint was satisfied according to the dynamics of the linearized aircraft model. This phenomenon can be observed in Fig. 3.3, which presents numerical results of the full preview method to constrain the bending curvature of a flexible aircraft when recovering from a descent. While descending, the aircraft velocity increases, which causes an increase in the bending curvature influence from the horizontal tail control surfaces. However, the solution from the LA system was based on the initial equilibrium airspeed and its corresponding bending curvature influence matrix. While it reduces the dynamic curvature, it does not satisfy the constraint, as seen by the plot of the left curvature. To address this issue, the LA system is adapted for use with a parameter-varying aircraft model, as a first-step toward adaptation for use with a nonlinear aircraft model and, eventually, for use with more realistic aircraft representations.

3.3.1 Impact of Parameter-Varying System on Load Alleviation Step

In order to modify the LA system for application to an LPV aircraft model, one starts by identifying an appropriate parameter that will distinguish significant operating points and their associated dynamics. Then, one examines how this parameter affects

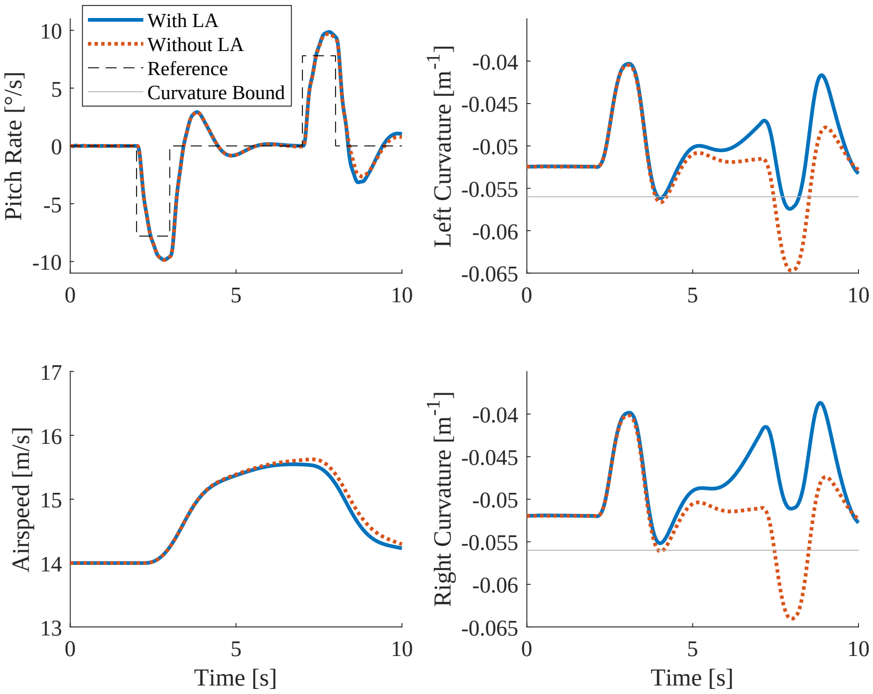

Figure 3.3: Example results of bias error for a full preview solution using an LTI LA system applied to an LPV aircraft model

the principal dynamics of the system. For flexible aircraft in this work, the dynamic pressure, q, was chosen as a distinguishing parameter because it incorporates the influence of both altitude and airspeed on the flexible output of the system. Beginning with the model of the flexible aircraft, Eq. (2.1) is expressed as an LPV system as follows:

$$\begin{cases} \dot{x}(t) &= A(q(t))x(t) + B_u(q(t))u(t) + B_g(q(t))g(t), \\ y_r(t) &= C_r(q(t))x(t), \\ y_f(t) &= C_f(q(t))x(t). \end{cases} \tag{3.30}$$

However, the practical effect of this change in the aircraft model on the LA system is found by examining the derivation of the null space filter and the QP formulation used for the load alleviation step. Looking at each of these portions of the LA system separately, this section will focus on the load alleviation step, while the change for the null space filter will be examined in a subsequent section.

The formulation of the QP problem first begins by deriving a closed-loop system expression of the flexible output based only on the external inputs (i.e., reference and null space variable signals and possible gust disturbance). This expression is important because it provides a connection between the unknown null space variable signal and the given constraints to the flexible output and the predicted flexible response based on the other external inputs. Therefore, even though there are internal changes in the dynamics which produce the flexible output, the QP formulation only depends on the predicted flexible output signal. Therefore, when using an invariant null space filter, no significant modifications of Eq. (3.29) are needed to find an optimal signal $v(t)$ to satisfy the constraints.

3.3.2 Development of Parameter-Varying Null Space Filter

Using an LPV null space filter helps ensure that the incremental control output from the null space filter, $\Delta u(t)$, does not affect the rigid body output when the specified parameter varies. To accomplish this, each linear model of the aircraft $G_i(s)$ corresponding to a particular q_i is used, in turn, as a basis for generating a null space filter $N_i(s)$ for $i = 1,\ 2, \ldots,\ n_m$, where n_m is the number of linear models used to define the LPV system.

Two issues must be addressed to be able to implement such a parameter-varying null space filter. The first issue is that the null space filter is not unique. Hence, the null space filters for different values of the scheduling parameter may be mismatched with each other with respect to their effect on $\Delta u(t)$. The second issue is that each null space filter has its own internal state which is typically non-physical and is not matched to the internal states of the other null space filters $N_i(s)$.

Figure 3.4 stands as an example of how these issues can influence the LA system response. In this descent maneuver, as the dynamic pressure increases, the LPV null space filter transitions from one linear model to another to calculate $v(t)$. When this transition occurs while the $v(t)$ signal is active (e.g., at 5.75 seconds), it may result in instabilities.

3.3.2.1 Normalization of Null Space Filter Output Signals

The first of above issues is addressed by normalizing the null space filters $N_i(s),\ i = 1,\ 2, \ldots,\ n_m$. The idea of this normalization is to replace $N_i(s)$ by $\Lambda_{u,i} N_i(s) \Lambda_{v,i}$, where $\Lambda_{u,i}$ and $\Lambda_{v,i}$ are diagonal conditioning matrices; these conditioning matrices are referred to as a post-filter matrix and a pre-filter matrix, respectively. These conditioning matrices are determined as follows. The $\Lambda_{v,i}$ is defined by computing the mean value, $m_{ig},\ g = 1,\ 2, \ldots,\ n_e$, of the absolute value of all elements in the g^{th} column of the DC gain matrix of the null space filter, $N_i(0)$. With the desired

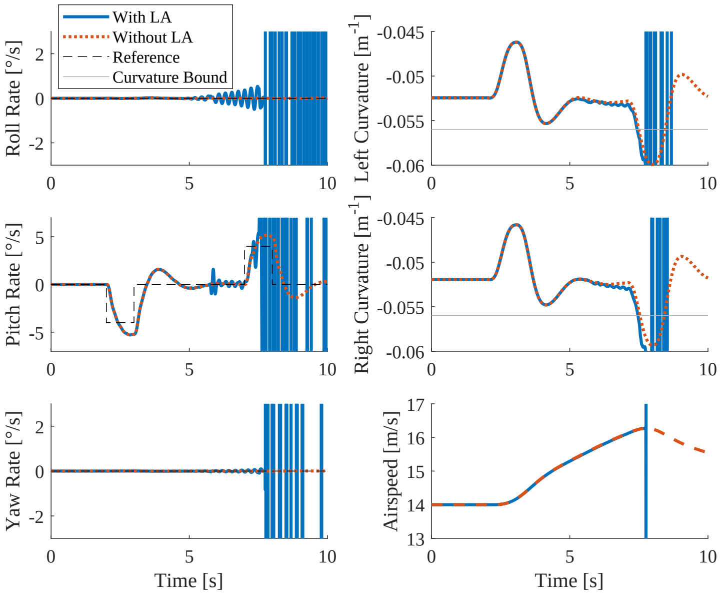

Figure 3.4: Responses of rigid body motion and wing root bending curvature for descent showing complications of an uncorrected LPV null space filter system

interval I_v selected for the input, a value $\lambda_{v,ig}$ is determined such that $m_{ig}\lambda_{v,ig} \in I_v$. The $\lambda_{v,ij}$ values are then the diagonal elements of the pre-filter matrix $\Lambda_{v,i}$.

To determine the post-filter matrix, $\Lambda_{u,i}$, the mean value, m_{ih}, $h = 1,\ 2, \ldots,\ n_u$ of the absolute value of all elements in the h^{th} row of the product of $N_i(0)\Lambda_{v,i}$ is computed. With the desired interval $I_{u,h}$ selected, a value $\lambda_{u,ih}$ is determined such that $m_{ih}\lambda_{u,ih} \in I_{u,h}$. The $\lambda_{u,ih}$ values are then the diagonal elements of the post-filter matrix $\Lambda_{u,i}$. The intervals $I_{u,h}$ are selected so that they coincide for similar types of actuators (actuators that have similar range) and to produce coordinated symmetric/asymmetric responses. For instance, the rows corresponding to the left and right flap actuator channels can use the same interval to promote symmetry (e.g., $I_{u,1}$). Likewise, rows for the left and right thrust channels can use the same interval (e.g., $I_{u,2}$). However, since flaps and thrust are not similar types of actuators, in general $I_{u,1} \neq I_{u,2}$. Using the same I_v and $I_{u,h}$ intervals to define each $\Lambda_{v,i}$ and $\Lambda_{u,i}$ for $i = 1,\ 2, \ldots,\ n_m$ normalizes the parameter varying set of null space filters.

Note that the pre-filter $\Lambda_{v,i}$ does not affect the defining characteristic of the null space filter, that the output from the null space filter should not affect the rigid body output. Indeed,

$$G_{ru,i}(s)N_i(s) = 0 \Rightarrow G_{ru,i}(s)N_i(s)\Lambda_{v,i} = 0. \tag{3.31}$$

However, the postfilter, $\Lambda_{u,i}$, may affect the rigid body output unless $\Lambda_{u,i}$ is a scalar multiple of the identity matrix. That is, in general,

$$G_{ru,i}(s)\Lambda_{u,i}N_i(s) \neq 0, \tag{3.32}$$

and hence, another approach is needed.

Consider the ideal normalization of the null space filter given by

$$N_i^*(0) = \Lambda_{u,i}N_i(0)\Lambda_{v,i}. \tag{3.33}$$

One can obtain $N_i^*(0)$ by using only a pre-filter, $K_{v,i}$, if one can express

$$N_i^*(0) = N_i(0)K_{v,i}. \tag{3.34}$$

Note that because this is an over-actuated system, $N_i(0)$ has more rows than columns and $N_i(0)^{\mathrm{T}}N_i(0)$ is full rank. Hence, Eq. (3.34) can be solved for $K_{v,i}$ with the solution given by the pseudoinverse:

$$K_{v,i} = (N_i(0)^{\mathrm{T}}N_i(0))^{-1}N_i(0)^{\mathrm{T}}\Lambda_{u,i}N_i(0)\Lambda_{v,i}. \tag{3.35}$$

This new pre-filter, $K_{v,i}$, achieves the effect of the pre-filter and post-filter described in Eq. (3.33) and still preserves the dynamics within the null space of the rigid body output. The normalization given in Eqs. (3.34) and (3.35) resolves the first issue.

3.3.2.2 An Alternate Method for Receding Horizon Implementation

The second issue (i.e., inconsistent internal states for the various null space filters $N_i(s)$) makes the most noticeable impact during the receding horizon approach for determining the null space variable trajectory by quadratic programming. Specifically, when moving from one implementation interval to the next, continuity of the internal state of the closed-loop system must be maintained using the initial conditions. When considering this LA system, as shown in Fig. 3.1, one can see that there are two different ways to relate the signal from the control allocator to the rest of the system, and thus there are two options for maintaining continuity between implementation intervals of the system. One method is to consider the null space variable, $v(t)$, as the external input signal; this approach was used in Section 3.2.2. The other method is to consider the $\Delta u(t)$ signal as the external input.

The former option integrates the dynamics of the null space filter as a part of the closed loop system, and thus requires that the internal state of the null space filter be maintained to ensure continuity of the system output when advancing from one implementation interval to the next in the receding horizon implementation. This option may cause issues as the LPV null space filter transitions from one basis to another, as dictated by changing flight conditions. For example, suppose a null space variable trajectory $v_k(t)$ for implementation interval k is based on $N_3(s)$ and its corresponding $G_3(s)$ aircraft model (as dictated by the value of the parameter q at the beginning of interval k). Then if the value of q at the beginning of implementation interval $k+1$ dictates a shift of dynamics to $G_4(s)$ and $N_4(s)$, using the value of the internal state of the $N_3(s)$ system as the initial condition for the predictive simulation with the $N_4(s)$ system may result in unanticipated dynamics because the internal states of these two null space filters are inconsistent.

The latter option maintains the $\Delta u(t)$ trajectory between implementation intervals, which is determined by passing the $v(t)$ signal through the appropriate null space filter according to the value of parameter q (i.e., running a linear simulation for $\Delta u = N_i(s)v$). This shift from using $v(t)$ to $\Delta u(t)$ as one of the primary inputs to the system in controlling the flexible output, $y_f(t)$, has the added benefit that the initial condition for new implementation intervals has a physical meaning because it is the extra utilization of the control effectors resulting from the $\Delta u(t)$ signal. To accommodate this change, several modification are necessary starting from Eq. (3.25). Let $y_f(t)$, $t \geq 0$, denote the time-domain solution of the flexible output of the aircraft model, i.e.,

$$y_f(t) = y_{f_0}(t, x_{\mathrm{CL}}(0)) + y_{fr}(t, r(t)) + y_{fg}(t, g(t)) + y_{f\Delta u}(t, \Delta u(t)), \tag{3.36}$$

where $y_{fr}(t)$ is the component of the flexible output from the reference signal, and $y_{fg}(t)$ and $y_{f\Delta u}(t)$ are similar components from the gust and incremental control input signals, respectively. The $y_{f_0}(t, x_{\mathrm{CL}}(0))$ component of the flexible output is based on the initial condition of the closed loop internal state $x_{\mathrm{CL}}(0)$, which includes states from the aircraft model and the nominal controller. Setting Eq. (3.36) in relation to the load bounds yields the following constraints:

$$\begin{aligned} & y_f^- \leq y_f(t) \leq y_f^+ \Leftrightarrow \\ & y_{f\Delta u}(t, \Delta u(t)) \geq y_f^- - y_{f_0}(t, x_{\mathrm{CL}}(0)) - y_{fr}(t, r(t)) - y_{fg}(t, g(t)), \\ & y_{f\Delta u}(t, \Delta u(t)) \leq y_f^+ - y_{f_0}(t, x_{\mathrm{CL}}(0)) - y_{fr}(t, r(t)) - y_{fg}(t, g(t)). \end{aligned} \tag{3.37}$$

Using the receding horizon approach described in Section 3.2.2, the trajectory for $\Delta u(t)$ is indirectly calculated over the preview horizon, by determining a minimum

$v(t)$ and then passing it through the null space filter (with zero initial conditions) to obtain $\Delta u(t)$, i.e., $\Delta u = N_i(s)v$, subject to the constraints in Eq. (3.37). Computationally, this reduces to a QP problem. As described before, only the first few time steps of that solution are applied to the system. In this way, the entire maneuver over the time interval $[0, T_{\text{man}}]$ is iteratively constructed.

As in Section 3.2.2, a computationally efficient solution is obtained when the objective function to be minimized is chosen as the square of the 2-norm of the difference $\delta\Delta u_k(t)$ relative to an assumed incremental control trajectory $\Delta u_{a,k}(t)$, i.e.,

$$\begin{aligned} \Delta u_k(t) &= \Delta u_{a,k}(t) + \delta\Delta u_k(t) \\ &= \Delta u_{a,k}(t) + N_i v_k(t) \end{aligned} \tag{3.38}$$

for $kT_i \leq t \leq kT_i + T_p, k = 0, 1, 2, \ldots$. The nominal trajectory of $\Delta u_{a,k}(t)$ for $k = 0$ is zero and for $k \geq 1$ is informed by the trajectory of $\Delta u_{k-1}(t)$ as

$$\Delta u_{a,k}(t) = \begin{cases} \Delta u_{k-1}(t + T_i), & 0 \leq t \leq T_p - T_i, \\ \Delta \tilde{u}_{a,k}(t), & T_p - T_i \leq t \leq T_p, \end{cases} \tag{3.39}$$

where $\Delta\tilde{u}_{a,k}(t)$ is a linear function of time with boundary values $\Delta u_{k-1}(T_p)$ and zero.

Inserting Eq. (3.38) into Eq. (3.37) shows how $v_k(t)$ is used to indirectly alter $\Delta u_{a,k}(t)$ based on the constraint violations arising from the $\Delta u_{a,k}(t)$ trajectory. Specifically, the load constraints can now be expressed in a form which is convenient for use in a QP problem, i.e.,

$$\begin{aligned} \underbrace{G_{fu,i}N_i}_{H_{fv,i}} v(t) &\geq y_f^- - y_{f0}(t, x_{\text{CL}}(0)) - y_{fr}(t, r(t)) - y_{fg}(t, g(t)) - y_{f\Delta u_a}(t, \Delta u_a(t)), \\ \underbrace{G_{fu,i}N_i}_{H_{fv,i}} v(t) &\leq y_f^+ - y_{f0}(t, x_{\text{CL}}(0)) - y_{fr}(t, r(t)) - y_{fg}(t, g(t)) - y_{f\Delta u_a}(t, \Delta u_a(t)), \end{aligned} \tag{3.40}$$

where there is a corresponding $H_{fv,i}$ system based on each linear model used to define the linear parameter varying model of the aircraft system and the corresponding null space filter for that model.

When using a discrete-time format, filtering v_k with $H_{fv,i}(s)$ is represented by the multiplication of Toeplitz matrix $\mathbf{H}_{fv,i}$ and $\mathbf{v}_k$, as detailed in Section 3.1.2. Therefore, this leads to the following QP problem:

$$\begin{aligned} \min_{\mathbf{v}_k} \quad & \mathbf{v}_k^{\mathrm{T}}\mathbf{v}_k, \\ \text{s.t.} \quad & \mathbf{H}_{fv,i}\mathbf{v}_k \leq y_f^+ - \mathbf{y}_{f0,k} - \mathbf{y}_{fr,k} - \mathbf{y}_{fg,k} - \mathbf{y}_{f\Delta u_a,k}, \\ & -\mathbf{H}_{fv,i}\mathbf{v}_k \leq -y_f^- + \mathbf{y}_{f0,k} + \mathbf{y}_{fr,k} + \mathbf{y}_{fg,k} + \mathbf{y}_{f\Delta u_a,k}. \end{aligned} \tag{3.41}$$

Before solving Eq. (3.41) for each implementation interval k, the current state of the aircraft system is observed to determine the value of the parameter defining the LPV model such that the appropriate $H_{fv,i}$ is used.

3.3.3 Closing Remarks on the Parameter-Varying Load Alleviation System

The investigation of adapting the LA system for use with an LPV aircraft model and the utilization of an LPV null space filter was beneficial in revealing difficulties that may arise from such an approach. In particular, the process is more involved than in traditional controller gain scheduling. Two approaches were used to apply the LA system to an LPV aircraft model.

The first approach was to use one invariant null space filter generated from the linearized aircraft model at the initial flight condition and apply it to the LPV aircraft throughout the dynamic control allocation process (see Section 3.3.1). This approach allows a mismatch of dynamics as the aircraft operates away from the initial flight condition and must rely on state updates from the iterative receding horizon approach to account for this model mismatch. The results from the numerical investigation of this approach will be presented in Section 4.6.

The second approach was to design an LPV null space filter with dynamics which varied along with those of the LPV aircraft in order to minimize model mismatch (see Section 3.3.2). The results from the numerical investigation of this approach will be presented in Section 4.7. Both of these results use the same maneuver to allow a direct comparison of these two approaches.

As observed in the numerical results, both approaches satisfactorily met the primary objective of load alleviation. However, the added complexity of arranging an LPV null space filter reduced the performance of the LA system in meeting its secondary objective of not affecting the rigid body output. In addition to the system performance in this case, when considering the degree of change in dynamic pressure needed to have a significant effect on the dynamics of the aircraft system and the short time duration of maneuvers and gust disturbances, the use of an LPV null space filter system may not be warranted. Throughout the entire flight envelope of an aircraft, there will be a need for several null space filters, but the spacing of these null space filters would be distinct enough that their arrangement in an LPV system would not be necessary. This evidence suggests that the simpler design of using an invariant null space filter is sufficient for alleviating loads for an LPV aircraft model and will therefore be used for the next step of adapting this LA system for a nonlinear aircraft representation.

3.4 Adapting the Load Alleviation System for Use with Nonlinear Systems

The next step in this work to prepare the LA system for use with more realistic aircraft representations is to consider its implementation on a nonlinear system. As shown in Eq. (3.41), the constraints of the QP problem shape the $v(t)$ signal that will control the flexible output. The right-hand side of the constraints is informed by a comparison of the predicted trajectory of $y_f(t)$ to the flexible limits of the structure. The left-hand side of the constraints is informed by the dynamics of the combined system of the null space filter and aircraft model. Motivated by the conclusions made in Section 3.3.3, this development will focus on the application of a linear-based LA system to a nonlinear aircraft model.

Specifically, for maneuvers and gust disturbance encounters beginning at a given equilibrium condition, a linearized model of the aircraft at that condition is used to generate a null space filter. That combination of the linearized model, corresponding null space filter, and nominal controller are used to allocate the controls with the ultimate objective of alleviating the critical loads of the nonlinear aircraft. The University of Michigan's Nonlinear Aeroelastic Simulation Toolbox (UM/NAST), which uses a strain-based formulation to model elastic dynamics of aerospace structures in free flight [54], will be used to represent the nonlinear dynamics of the system. This software program includes various modules used to determine input settings for stable flight conditions, analyze structural modes, or to create linearized versions of the nonlinear models. UM/NAST also has modules to run static or dynamic nonlinear simulations and can also be coupled with controllers defined using C++, Python, or MATLAB [55, 56].

3.4.1 Implementing Load Alleviation in Nonlinear Simulations

For a nonlinear aircraft model, the LA system will continue to utilize a receding horizon approach for numerical demonstrations. However, the same method used to execute the receding horizon approach in the linear simulations could not be used for the nonlinear dynamic simulations using UM/NAST. Specifically, a nonlinear simulation could not be started and seamlessly pick up from where a previous simulation was left off (using UM/NAST v.4.0.2), as was done using MATLAB and Simulink for the linear simulations. Therefore the receding horizon approach is adapted so that it can be contained within a function used by the nominal controller in order to determine the optimal $\Delta u(t)$ signal for the prediction horizon, T_p, but only implement the first time step of the solution (i.e., the implementation interval is set to one time step, $T_i = T_s$). This adaptation aligns the receding horizon approach with standard methods of MPC.

In order to use MPC when applying the LA system to a nonlinear model, the notional preview simulation and the quadratic programming optimization portions of the system are compiled into a separate function that is used by the nominal controller. This control allocator (CA) function requires the current value of the full state of the nonlinear aircraft model, the current state value of any integrators used in the nominal controller, the time discretization, the value of prediction horizon, T_p, and a priori knowledge of the reference command trajectory and gust disturbance over the prediction horizon of length T_p. The CA function also uses a library of pre-calculated systems and variables for use by the optimization. This library includes an LTI model for the flexible aircraft and its state, linearized about the flight condition at the beginning of the simulation, and the corresponding model for the null space filter based on that aircraft model. The library also includes a representation of the closed loop dynamics of the aircraft coupled with the nominal controller which gives the flexible output, $y_f(t)$, for a given reference command trajectory input, $r(t)$ and gust disturbance, $g(t)$ (see Appendix B). The library also includes matrices used to represent the aircraft model coupled with the null space filter in Toeplitz form, for use in the quadratic programming problem. The CA function maintains its own reckoning of the current state of the $\Delta u(t)$ trajectory, in order to maintain continuity between each time step. The controller state is coupled with the current aircraft state to define the closed loop state initial condition.

The CA function begins with an assumed $\Delta u_a(t)$ trajectory over the prediction horizon T_p, which is how the continuity of this signal is maintained between time steps. When initialized, this assumed trajectory is just zeros, but is afterward replaced by the optimal solution from the QP solver. The previews of $r(t)$ and $g(t)$ are concatenated and used as an input in a notional linear simulation of the closed-loop system of the aircraft coupled with the nominal controller to predict the flexible output $y_f(t)$ for the preview horizon, T_p. The $\Delta u_a(t)$ trajectory is also used as an input for the aircraft model to predict the corresponding component of $y_f(t)$ over the prediction horizon of length T_p. These components are added together to find the combined prediction of $y_f(t)$ resulting from $r(t)$, $g(t)$, and the assumed $\Delta u(t)$ trajectory. This prediction comprises the right-hand side of the constraints in Eq. (3.41).

The CA function then checks to see if the predicted $y_f(t)$ exceeds the user-specified constraint on the flexible output. If the constraint is violated at any time within the prediction horizon T_p, then the QP solver is used to determine an optimal $v(t)$ trajectory that will keep $y_f(t)$ within the imposed constraints based on the solution of Eq. (3.41) (assuming a feasible solution exists). The optimal $v(t)$ trajectory is used as an input for the null space filter to obtain a corrective $\delta\Delta u(t)$ trajectory which is combined with the $\Delta u_a(t)$ trajectory to determine the final $\Delta u(t)$ trajectory. On the other hand, if the predicted $y_f(t)$ does not exceed the user-specified constraint, then the $\Delta u_a(t)$ trajectory is used as the final $\Delta u(t)$ trajectory. As with standard MPC, only the first time step of the optimal $\Delta u(t)$ trajectory is returned to the nominal controller and is added to the $u_0(t)$ value determined by the nominal control law (as shown in Fig. 3.2) to alleviate the loads. In subsequent uses of the CA function, the remainder of the final $\Delta u(t)$ trajectory is retained in memory to be used as the $\Delta u_a(t)$ trajectory for the next iteration of the CA function.

3.4.2 Disengagement of the Load Alleviation System

This LA system is designed to introduce an additional input signal to alleviate loads when needed, but then to also disengage by removing the signal when it is not needed. There are a couple of different options for disengaging the system, which go along with the options for maintaining continuity discussed in Section 3.3.2.2. If continuity is maintained by the internal state of the null space filter, then setting the trajectory of the null space variable equal to zero would allow the initial condition of the internal state to decay according to the dynamics of the null space filter. If the continuity is maintained by the $\Delta u(t)$ signal, then some other decay process must be prescribed to disengage the system.

Regardless of which option is used, during implementation, only the first time step of the trajectory is used in the iteration in which it was developed. The remaining time steps of the trajectory may be retained in memory to provide a starting point for subsequent iterations of the CA function. However, one additional time step of values needs to be appended to the retained trajectory in order to run the necessary nominal prediction simulations used by the MPC. The value of this last time step of the prediction can have a great effect on the overall performance of the system, especially since any deviation from this value is penalized during the QP process. Since the overall objective of the LA system is to introduce a $\Delta u(t)$ only when necessary, the value for this last time step should represent an overall reduction to zero, for each input channel. Therefore, the value for the next-to-last time step is multiplied by a scalar value between zero and one and appended as the final time step in order to have enough time steps for a notional prediction for the entire T_p.

When using the internal state of the null space filter to maintain continuity, the $v(t)$ trajectory can reduce to zero very quickly, because the non-zero initial state of the null space filter will still provide continuity to the system. Therefore, the $v(t)$ trajectory from one iteration does not necessarily need to be retained for subsequent iterations. If the trajectory is retained, the value of the next-to-last time step may be multiplied by small scalar values or even zero (e.g., 0.0-0.5) to prescribe the last time step of the preview horizon. Repeating this procedure for each iteration results in an immediate or rapid exponential reduction of the $v(t)$ trajectory to zero. Processing this result through the null space filter reduces the $\Delta u(t)$ trajectory according to the dynamics of the null space filter, assuming that the null space filter dynamics are stable. If the dynamics of the null space filter are unstable, then it can still be used in combination with the flexible output of the aircraft to solve the QP problem and to generate a $\Delta u(t)$ trajectory. However, maintaining system continuity using the state of an unstable null space filter may result in an inability to disengage the LA system.

When using the $\Delta u(t)$ signal to maintain system continuity, the values of this signal are directly connected to activation of the aircraft control effectors, since the signal is downstream from the null space filter. This means that the decay of this signal may adversely affect the rigid body output of the system. Therefore, care should be taken to reduce the trajectory gradually in order to minimize the effect on the rigid body output of the aircraft. If a previous $\Delta u(t)$ trajectory is retained, the value of the next-to-last time step may be multiplied by a scalar value, $k_{\Delta u}$ to prescribe the last time step of the preview horizon, i.e.,

$$\Delta u_{a,k}(t) = \begin{cases} \Delta u_{k-1}(t+1), & 0 \leq t \leq T_p - 1, \\ k_{\Delta u} \Delta u_{k-1}(t), & t = T_p. \end{cases} \tag{3.42}$$

If no further optimization of the $\Delta u(t)$ trajectory is needed in subsequent iterations of the CA function, this iterative scaling down of the final time step results in an exponential decay of the $\Delta u(t)$ trajectory and a disengagement of the LA system. If a previous $\Delta u(t)$ trajectory is not maintained, then a trajectory must be generated which provides a decay of the signal over the preview horizon. Again, iterative scalar reduction of the signal results in an exponential decay of the LA system. The magnitude of the scalar value affects the rate of exponential decay. If the magnitude is too small, the signal will be removed too rapidly, which may result in large oscillations of $y_r(t)$. If the magnitude is too large, the LA system will remain engaged much longer than necessary or may result in too much compensation being used, which may drive the system unstable in the case of an unstable null space filter. Therefore, a magnitude within the range of 0.8 to 0.98 may provide the most desirable disengagement of the LA system, while minimizing adverse effects to the rigid output.

3.5 Final Configuration of Load Alleviation System

The final configuration of the LA system using CA for a nonlinear aircraft model consists of a CA function using MPC that is called by the nominal controller of the aircraft at every time step. The nominal controller and CA function are MATLAB scripts that can connect with the Python interface for UM/NAST. The nominal controller receives a sensor feedback signal, $y_r(t)$, from a sensor specified in UM/NAST and linked to the model and dynamic solver object. The reference command signal, $r(t)$, and gust disturbance signal, $g(t)$, are contained in lookup tables in a database, which is accessed by the nominal controller. The sensor data and reference signal are used according to the control law to generate a nominal control signal, $u_0(t)$. The nominal controller must also use the CA function to obtain the Δu vector.

The nominal controller provides the CA function with the current full state of the aircraft, the current values of the controller integrator states, a preview (with duration T_p) of the gust disturbance signal, $g(t)$, and a preview of the reference command signal, $r(t)$, dictating the maneuver. The CA function also accesses a library with linearized models of the aircraft, the null space filter, and the closed loop system of the aircraft with the nominal controller. The library also contains the trim values of the full state of the aircraft and matrices used to represent the aircraft model coupled with the null space filter in Toeplitz form, for use in the quadratic programming problem. The CA function maintains its own reckoning of the current state of the $\Delta u(t)$ trajectory, in order to maintain continuity between each time step.

The CA function first generates an assumed $\Delta u_a(t)$ trajectory for the given T_p, which is carried over from the previous iteration. The previews of $r(t)$, $g(t)$, and the $\Delta u_a(t)$ trajectories are used in a notional linear simulation to predict the flexible output trajectory $y_f(t)$ for the preview horizon. If the prediction shows that $y_f(t)$ will exceed the constraints, then the optimization function is triggered in order to alleviate the loads. The optimization function begins with the predicted $y_f(t)$ and uses QP to find a null space variable trajectory, $v(t)$, that will adjust the $y_f(t)$ trajectory to keep it within the constraints. The $v(t)$ solution is then run through a linear simulation with the null space filter dynamics to generate the $\delta\Delta u(t)$ trajectory. This is then added to the assumed trajectory to form the $\Delta u(t)$ trajectory for that iteration (i.e., $\Delta u(t) = \Delta u_a(t) + \delta\Delta u(t)$). If the prediction shows that $y_f(t)$ will not exceed the constraints, then $\Delta u(t) = \Delta u_a(t)$. The first time step value of $\Delta u(t)$ is returned to the nominal controller as the output of the CA function. The remaining time steps of $\Delta u(t)$ are retained in memory to be used as $\Delta u_a(t)$ for the next iteration, with the values in the last time step scaled down, as shown in Eq. 3.42, with $k_{\Delta u} = 0.95$. This process repeats every time step. Therefore, the CA function is either following a previously determined $\Delta u(t)$ solution which will decay at the end, or refining the $\Delta u(t)$ trajectory to correct predicted constraint violations.

Finally, after the nominal controller receives the Δu vector from the CA function, with an entry for each control channel, it adds the values of Δu to their appropriate control channels. These combined signals are then bounded by the maximum deflection values and then returned to the UM/NAST simulation.

CHAPTER 4

Numerical Investigation and Results for Load Alleviation System

This chapter presents numerical results for the LA system throughout the build-up approach. The two aircraft models used for numerical simulations of the LA system are described (i.e., the X-HALE and the GTA). Each aircraft model is described generally, and then in more detail for the flight conditions used to investigate the feasibility of the LA system concept. Numerical results are then presented as a proof of the LA system concept, starting with linear-based simulations and then building up to nonlinear dynamic simulations.

4.1 Aircraft Models used for Numerical Demonstration

The methods for LA discussed and derived in this work are numerically demonstrated using a couple of aircraft models. Each of these models are firstly defined in a nonlinear fashion, for use with UM/NAST, and linearized versions are generated to define an LA system for each.

4.1.1 X-HALE Model

The first aircraft model used for numerical demonstration is the X-HALE aircraft [43]. As illustrated in Fig. 4.1, the X-HALE is equipped with four elevators ($T_{L1}, T_{L2}, T_{R1}, T_{R2}$), two roll spoilers ($R_L, R_R$), and five thrusters ($P_0, P_{L1}, P_{L2}, P_{R1}, P_{R2}$). In total, this comprises eleven control inputs to the system, i.e., $n_u = 11$. Accordingly, the control input u is defined as

$$u = \begin{bmatrix} R_L & R_R & T_{L1} & T_{L2} & T_{R1} & T_{R2} & P_0 & P_{L1} & P_{L2} & P_{R1} & P_{R2} \end{bmatrix}^{\mathrm{T}}. \tag{4.1}$$

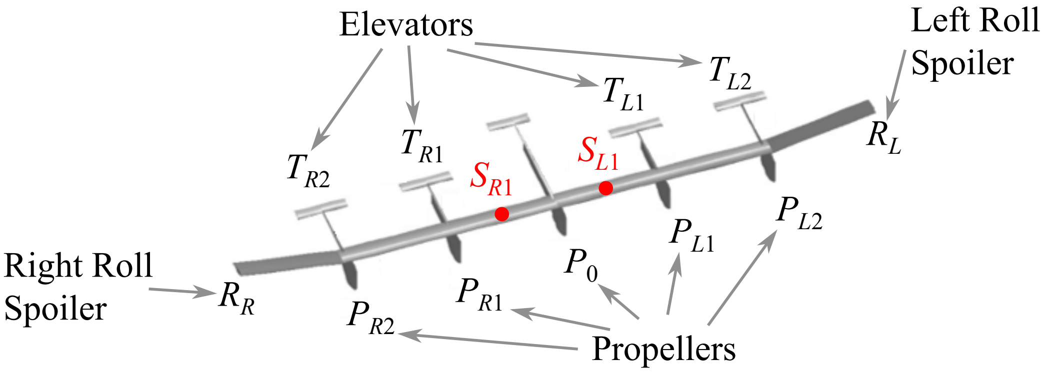

Figure 4.1: Control inputs and critical stations on X-HALE

The vector of rigid body outputs to be controlled consists of the roll, pitch, and yaw angular rates, i.e.,

$$y_r = \begin{bmatrix} p & q & r \end{bmatrix}^{\mathrm{T}}, \tag{4.2}$$

which means that $n_r = 3$. With $n_u > n_r$, the X-HALE has the characteristics to support weak input redundancy established by Eq. (2.5).

The critical stations to evaluate the flexible outputs are defined as S_{L1} and S_{R1}, see Fig. 4.1. The vector of flexible outputs, y_f, is composed of the out-of-plane bending curvatures at the critical stations, i.e.,

$$y_f = \begin{bmatrix} \kappa_{L1} & \kappa_{R1} \end{bmatrix}^{\mathrm{T}}. \tag{4.3}$$

The stiffness of the X-HALE was numerically doubled with respect to the actual aircraft so that the resulting model is representative of flexible rather than very flexible aircraft (see Appendix C for details). This limits the shape deformation and is synergistic with the assumption of linear structural dynamics. A linearized model is generated at a trimmed condition of straight, level, unaccelerated flight using UM/NAST. The trim airspeed is 14 m/s, with an angle of attack of 1.8° at an altitude of 30 m. This is a typical flight condition of X-HALE. At this condition, the wings already have a deformed shape, with an out-of-plane curvature of $-0.052\ \mathrm{m}^{-1}$ at both inboard wing sections S_{L1} and S_{R1} (negative curvature indicates an upward bend). The curvature for each of the mid-wing sections is $-0.022\ \mathrm{m}^{-1}$. The outboard wing sections have a curvature of $-0.007\ \mathrm{m}^{-1}$. Since the steady-state curvature values at the inboard wing sections are larger, those sections were selected as the critical stations of the structure.

The frequency response of the linearized flexible aircraft is shown in Fig. 4.2. Most peaks in Fig. 4.2 correspond to the structural modes of the flexible X-HALE aircraft. Note that the first three rows correspond to the rigid body response (i.e., p, q, r) while the last two rows correspond to the out-of-plane curvature κ_{L1} and κ_{R1} at critical stations S_{L1} and S_{R1}, respectively. The three columns illustrate the control inputs from roll spoilers, elevators, and thrusters, respectively. The left and right roll spoilers affect the rigid body response at almost identical magnitudes, their slight difference arises from the geometric distance difference from the roll spoilers to S_{L1}. The elevators affect the pitch rate q in a very similar way, but the outside elevators T_{L2} and T_{R2} are more capable of introducing roll and yaw compared to the inside elevators due to additional moment. This spatial distribution also affects the response of the thrusters: the outside thrusters P_{L2} and P_{R2} are more capable of affecting roll, yaw

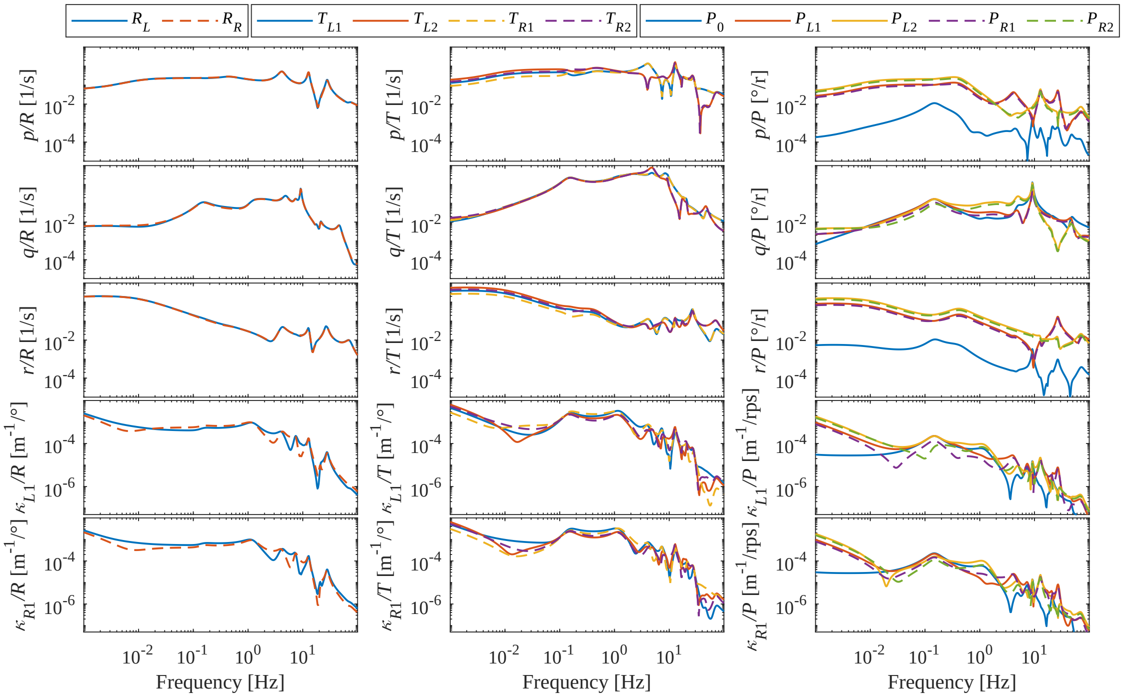

Figure 4.2: Frequency response of linearized X-HALE model

and bending curvature, while the central thruster P_0 provides significantly less effect on these outputs. It is also noteworthy that the elevators affect bending curvature more significantly compared to other control inputs. This property may be exploited in the process of control allocation.

4.1.2 X-HALE Configuration and Nominal Control

The LA system is first demonstrated using the X-HALE aircraft model in order to prove the functionality of the concept. The nominal controller is adapted from the control structure in [55], and is illustrated in Fig. 4.3. The nominal controller stabilizes the rigid body output of roll, pitch, and yaw rates (i.e., $n_r = 3$) based on pilot input. By observation, the criterion for weak input redundancy given in Eq. (2.5) is satisfied because $n_u > n_r$.

Cascaded Proportional/Proportional-Integral (P/PI) controllers are used to con-

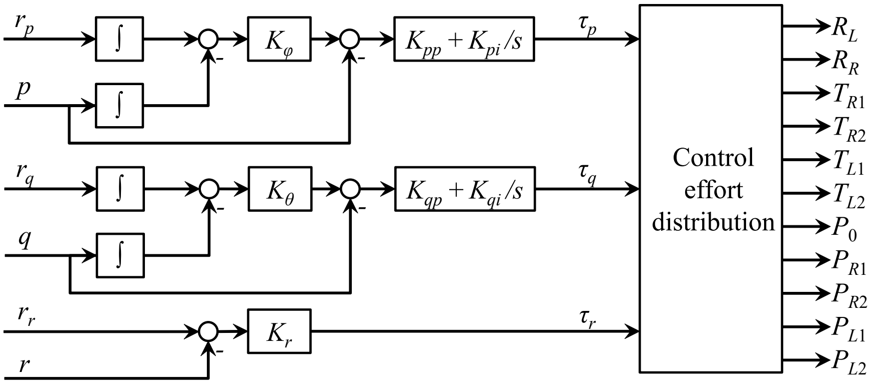

Figure 4.3: X-HALE nominal controller structure

trol the roll and pitch rates, while a proportional controller is used to control the yaw rate. These P/PI and proportional controllers generate τ_p, τ_q, and τ_r, which inform required control actions for roll, pitch, and yaw axes, respectively. Their directions are defined in a way that positive τ_p, τ_q and τ_r induce positive roll, pitch, and yaw motion, respectively. The corresponding gains are provided in Table 4.1. The required control actions are further assigned to each control input as

$$
\begin{aligned}
\begin{bmatrix} R_L \\ R_R \end{bmatrix} &= \begin{cases}
\begin{bmatrix} R_{\max} - R_{\text{trim}} & 0 \end{bmatrix}^{\mathrm{T}} & \text{if } \tau_p \leq -\left(R_{\max} - R_{\text{trim}}\right) \\
\begin{bmatrix} -\tau_p & 0 \end{bmatrix}^{\mathrm{T}} & \text{if } -\left(R_{\max} - R_{\text{trim}}\right) < \tau_p \leq R_{\text{trim}} \\
\begin{bmatrix} -R_{\text{trim}} & \tau_p - R_{\text{trim}} \end{bmatrix}^{\mathrm{T}} & \text{if } R_{\text{trim}} < \tau_p \leq R_{\max} + R_{\text{trim}} \\
\begin{bmatrix} -R_{\text{trim}} & R_{\max} \end{bmatrix}^{\mathrm{T}} & \text{if } R_{\max} + R_{\text{trim}} < \tau_p
\end{cases} \\
T_{L1} &= T_{R1} = \tau_q, \\
T_{L2} &= \tau_q + K_{p,\text{tail}}\tau_p, \\
T_{R2} &= \tau_q - K_{p,\text{tail}}\tau_p, \\
P_0 &= 0, \\
P_{L1} &= P_{L2} = \tau_r, \\
P_{R1} &= P_{R2} = -\tau_r.
\end{aligned}
\tag{4.4}
$$

Note that the original control effort distribution in [55] actuated the four elevators symmetrically for the pitch motion, while adopting differential thrust between the left-side and right-side thrusters for the yaw motion. In comparison to this original approach, two modifications are made. Firstly, the spoiler inputs are asymmetrically defined for the roll motion with four different configurations considering τ_p and the trimmed condition, R_{trim}. Note that the trimmed condition of the roll spoilers is assumed to be a positive deflection of R_L and zero deflection of R_R. This modification arises from the roll spoilers' physical motion range from 0° to 30° ($R_{\max}$). Secondly, the roll control action τ_r (scaled by $K_{p,\text{tail}}$) is routed asymmetrically to the outboard elevators T_{L2} and T_{R2}, to enhance the roll control authority of the aircraft. This nominal controller design already includes a heuristic baseline control allocation structure, which is based on standard manipulation methods of the throttle, roll, pitch, and yaw in stability augmentation systems. Also, this design only uses the feedback of the rigid body angular rates, which satisfies the specification of separating the rigid and flexible outputs y_r and y_f in Fig. 3.1.

Table 4.1: Gains of X-HALE nominal controller

K_ϕ [s^{-1}]	K_{pp} [s]	K_{pi}	K_θ [s^{-1}]	K_{qp} [s]	K_{qi}	K_r[s]	$K_{p,\text{tail}}$
2.5	1.3	3	23	0.01	0.1	200	0.4

Note that the architecture for the nominal controller of the X-HALE is not based solely on an error signal of the difference between a measured output and the reference signal. Therefore, some additional considerations must be made when combining all elements of the system into a closed-loop system (see Appendix A).

4.1.3 Generic Transport Aircraft (GTA) Model

The second aircraft model used for numerical demonstration is the GTA design, modified from [44]. The model has also been used in other recent analysis of flexible aircraft and aeroelasticity [57]. As illustrated in Fig. 4.4, the GTA is equipped with two elevators (ELV_L, ELV_R), two ailerons (AIL_L, AIL_R), one rudder (RDR), two flaps (FLP_L, FLP_R), and two thrusters (T_L, T_R). In total, this comprises nine control inputs to the system, i.e., $n_u = 9$. Accordingly, the control input u is defined as

$$u = \begin{bmatrix} ELV_R & ELV_L & RDR & AIL_R & AIL_L & FLP_R & FLP_L & T_R & T_L \end{bmatrix}^{\mathrm{T}}. \tag{4.5}$$

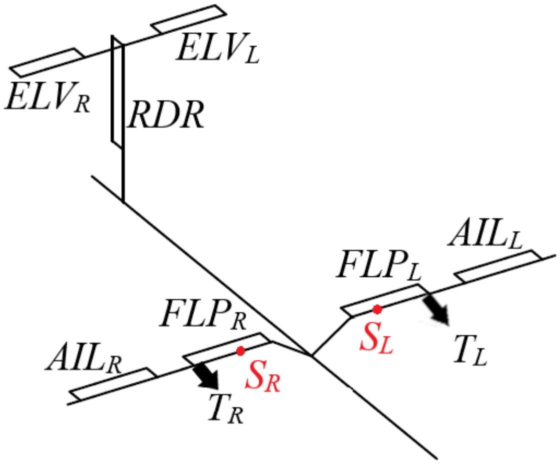

Figure 4.4: Control inputs and critical stations on the Generic Transport Aircraft

Note that the flaps in this model are defined identically to the ailerons, just located close to the fuselage. This means that they are not restricted to only deflect trailing-edge down and are not rate limited to move more slowly than ailerons. The vector of rigid body outputs to be controlled consists of the roll, pitch, and yaw angular rates, i.e.,

$$y_r = \begin{bmatrix} p & q & r \end{bmatrix}^{\mathrm{T}}. \tag{4.6}$$

which means that $n_r = 3$. With $n_u > n_r$, the GTA also has the characteristics to support weak input redundancy established by Eq. (2.5).

The fuselage of the GTA is 22 meters long with a diameter of 2.2 meters. The wingspan is 19 meters, with a constant chord of 2.2 meters, giving it an aspect ratio of 8.6. The critical stations to evaluate the flexible outputs are defined as S_L and S_R, which are 2.25 meters away from the center of the fuselage, see Fig. 4.4. The vector of flexible outputs, y_f, is composed of the out-of-plane bending curvatures at the critical stations, i.e.,

$$y_f = \begin{bmatrix} \kappa_{L1} & \kappa_{R1} \end{bmatrix}^{\mathrm{T}}. \tag{4.7}$$

The stiffness of the GTA wings was numerically reduced from the design originally proposed in [44] so that the resulting model is more flexible and demonstrates geometric nonlinearities for wing bending (see Appendix C for details). A linearized model is generated at a trimmed condition of straight, level, unaccelerated flight using UM/NAST. The trim airspeed is 160 m/s, with an angle of attack of 1.8° at an altitude of 20,000 ft (6096 m). At this condition, the wings already have a deformed shape, with the highest out-of-plane bending curvature occurring at locations S_L and S_R. The curvature for wing locations closer to the fuselage, or for the wing box inside the fuselage, have a much smaller static deflection. The curvature for wing locations further outboard steadily decreases, approaching zero near the wingtip.

4.1.4 Generic Transport Aircraft Configuration and Nominal Control

The nominal controller for the GTA stabilizes the rigid body output of roll, pitch, and yaw rates (i.e., $n_r = 3$) based on a reference signal meant to represent pilot input. By observation, the criterion for weak input redundancy given in Eq. (2.5) is satisfied because $n_u > n_r$. Unlike the nominal controller for the X-HALE, decoupled Proportional-Integral (PI) controllers are used to control the angular rates of each axis. These PI controllers generate τ_p, τ_q, and τ_r, which inform required control actions for roll, pitch, and yaw axes, respectively, i.e.,

$$\begin{aligned} \tau_p &= (K_{pp} + \tfrac{K_{pi}}{s})(r_p - y_p), \\ \tau_q &= -(K_{qp} + \tfrac{K_{qi}}{s})(r_q - y_q), \\ \tau_r &= (K_{rp} + \tfrac{K_{ri}}{s})(r_r - y_r). \end{aligned} \tag{4.8}$$

These signals are directly fed to the control channels identified in Eq. 4.5, deflecting the ailerons asymmetrically (i.e., $AIL_R(t) = -\tau_p(t)$ and $AIL_L(t) = \tau_p(t)$), deflecting both elevators symmetrically (i.e., $ELV_L(t) = ELV_R(t) = \tau_q(t)$), and deflecting the rudder by $\tau_r(t)$. This represents a heuristic baseline control allocation structure. The input channels for the thrusters and flaps are not controlled by the nominal controller, and would just be direct feedthrough from the operator. However, all input channels are available for the CA, through the $\Delta_u(t)$ signal. All control surfaces are given a maximum deflection limit of $\pm 45°$. Note that this design only uses the feedback of the rigid body angular rates, which satisfies the specification of separating the rigid and flexible outputs in Fig. 3.1. The gains of the PI controller are provided in Table 4.2.

Table 4.2: Gains of GTA nominal controller

K_{pp} [s]	K_{pi}	K_{qp} [s]	K_{qi}	K_{rp} [s]	K_{ri}
1	10	0.3	3	3	7

The stiffness values of the wings are reduced from the GTA design presented in [44] for out-of-plane bending, in-plane bending, and torsion. The extensional stiffness values are unchanged and all other components of the model (i.e., fuselage, horizontal tails, and vertical tail) are treated as rigid elements in the UM/NAST framework. With this relaxed stiffness of the wings, at an equilibrium flight condition of 160 m/s at 20,000 ft, the baseline vertical wingtip deflection is 20.0% of half the aircraft wingspan. At this condition, the first out-of-plane bending frequency is 1.37 Hz. As for rigid body flight dynamics, the short period frequency is 0.86 Hz, as determined by numerical simulation, using a high magnitude elevator deflection of $-13°$ for 0.3 second. In terms of the flexible output of the system, the out-of-plane wing bending curvature has a static value of -0.118 1/m at this flight condition. This bending curvature is the main objective for the LA system to control within given structural bounds.

4.2 Gust Model Implementation

A basic B_g matrix was generated by using the direction cosines matrix for the attitude of the aircraft center of gravity at the equilibrium condition. This matrix establishes a connection between the body-fixed frame of reference and the inertial frame of reference, i.e.,

$$O_{BI} = \begin{bmatrix} \mathrm{c}\psi_0\mathrm{c}\theta_0 & \mathrm{c}\theta_0\mathrm{s}\psi_0 & -\mathrm{s}\theta_0 \\ \mathrm{c}\psi_0\mathrm{s}\phi_0\mathrm{s}\theta_0 - \mathrm{c}\phi_0\mathrm{s}\psi_0 & \mathrm{c}\phi_0\mathrm{c}\psi_0 + \mathrm{s}\phi_0\mathrm{s}\psi_0\mathrm{s}\theta_0 & \mathrm{c}\theta_0\mathrm{s}\phi_0 \\ \mathrm{s}\phi_0\mathrm{s}\psi_0 + \mathrm{c}\phi_0\mathrm{c}\psi_0\mathrm{s}\theta_0 & \mathrm{c}\phi_0\mathrm{s}\psi_0\mathrm{s}\theta_0 - \mathrm{c}\psi_0\mathrm{s}\phi_0 & \mathrm{c}\phi_0\mathrm{c}\theta_0 \end{bmatrix}, \tag{4.9}$$

where s· and c· are abbreviations for the sine and cosine functions, respectively. For this matrix, ϕ_0, θ_0, and ψ_0 are the angles for roll, pitch, and yaw, respectively, defining the attitude of the aircraft at the equilibrium condition.

The velocity of the gust disturbance was then assumed to directly add to the rigid body velocity components at the center of gravity, as related through the direction cosines matrix. This influence of gust disturbances from longitudinal, vertical, and lateral directions was then captured in a B_g matrix for three gust disturbance components by inserting Eq. (4.9) into a $n_x \times 3$ matrix of zeros, aligning it with the rigid body velocity components, u, v, and w, of the state vector. By this assumption, the gust velocity directly impacts only the rigid body motion through the aircraft center of gravity. The effect of the gust disturbance on the flexible output results from the structural dynamics captured in the model. As a result, a downward gust increases the out-of-plane wing bending and an upward gust decreases bending. A more accurate way to account for the gust disturbances could be through the analysis of the aerodynamic influence on the lifting surfaces and control surfaces. The theory for such a treatment is detailed in [20], but the functionality for generating a B_g matrix with the UM/NAST linearization module is currently under development.

4.3 Performance Metrics for Numerical Investigations

The following numerical simulations are used to illustrate the operation of the LA system developed in this work. The results are based on linear models, linear parameter-varying models, and nonlinear models. The following performance metrics are defined in order to quantify the performance of the LA system for each model and test case.

The first performance metric describes the amount of correction needed by the LA system in order to attenuate the flexible output within the user-defined bounds when performing the maneuver without the LA system. This metric is expressed as a percentage of the maximum flexible output displacement from the equilibrium value prior to the maneuver or gust disturbance, i.e.,:

$$y_{f,\text{correction}} = \frac{y_f^{-} - \hat{y}_{f\text{min}}}{\hat{y}_{f\text{min}} - y_{f\text{eq}}}, \tag{4.10}$$

where $\hat{y}_{f\text{min}}$ is the minimum observed flexible output from the maneuver without the LA system. $y_{f\text{eq}}$ is the value of the flexible output at the equilibrium condition, before the maneuver is initiated or gust disturbance is encountered.

The next performance metric corresponds to the primary objective of load alleviation and describes the margin between the flexible output and the user-defined constraint during the maneuver or gust encounter. After running a numerical simulation with the LA system engaged, the minimum observed value of the flexible output will be compared to the user-defined constraint. This results in a flexible output integrity metric, expressed as a percentage of the maximum flexible output displacement from the equilibrium value:

$$y_{f,\text{integrity}} = \frac{y_f^{\bar{}} - y_{f\text{min}}}{\hat{y}_{f\text{min}} - y_{f\text{eq}}}, \tag{4.11}$$

where $y_{f\text{min}}$ is the minimum observed flexible output during the maneuver or gust disturbance encounter with the LA system engaged. Any instance where the integrity metric has a value less than zero represents a constraint violation. The closer this value is to zero can be thought of as a measure of optimality, meaning that the LA system adjusted the control allocation enough to meet the constraints, but not to excess.

The final performance metric corresponds to the secondary objective of the proposed LA system: preserving rigid body trajectory tracking performance. A distinguishing feature of the system under evaluation is the exploitation of the null space of the aircraft model which enables changes to the flexible output without affecting the rigid body output. However, this feature relies on the property of superposition present in linear systems, which may not hold across all frequencies during the dynamic simulation. The rigid body output data observed during the maneuver or gust disturbance encounter with the LA system engaged will be compared to the corresponding output data without the LA system engaged throughout the time history data log. Specifically, the difference between the rigid body output values will be calculated starting from the first point in time where the mean $\Delta u(t)$ value of all input channels is greater than zero until the mean $\Delta u(t)$ value returns to zero, or the end of the data log. The mean of the absolute value of these differences will be calculated, resulting in a rigid body output mean absolute error:

$$e_{y_r} = \frac{1}{n}\sum_{i=1}^{n} |y_r(i) - \hat{y}_r(i)|, \tag{4.12}$$

where n is the number of time steps in the sample and $y_r(t)$ and $\hat{y}_r(t)$ represent the rigid body output data from the simulation with and without the LA system engaged, respectively. Ideally, this value should be as close to zero as possible.

4.4 X-HALE Proof of Concept of Load Alleviation System through Control Allocation

The maneuver load alleviation scheme developed in Section 3.1 is demonstrated using the linear X-HALE model and nominal control law from Section 4.1.1. The linearized model of X-HALE is imported into MATLAB and Simulink (ver. R2020a [58]) to make all necessary calculations and produce simulation results. The null space filter is generated using the process described in Section 3.1.1, based on the X-HALE linearized model, and the quadratic programming problem in Eq. (3.20) is established in the load alleviation block, as shown in Fig. 3.1. The curvature bounds on critical stations S_{L1} and S_{R1} are set to $\pm 0.056\,\mathrm{m}^{-1}$. The quadratic programming problem is solved using the active-set method; the computed null space variable, v, is used to establish Δu, which incrementally modifies the control surfaces on top of the nominal controller. Two different maneuvers are considered in the simulations:

1. Climb maneuver: The reference trajectory involves a pitch up three seconds after the simulation starts with a pulse of 8.2°/s, intended to achieve 10° of pitch in one second and holding for six seconds before leveling off in one additional second. This results in a climb of 10 meters.

2. Climbing turn maneuver: The reference trajectory directs to bank the aircraft and change the yaw rate one second after the simulation starts. A pulse of 30°/s

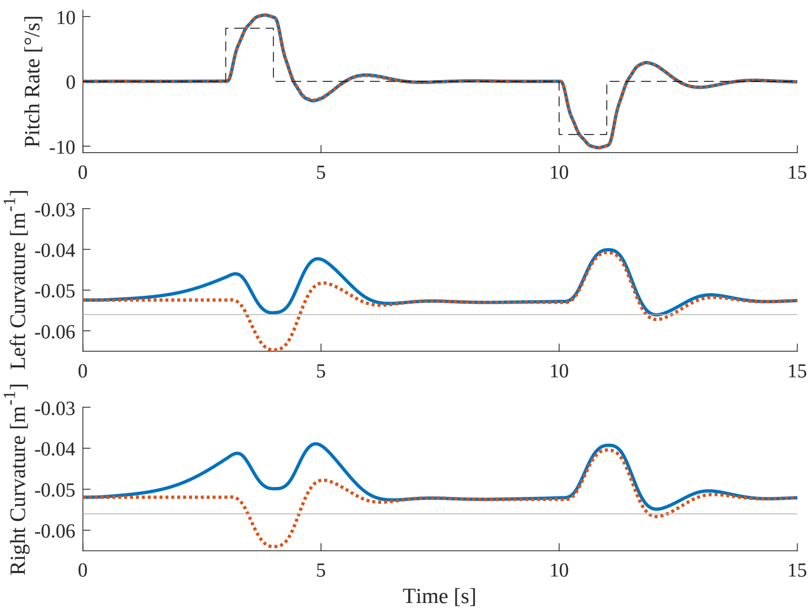

Figure 4.5: Responses of pitch rate and wing root bending curvature for climb maneuver with and without MLA

> is given for the roll rate and a yaw rate of 15°/s is established in one second. The bank angle and yaw rate are held for five seconds before the reference reverses the initial trajectory over one second to return to zero bank angle on a new heading. This results in a target heading angle change of 90°. The longitudinal reference command of the trajectory is the same as in the climb maneuver.

Additional trajectories which did not include a pitch component were explored but did not sufficiently excite the bending curvature beyond the bound. Therefore, the climbing turn maneuver was chosen to demonstrate the functionality of the MLA system for multi-axial maneuvers.

The pitch angle response and the bending curvature at the critical stations are shown in Fig. 4.5. Roll and yaw responses are not shown in Fig. 4.5 since pitch control is designed in a decoupled way, as discussed in Section 4.1.1. This test case requires that the flexible output be attenuated by 68.2%, according to the $y_{f,\text{correction}}$ metric defined in Eq. (4.10).

Note that the bending curvatures κ_{L1} and κ_{R1} violate the specified constraints without LA through control allocation and are kept within the bounds by using the LA system. The flexible output integrity metric from Eq. (4.11) shows positive values for both the left and right critical stations:

$$\begin{aligned} \kappa_{L1,\text{integrity}} &= 3.36\%, \\ \kappa_{R1,\text{integrity}} &= 26.7\%. \end{aligned} \tag{4.13}$$

The smaller of these values being close to zero represents that a near-optimal solution was found. The curvatures with LA converge to the curvatures without LA in regions where constraints are not violated. This is consistent with the objective function in Eq. (3.20), where changes to the nominal control signal are being minimized.

Note that the pitch response with and without the LA appear identical, indicating that the trajectory tracking performance is not affected by LA. Indeed, the mean absolute errors (from Eq. (4.12) for roll-, pitch-, and yaw-rates over the first 8 seconds of the simulation are all less than 0.05°/s:

$$\begin{aligned} e_p &= 0.008^\circ/\text{s}, \\ e_q &= 0.031^\circ/\text{s}, \\ e_r &= 0.007^\circ/\text{s}. \end{aligned} \tag{4.14}$$

This benefit arises from utilizing the null space which exploits the weak input redundancy of the system.

The time histories of the elevator and roll spoiler inputs are shown in Fig. 4.6. The incremental changes to the thruster inputs were less than one percent of the normalized throttle signal and, therefore, are not shown. The control inputs of the inner elevators (T_{L1} and T_{R1}) are decreased to reduce the bending curvature at the wing root while the deflection of the outside elevators (T_{L2} and T_{R2}) is increased. The roll spoilers are also engaged symmetrically to move the lift away from the wing tips.

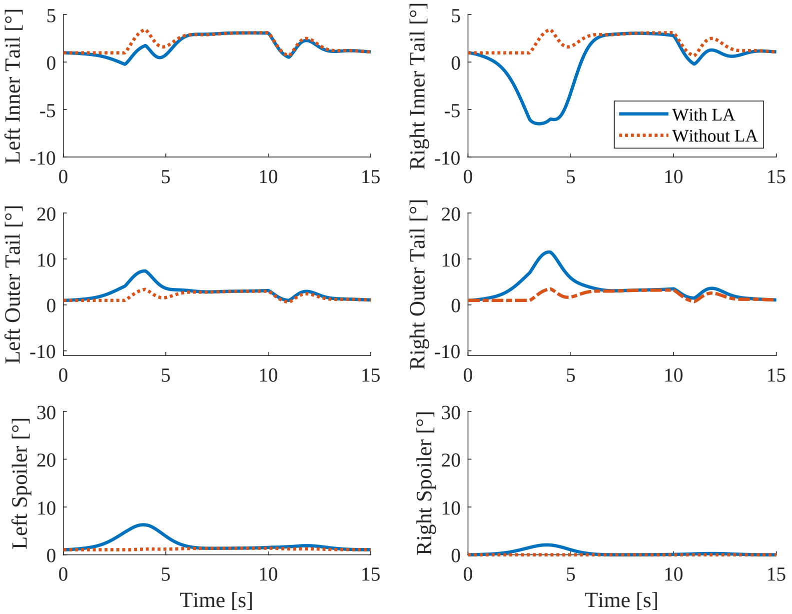

Figure 4.6: Time histories of elevator and roll spoiler inputs for climb maneuver with and without MLA

This redistribution of lift may at first seem counter-intuitive compared to traditional MLA systems where most of the control efforts are redistributed to the inward control surfaces. However, this behavior aligns with the fact that the X-HALE model has straight wings, with no taper. Also, the X-HALE mass is distributed across the wingspan, in contrast to the heavy fuselage in commercial aircraft. Therefore, the changes result in a more distributed lift profile throughout the middle two-thirds of the wing, rather than the center. Note the proposed method assumes a prediction horizon T_p which is equal to the duration of the simulation in this proof of concept investigation. Using a prediction horizon results in incremental changes to the control input that start to reduce the bending curvature before the maneuver is commanded, in anticipation of the large change in curvature caused by the pitch-up motion.

The tracking performance and the flexible outputs at the critical stations for the climbing turn maneuver are shown in Fig. 4.7. The pitch response is similar to the first maneuver, which confirms the decoupled design of the nominal controller was not

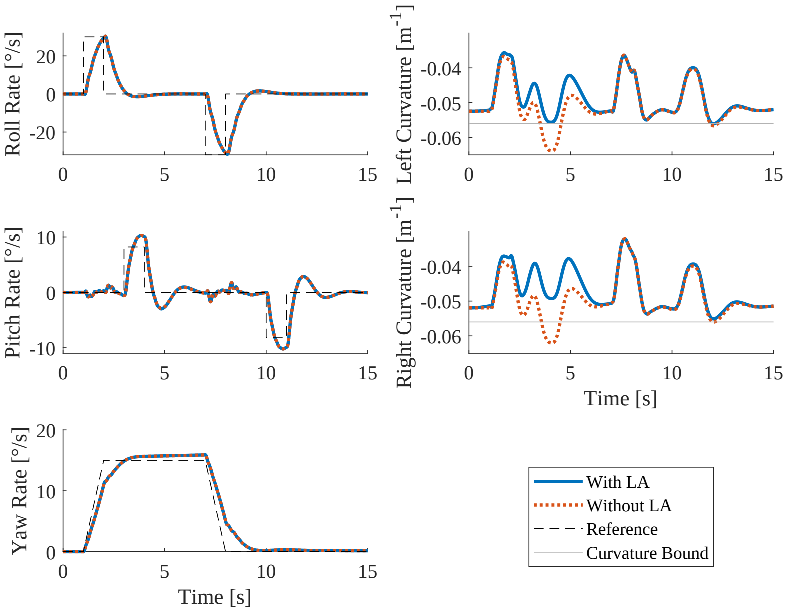

Figure 4.7: Responses of rigid body motion and wing root bending curvatures for climbing turn maneuver with and without MLA

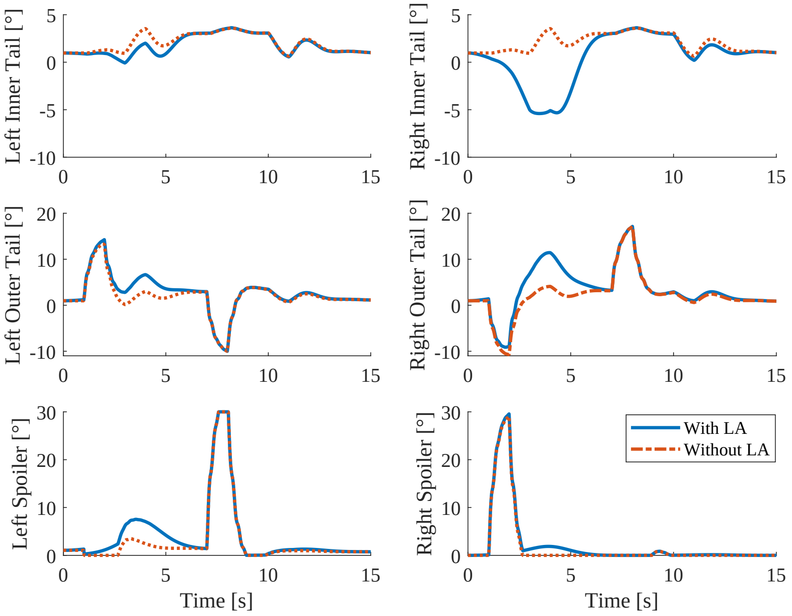

Figure 4.8: Time histories of elevator and the roll spoiler inputs for climbing turn maneuver with and without MLA

compromised by the control allocation. This test case has a flexible output correction factor of $y_{f,\text{correction}} = 66.0\%$. The bending curvature dynamics are restricted within bounds by the proposed approach:

$$\begin{aligned} \kappa_{L1,\text{integrity}} &= 3.21\%, \\ \kappa_{R1,\text{integrity}} &= 34.0\%. \end{aligned} \tag{4.15}$$

As in the climb test case, the mean absolute errors of the rigid body outputs over the first 8 seconds of the simulation are all less than 0.05°/s:

$$\begin{aligned} e_p &= 0.007^\circ/\text{s}, \\ e_q &= 0.028^\circ/\text{s}, \\ e_r &= 0.007^\circ/\text{s}. \end{aligned} \tag{4.16}$$

The time histories of the tail and roll spoiler inputs are shown in Fig. 4.8. At the beginning of the maneuver, the left roll spoiler, which is not heavily used by the nominal controller at this instant, is engaged to alleviate the load. During this maneuver, the inner elevators (T_{L1} and T_{R1}) have more negative deflection to reduce the bending curvature at the wing root while the deflections of the outside elevators (T_{L2} and T_{R2}) are increased. This also arises from the redistribution of lift forces to the outside control surfaces, due to the same reasons as for the first maneuver.

4.5 Numerical Investigation of Load Alleviation System with Gust Disturbance and Limited Preview

The enhancements to the LA system, including gust disturbances and limited preview, as described in Section 3.2, are investigated using numerical simulations. The linearized model of X-HALE is imported into MATLAB and Simulink (ver. R2016a

[48]) to make all calculations and produce simulation results.

Four general test cases with increasing complexity (i.e., discrete gust, continuous gust, longitudinal maneuver with gust, and multi-axis maneuver with gust) were used for this demonstration.

1. Discrete gust encounter: The aircraft encounters a discrete downward gust with a $1-$cosine profile. The gust is encountered two seconds after the simulation starts, swelling to a peak gust amplitude of $U_0 = 2.0$ m/s and then decaying to zero over two seconds (i.e., $t_{\text{gust}} = 2$ s). No maneuver is provided for this case, i.e., the controller aims to maintain straight and level flight.

2. Dryden turbulence encounter: The aircraft is flying in a turbulence field characterized by a Dryden model. No maneuver is provided for this case, i.e., the controller aims to maintain straight and level flight.

3. Descent with turbulence: The aircraft is descending to a lower altitude in the presence of turbulence characterized by the Dryden model. The reference trajectory consists of a pitch down two seconds after the simulation starts with a pulse of $-7.8°/\text{s}$, intended to achieve $-6°$ of pitch in one second (equilibrium condition pitch attitude is $+1.8°$). The nose-down pitch attitude is held for four seconds before leveling off in one additional second. This maneuver results in a descent of 10 meters.

4. Descending turn with turbulence: The aircraft is descending while executing a right turn in the presence of turbulence characterized by the Dryden model. The reference trajectory initiates the turn one second after the simulation starts. A reference pulse of 30°/s is given for the roll rate and a reference yaw rate of 15°/s is established in one second. The bank angle and yaw rate are held for six seconds before the reference reverses the initial signal over one second to return to zero bank angle on a new heading. This results in a target heading

angle change of 105°. The descent portion of the trajectory is the same as in the descent maneuver.

The time signal for the discrete gust used for simulation was generated using Eq. (2.6). This gust was assumed to be in the downward vertical direction because it provides the most direct effect to increase wing bending for the assumptions made when generating the B_g matrix.

The continuous gust disturbance was implemented using the "Dryden Wind Turbulence Model" (Discrete, $-q$, $+r$) block in Simulink [49]. The block parameters were set with a 6-m wind of 5 m/s, from the north. The probability of exceedance of high-altitude intensity was "10^{-2} - Light" and the scale length was 762 meters, which is a standard value of 2,500 feet [2]. The wingspan was set to 6 meters and the sample time was 0.001 seconds. With these parameters, the Simulink block uses the current aircraft altitude, velocity, and direction cosines matrix based on the current attitude to generate longitudinal, lateral, and vertical velocity components of turbulence. These components were used as the inputs to the static B_g from Eq. (2.1) matrix which was defined at the equilibrium condition.

Test case 1 with discrete gust uses the full preview method discussed in Section 3.1.2, while the other test cases use the receding horizon approach discussed in Section 3.2.2. For the receding horizon approach, the preview horizon T_p was set to three seconds and implementation interval T_i was set to 0.1 seconds. The discrete-time linear models used a time step of 0.001 seconds. The QP problems in Eqs. (3.20) and (3.29) are solved using the "lsqlin" function in MATLAB, using the active-set algorithm.

The results for test case 1 are shown in Figs. 4.9 and 4.10. Figure 4.9 shows the pitch rate response and the out-of-plane bending curvatures at the critical stations while encountering the discrete gust. The yellow line shows the aircraft response without any flight controller. The X-HALE shows a stabilizing response, but note

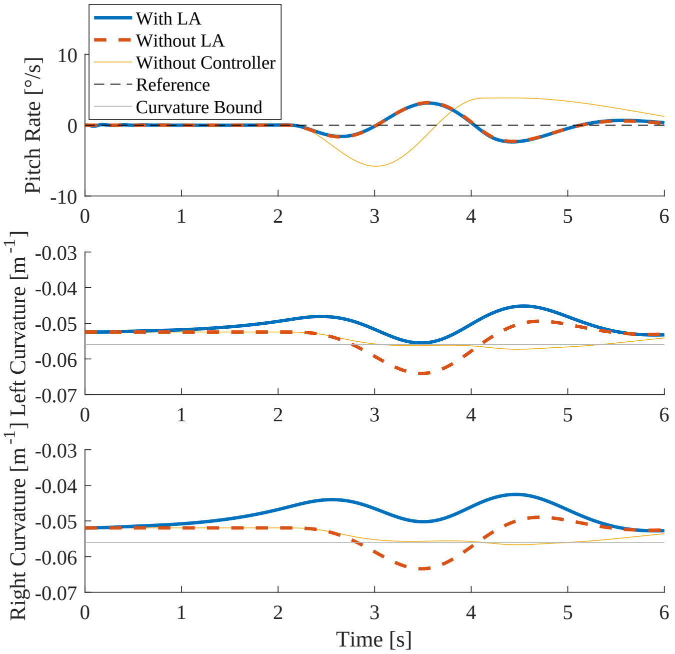

Figure 4.9: Responses of pitch rate and wing root bending curvature for test case 1: discrete downward gust with and without LA

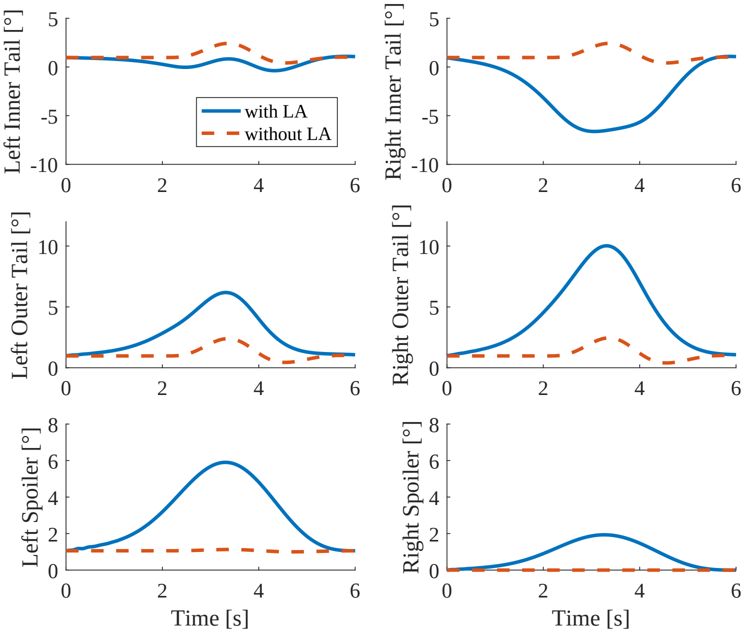

Figure 4.10: Time histories of tail and roll spoiler inputs for test case 1: discrete downward gust with and without LA

that the structural loads (bending curvature) are not very high. Keep in mind that higher negative values indicate increased upward curvature. The aircraft response with the nominal controller engaged (red dashed line) shows a much faster return to the trim point, but results in higher loads. This shows that gust disturbances may not necessarily be the cause of excessive structural loads, but rather it is due to the flight controller or operator responding to the disturbance.

The aircraft response with the LA system activated is shown by the solid blue line. This test case has a flexible output correction factor of $y_{f,\text{correction}} = 66.6\%$. The bending curvature dynamics are restricted within bounds by the LA system:

$$\begin{aligned} \kappa_{L1,\text{integrity}} &= 4.02\%, \\ \kappa_{R1,\text{integrity}} &= 26.7\%. \end{aligned} \tag{4.17}$$

The mean absolute errors of the rigid body outputs are all less than 0.05°/s, indicating that the trajectory tracking performance is minimally affected by the LA system and the decoupled design of the null space filter is effective:

$$\begin{aligned} e_p &= 0.011^\circ/\text{s}, \\ e_q &= 0.042^\circ/\text{s}, \\ e_r &= 0.009^\circ/\text{s}. \end{aligned} \tag{4.18}$$

The time histories of the tail and roll spoiler inputs for test case 1 are shown in Fig. 4.10. The incremental changes to the thruster inputs were less than one percent of the normalized throttle signal and, therefore, are not shown. To alleviate the load, the roll spoilers are engaged symmetrically to reduce the lift at the wing tips, while they were not used at all for the response without LA. The left and right outer tails increase the deflections which caused the high bending curvature without LA, which shows that more lifting load is being supported at the outer pods (at two-thirds of the length of the wing). The left and right inner tails deflect opposite of the response

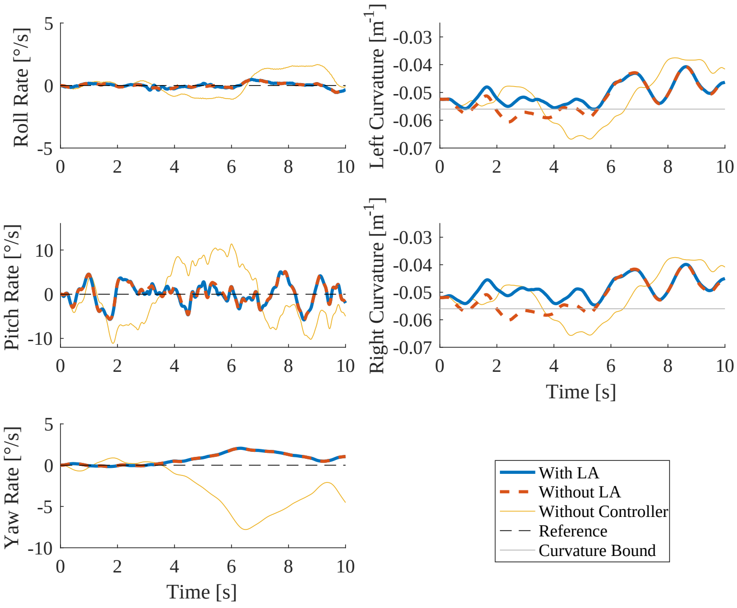

Figure 4.11: Responses of rigid body motion and wing root bending curvature for test case 2: turbulence with and without LA

from the nominal controller, showing less load being supported at the inner pods (at one-third of the length of the wing). This result seems to contradict the conclusions presented by [18], which showed efficient deflections were down for inboard control surfaces and up for outboard control surfaces. However, note that the analysis in the literature was for conventional transport aircraft, where the majority of the mass is in the fuselage, attached to the roots of the wings. The X-HALE mass is distributed along its wingspan, therefore, a different result is understandable and insightful for this type of aircraft.

One can see that the control surfaces begin deflecting to reduce the bending curvature at around one second into the simulation. This is one second before the gust is encountered and around 1.75 seconds before the curvature bounds are exceeded without LA. This shows that the proposed method manipulates the structures in anticipation of a future load exceedance, due to the preview horizon and a priori knowledge of the gust and controller response.

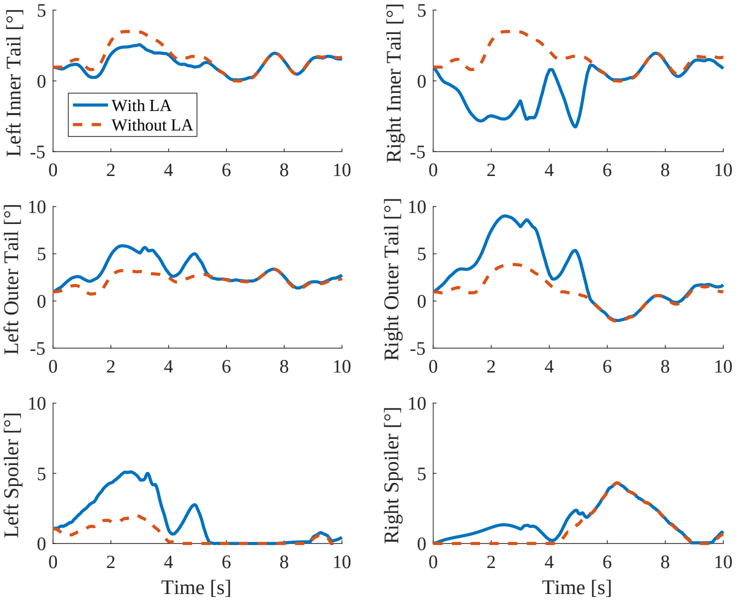

Figure 4.12: Time histories of tail and roll spoiler inputs for test case 2: turbulence with and without LA

The rigid body response and the bending curvatures at the critical stations while encountering turbulence in level flight for test case 2 are shown in Fig. 4.11. The response with the nominal controller disengaged, is again presented by the yellow line, which results in higher curvature values, than the discrete gust. In this case, the nominal controller reduces the maximum bending curvature during the simulation, but still results in curvatures in excess of the bounds.

The aircraft response with the LA system activated is shown by the solid blue line. This test case has a flexible output correction factor of $y_{f,\text{correction}} = 53.3\%$. The bending curvature dynamics are restricted within bounds by the LA system:

$$\begin{aligned} \kappa_{L1,\text{integrity}} &= 0.01\%, \\ \kappa_{R1,\text{integrity}} &= 15.4\%. \end{aligned} \tag{4.19}$$

The mean absolute errors of the rigid body outputs are all less than 0.2°/s, indicating that the trajectory tracking performance is minimally affected by the LA

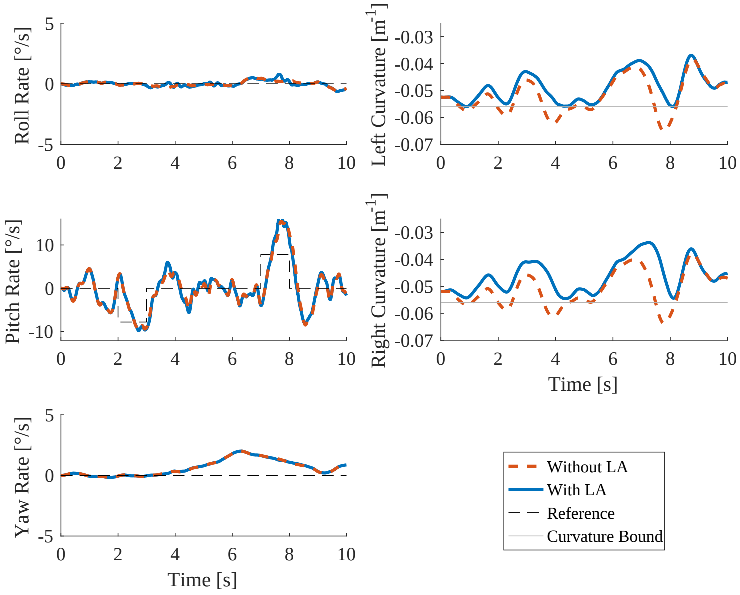

Figure 4.13: Responses of rigid body motion and wing root bending curvature for test case 3: descent in turbulence with and without LA

system and the decoupled design of the null space filter is effective:

$$\begin{aligned} e_p &= 0.030°/\text{s}, \\ e_q &= 0.186°/\text{s}, \\ e_r &= 0.007°/\text{s}. \end{aligned} \tag{4.20}$$

The time histories of the tail and roll spoiler inputs are shown in Fig. 4.12. Note that the control surfaces are engaged before the prolonged bending curvature exceedance which begins at two seconds into the simulation in order to keep the gust and controller response within the bounds. One can also see that the null space variable is not used for the last few seconds of the simulation since there is no exceedance of bounds to correct.

The rigid body response and the bending curvatures at the critical stations while descending in turbulence in test case 3 are shown in Fig. 4.13. The command to pitch down alleviates some of the excess loads that were observed at this point in

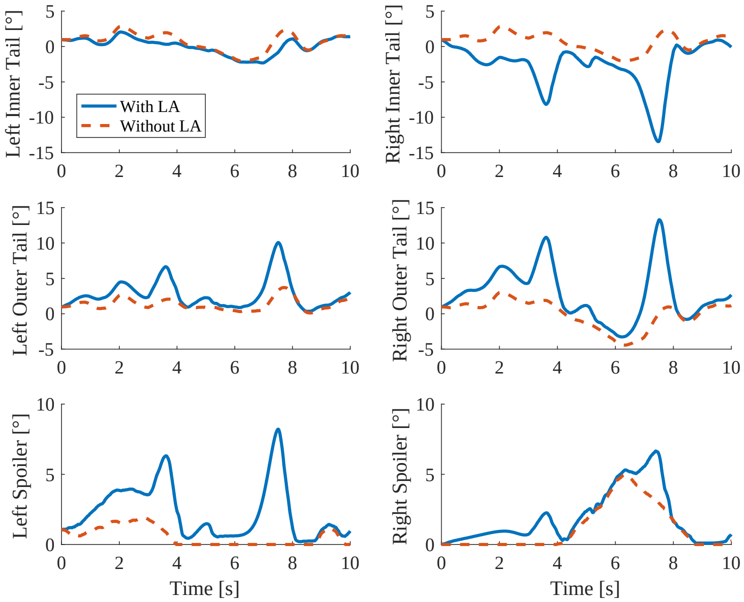

Figure 4.14: Time histories of tail and roll spoiler inputs for test case 3: descent in turbulence with and without LA

the simulation during case 2. However, the command to pitch up when stopping the descent results in a large and abrupt violation of the curvature bounds just before eight seconds into the simulation.

This test case has a flexible output correction factor of $y_{f,\text{correction}} = 69.0\%$. The bending curvature dynamics are restricted within bounds by the LA system:

$$\begin{aligned} \kappa_{L1,\text{integrity}} &= 0.11\%, \\ \kappa_{R1,\text{integrity}} &= 5.75\%. \end{aligned} \tag{4.21}$$

The mean absolute errors of the rigid body outputs are all less than 0.2°/s, indicating that the trajectory tracking performance is minimally affected by the LA system and the decoupled design of the null space filter is effective:

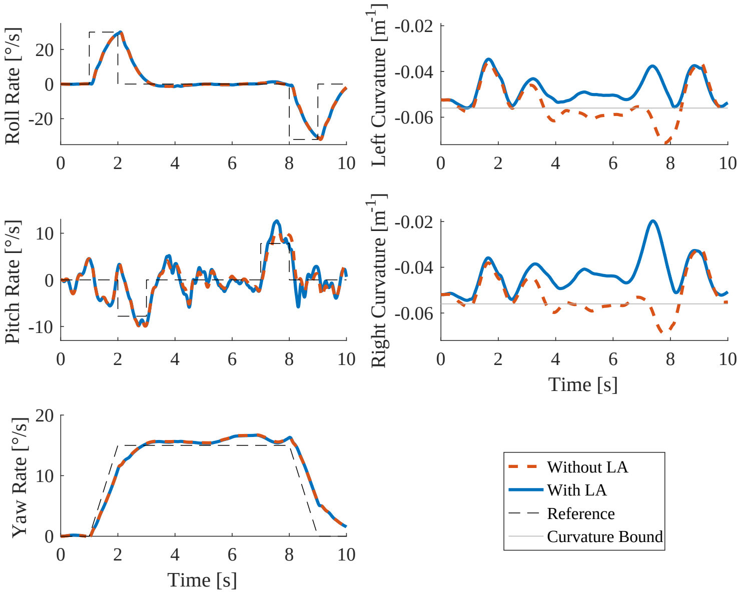

Figure 4.15: Responses of rigid body motion and wing root bending curvature for test case 4: descending turn in turbulence with and without LA

$$\begin{aligned} e_p &= 0.011°/\text{s}, \\ e_q &= 0.197°/\text{s}, \\ e_r &= 0.004°/\text{s}. \end{aligned} \tag{4.22}$$

Again, the trajectory tracking performance is not affected by LA method and the bending curvatures are kept within the bounds by using the proposed LA system. The time histories of the tail and roll spoiler inputs are shown in Fig. 4.14. The anticipatory nature of the LA system is observed again, as well as times in the middle and very end of the simulation, where the LA system is not engaged.

The rigid body response and the bending curvatures at the critical stations while executing a descending turn in turbulence in test case 4 are shown in Fig. 4.15. The combination of the multi-axis maneuver and turbulence results in a prolonged exceedance of the bending curvature for over four seconds. The highest curvature occurs suddenly, just before the eight-second mark, as the aircraft pitches back up to

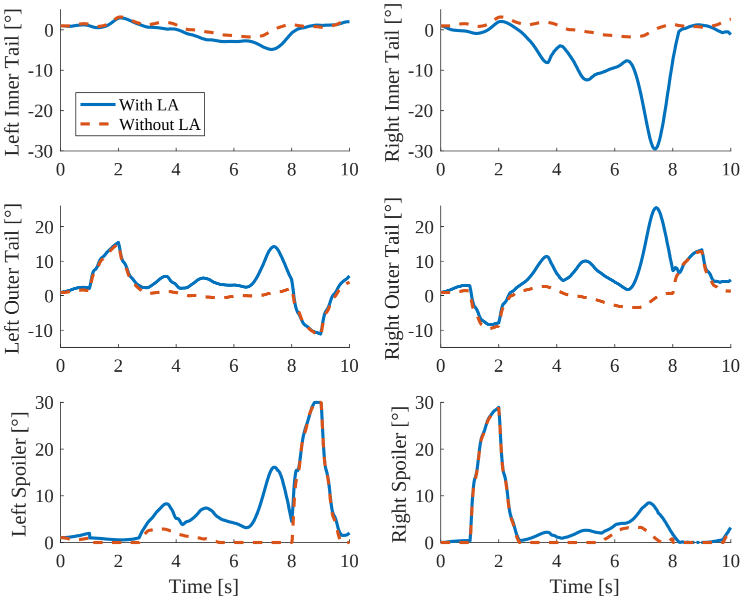

Figure 4.16: Time histories of tail and roll spoiler inputs for test case 4: descending turn in turbulence with and without LA

level flight while still turning. The amplitude and rate of this exceedance provided a good test case of the performance limits of the LA system. In one simulation run, a shorter preview horizon T_p of two seconds was used for this test case, but the solver for Eq. (3.29) could not find a feasible solution at this point in the simulation. This was corrected by increasing T_p to three seconds, which allowed for adequate anticipatory control input to manipulate the structure in such a way that the pitch up maneuver and turbulence did not exceed the bending curvature bounds. Around this time in the simulation, some high-frequency differences in the pitch response are observed as well, which shows a limitation of the null space filter for large values of the null space variable.

This test case has a flexible output correction factor of $y_{f,\text{correction}} = 78.9\%$. The bending curvature dynamics are restricted within bounds by the LA system:

$$
\begin{aligned}
\kappa_{L1,\text{integrity}} &= 0.30\%, \\
\kappa_{R1,\text{integrity}} &= 3.70\%.
\end{aligned}
\tag{4.23}
$$

The mean absolute errors of the rigid body outputs are all less than 0.25°/s, indicating that the trajectory tracking performance is minimally affected by the LA system and the decoupled design of the null space filter is effective:

$$
\begin{aligned}
e_p &= 0.057^\circ/\text{s}, \\
e_q &= 0.216^\circ/\text{s}, \\
e_r &= 0.033^\circ/\text{s}.
\end{aligned}
\tag{4.24}
$$

The time histories of the tail and roll spoiler inputs are shown in Fig. 4.16. This test case resulted in the highest use of the control surfaces, both for the trajectory tracking and for the load alleviation.

4.6 Numerical Investigation of Applying Invariant Null Space Filter to Parameter-Varying System

The LA system with an invariant null space filter is applied to an LPV model of the X-HALE in order to verify the approach described in Section 3.3.1. The LPV model is built by generating six linearized models using UM/NAST at incremental airspeeds, from 13 m/s to 18 m/s, at a constant altitude of 30 meters, with their associated values for dynamic pressure. These models are then combined in MATLAB (ver. r2020a [58]) as a model array with a single parameter variation with the vector of corresponding dynamic pressure values as the sampling grid. The various state values and input values for each equilibrium are also compiled into arrays for use with the model array. These arrays are engaged using the *LPV System* block in

Simulink. For this demonstration, the null space filter is invariant and is generated based on the equilibrium point conditions and linearized model at the beginning of the simulation. The system is connected together in Simulink to run the numerical simulation (including the nominal controller, reference signal source, null space filter, and null space variable signal source).

The LA system is demonstrated using the receding horizon method described in Section 3.2.2. A simulation is run with an assumed null space variable signal, $v_a(t)$, for the duration of one preview horizon, T_p. The flexible output response, $y_f(t)$, from that simulation is used for the QP problem to find the necessary change in null space variable signal, $\Delta v(t)$, to control the flexible output response within the constraints. The first implementation interval, T_i, of the solution, $v(t) = v_a(t) + \Delta v(t)$, is utilized and the remaining solution becomes the $v_a(t)$ for the next iteration. This routine continues, iteratively, until the solution is built for the entire maneuver.

The maneuver used for this demonstration is an altitude descent. The reference trajectory consists of a pitch down two seconds after the simulation starts with a pulse of $-4°/\text{s}$, intended to achieve $-2.2°$ of pitch in one second (equilibrium condition pitch attitude is $+1.8°$). The nose-down pitch attitude is held for four seconds before leveling off in one additional second. The reason for this maneuver is to have the constraint violation occur at a higher airspeed than the start of the simulation, thus creating an intentional mismatch between the LPV model of the aircraft and the invariant null space filter. The state results for this demonstration both with and without LA are shown in Fig. 4.17. The rigid body outputs of roll-, pitch-, and yaw-rates are on the left. The velocity is on the bottom right and the flexible outputs for each wing are on the upper right. The time histories of the tail and roll spoiler inputs are shown in Fig. 4.18.

This test case has a flexible output correction factor of $y_{f,\text{correction}} = 49.3\%$. The plot for the bending curvature shows that the constraint is satisfied throughout the maneuver, despite the mismatch between the LPV model of the aircraft, which is made possible because the LA system is getting updated state data every implementation interval to update the solution of $v(t)$. This was not the case for the results presented in Fig. 3.3. The bending curvature dynamics are restricted within bounds by the LA system:

$$\begin{aligned} \kappa_{L1,\text{integrity}} &= 4.40\%, \\ \kappa_{R1,\text{integrity}} &= 8.43\%. \end{aligned} \tag{4.25}$$

However, some high-frequency signals are also generated in the process, causing roll oscillations that then influence the other axes. It is possible that these roll oscillations are a consequence of the mismatch between the invariant null space filter (which design was based on the aircraft model linearized about a 14 m/s velocity) and the LPV aircraft model flying at a higher airspeed. Therefore, designing a corresponding null space filter for each aircraft model linearization and arranging them as an LPV system may improve performance. Despite the oscillations, the mean absolute errors of the rigid body outputs are still less than 0.1°/s, indicating that the trajectory tracking performance is minimally affected by the LA system and the decoupled design of the null space filter is effective:

$$\begin{aligned} e_p &= 0.023^\circ/\text{s}, \\ e_q &= 0.060^\circ/\text{s}, \\ e_r &= 0.003^\circ/\text{s}. \end{aligned} \tag{4.26}$$

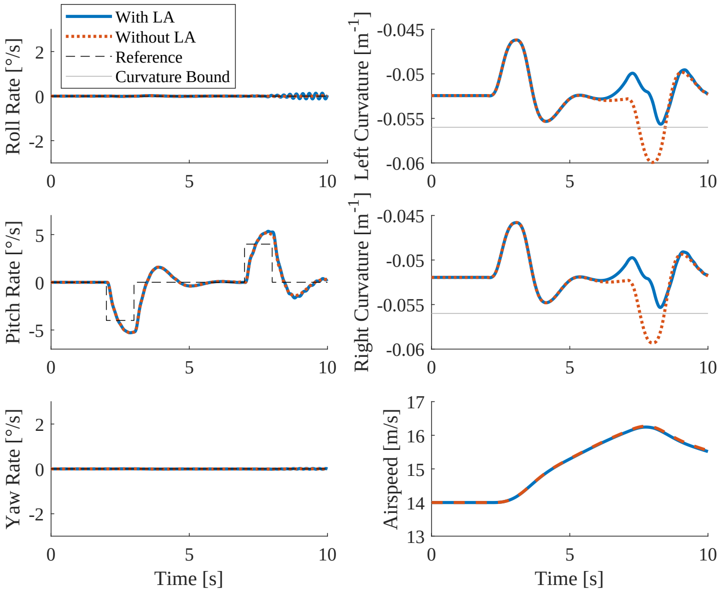

Figure 4.17: Responses of rigid body motion and wing root bending curvature for descent for an invariant null space filter applied to an LPV system, with and without LA

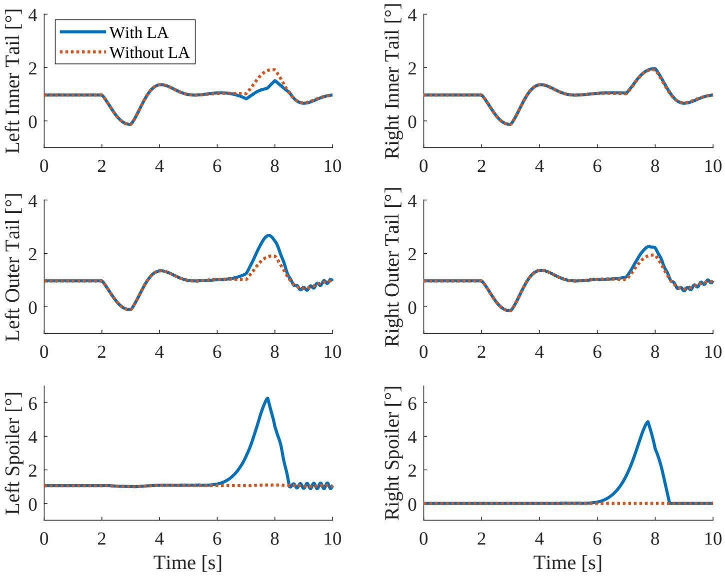

Figure 4.18: Time histories of tail and roll spoiler inputs for descent for an invariant null space filter applied to an LPV system, with and without LA

4.7 Numerical Investigation of Parameter-Varying Load Alleviation System

The solutions to the issues arising when using an LPV null space filter are applied in a numerical investigation in order to verify the approach described in Section 3.3.2. The LPV null space filter is built by generating six filters based on the linearized models of the X-HALE, with their associated values for dynamic pressure. These models are then combined in MATLAB (ver. r2020a [58]) as a model array, as was done for the X-HALE LPV system. The various state values and input values for each equilibrium are also compiled into arrays for use with the model array. These arrays are engaged using the *LPV System* block in Simulink. The option for the scheduling of this LPV system, in the settings in Simulink, is set to transition between models discretely, by going to the *nearest* model, rather than to linearly interpolate between models. The normalization of the null space filter output signals, described in Section 3.3.2.1, resulted in excessive spillover in the rigid body output, and therefore was not implemented for these results. The implementation of the LA solution is shifted in this demonstration, from maintaining continuity by the state of the null space filter to maintaining continuity of the $\Delta u(t)$ signal between iterations, as described in Section 3.3.2.2. The system is connected together in Simulink to run the numerical simulation (including the nominal controller, reference signal source, null space filter, and null space variable signal source).

The maneuver used for this demonstration is the same altitude descent used throughout this Chapter. The state results for this demonstration both with and without LA are shown in Fig. 4.19. The time histories of the tail and roll spoiler inputs are shown in Fig. 4.20.

This test case has a flexible output correction factor of $y_{f,\text{correction}} = 49.3\%$. The plot for the bending curvature shows that the constraint is violated slightly during the maneuver but there are no jumps during transitions from one model to the next. The bending curvature dynamics are restricted within bounds by the LA system:

$$
\begin{aligned}
\kappa_{L1,\text{integrity}} &= -0.19\%, \\
\kappa_{R1,\text{integrity}} &= 0.44\%.
\end{aligned}
\tag{4.27}
$$

However, high-frequency signals are still generated in the process, causing roll oscillations that then influence the other axes. The oscillations in this case have a higher amplitude than the oscillations seen when using an invariant null space filter, as shown in Fig. 4.17. Despite the oscillations, the mean absolute errors of the rigid body outputs are still less than 0.2°/s, indicating that the trajectory tracking performance is minimally affected by the LA system and the decoupled design of the null space filter is effective:

$$
\begin{aligned}
e_p &= 0.115^\circ/\text{s}, \\
e_q &= 0.138^\circ/\text{s}, \\
e_r &= 0.015^\circ/\text{s}.
\end{aligned}
\tag{4.28}
$$

Note, though, that there were many iterations while producing these results where the QP problem did not converge on a solution before reaching the maximum 10,000 iterations. This non-convergence may also explain why the solution includes negative deflections for the right roll spoiler, which should have been limited to positive deflections by the constraints in the QP problem. This was not the case when applying the invariant null space filter, where all iterations successfully converged to a solution.

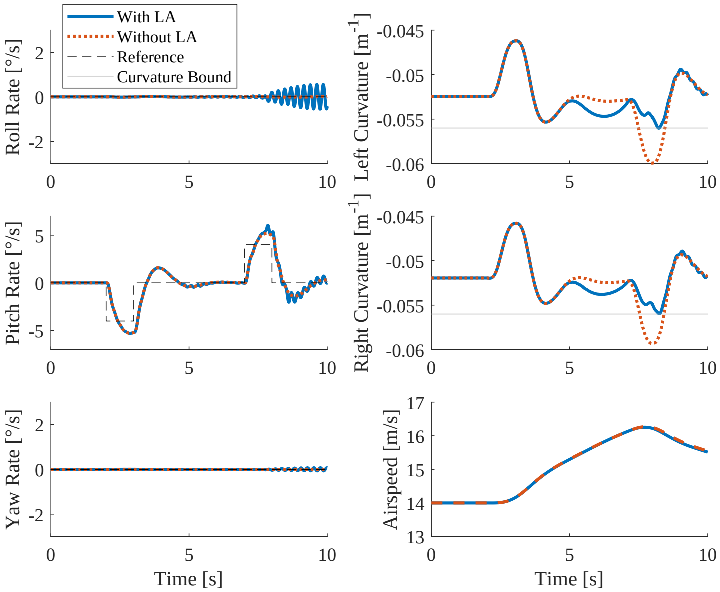

Figure 4.19: Responses of rigid body motion and wing root bending curvature for descent for an LPV null space filter applied to an LPV system, with and without LA

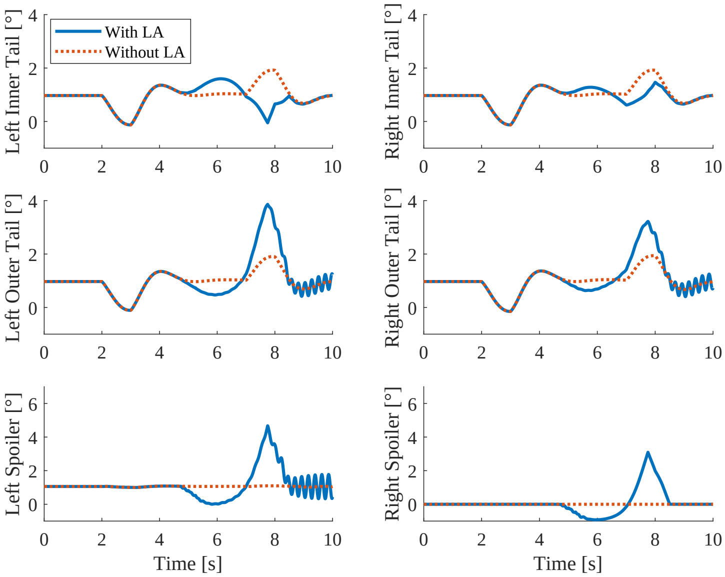

Figure 4.20: Time histories of tail and roll spoiler inputs for descent for an LPV null space filter applied to an LPV system, with and without LA

4.8 Numerical Investigation of Load Alleviation System on Nonlinear X-HALE Model

The LA system, with an invariant null space filter and configured in the MPC format, is applied to a nonlinear model of the X-HALE in order to verify the approach described in Section 3.4. The nonlinear model is built using UM/NAST and the required input settings for level flight are determined and applied for a dynamic simulation with a time discretization of 0.01 seconds. A virtual Inertial Navigation System (INS) is positioned at the center of the model and used for feedback control. The controller is written in a MATLAB script (ver. r2020a [58]), based on the P/PI architecture described in Section 4.1.2. The controller script obtains the reference command signal from a lookup table. This controller script also calls the CA function, which utilizes MPC to find the appropriate $\Delta u(t)$ value for each time step. The CA function is configured to retain the $\Delta u(t)$ solution each iteration in order to maintain continuity. The CA function is also configured to give priority to an exponential decay of the $\Delta u(t)$ signal (see Section 3.4.2) over the previous $\Delta u(t)$ solution if it will not adversely affect the flexible output to cause a constraint violation. For this demonstration, the null space filter is invariant and is generated based on the equilibrium point conditions and linearized model at the beginning of the simulation. The preview horizon, T_p, is set at three seconds.

The maneuver used for this demonstration is an altitude descent, just as was used to demonstrate the LA system for and LPV aircraft model. The reference trajectory consists of a pitch down two seconds after the simulation starts with a pulse of -4°/s. The nose-down pitch attitude is held for four seconds before leveling off in one additional second. The state results for this demonstration both with and without LA are shown in Fig. 4.21. The time histories of the tail and roll spoiler inputs are shown in Fig. 4.22.

This test case has a flexible output correction factor of $y_{f,\text{correction}} = 26.3\%$. The plot for the bending curvature shows that the constraint is satisfied with a large margin, which is likely caused by an overestimation of flexible output response on the part of the linear model used for prediction:

$$\begin{aligned} \kappa_{L1,\text{integrity}} &= 51.1\%, \\ \kappa_{R1,\text{integrity}} &= 52.4\%. \end{aligned} \tag{4.29}$$

However, some high-frequency signals are also generated in the process, causing pitch oscillations that then influence the other axes. It is possible that these pitch oscillations are a consequence of some spill-over effect between the null space variable and the rigid body output. Due to the oscillations, the mean absolute errors of the rigid body outputs have a higher value that may be undesirable:

$$\begin{aligned} e_p &= 0.167^\circ/\text{s}, \\ e_q &= 0.916^\circ/\text{s}, \\ e_r &= 0.032^\circ/\text{s}. \end{aligned} \tag{4.30}$$

4.9 Numerical Investigation of Load Alleviation System with Nonlinear GTA Model

The LA system is also applied to a nonlinear model of the GTA in order to demonstrate the effectiveness of the system described in Section 3.4. The GTA model contains dynamics which are more representative of typically-designed aircraft, with a fuselage, wings, and tail. This model also provides a much larger flight envelope that the X-HALE. The system was simulated using the dynamic solver module of UM/NAST. The test cases for this demonstration are modeled after one previously used for the X-HALE numerical demonstrations.

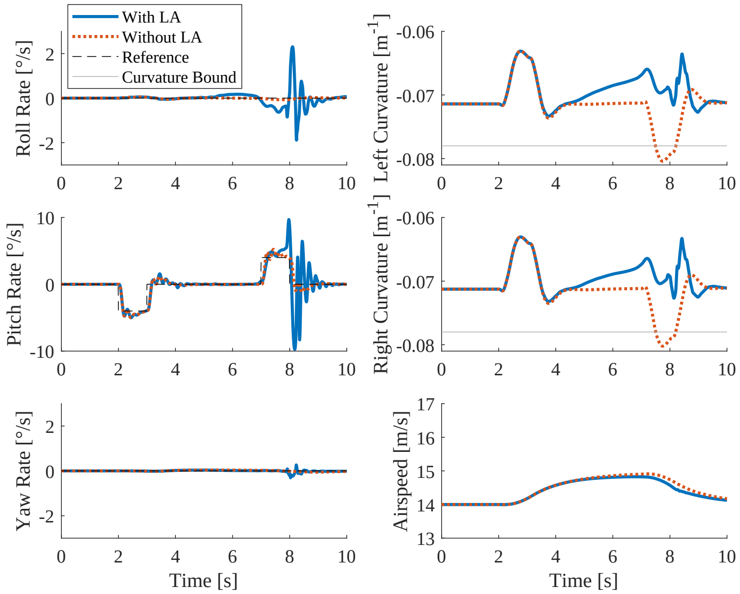

Figure 4.21: Responses of rigid body motion and wing root bending curvature for descent for an invariant null space filter applied to a nonlinear X-HALE model, with and without LA

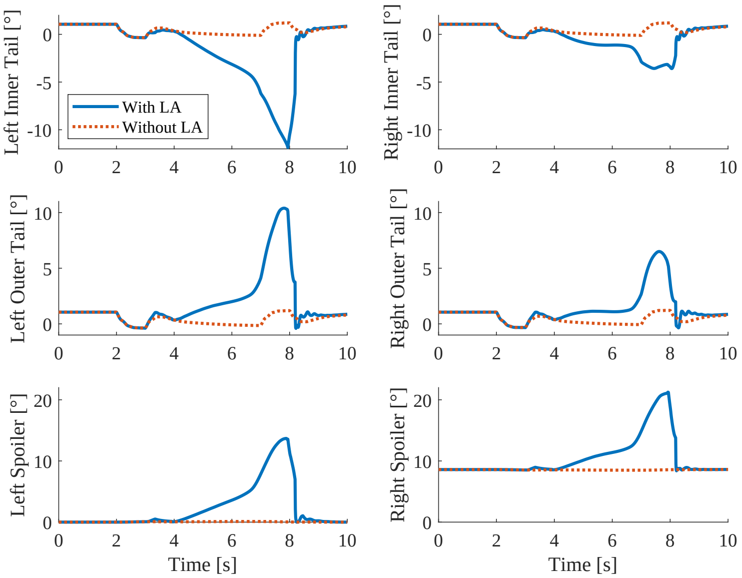

Figure 4.22: Time histories of tail and roll spoiler inputs for descent for an invariant null space filter applied to a nonlinear X-HALE model, with and without LA

1. Descent: In order to descend to a lower altitude, the reference trajectory consists of a pitch down two seconds after the simulation starts with a pulse of $-6°/\mathrm{s}$ over one second. The nose-down pitch attitude is held for four seconds before leveling off in one additional second. This maneuver results in a descent of 80 meters.

2. Descent with discrete gust encounter: While leveling off during the descent maneuver described above, the aircraft encounters a discrete upward gust with a 1−cosine profile. The gust is encountered eight seconds after the simulation starts, swelling to a peak gust amplitude of $U_0 = 10.8$ m/s and then decaying to zero over 1.03 seconds (i.e., $t_{\text{gust}} = 1.03$ s). The parameters for this gust are based on the airworthiness specifications for critical gust loads described in described in Title 14 of the CFR, section 25.341 [47].

The nonlinear model is built using UM/NAST and the required input settings for level flight are determined and applied for a dynamic simulation with a time discretization of 0.01 seconds. A virtual INS is positioned at the center of the model and used for feedback control. The controller is written in a MATLAB script (ver. r2020a [58]), based on the PI control architecture described in Section 4.1.4. The controller script obtains the reference command signal from a lookup table. This controller script also calls the CA function, which utilizes MPC (with $T_p = 3$s) to find the appropriate $\Delta u(t)$ value for each time step. The CA function is configured to retain the $\Delta u(t)$ solution each iteration in order to maintain continuity. The disengagement mechanism in this case is the addition of an exponential decay of the $\Delta u(t)$ signal at the end of the last solution from the QP solver, as described in Section 3.4.2. For this demonstration, the null space filter is invariant and is generated based on the equilibrium point conditions and linearized model at the beginning of the simulation. The bound on the wing bending curvature is set to -0.235m^{-1} for both cases. This value represents a flexible output correction factor of $y_{f,\text{correction}} = 11.1\%$, according to Eq. (4.10).

The state results for test case 1, both with and without LA, are shown in Fig. 4.23. The rigid body outputs of roll-, pitch-, and yaw-rates are on the left. The aircraft load factor is on the bottom right and the flexible outputs for each wing are on the upper right. The time histories of the elevator, aileron, and flap inputs are shown in Fig. 4.24. The solution had only an inconsequential effect on the nominal control signal for the rudder and thrusters, therefore, they are not displayed.

The plot for the bending curvature shows that the constraint is satisfied with a reasonable margin, which represents an attenuation of over 20% of the bending, compared to the results without LA:

$$\begin{aligned} \kappa_{L,\text{integrity}} &= 12.9\%, \\ \kappa_{R,\text{integrity}} &= 10.5\%. \end{aligned} \tag{4.31}$$

There is some extraneous motion in the roll axis, but it is very low. Overall, the results are very desirable:

$$\begin{aligned} e_p &= 0.060^\circ/\text{s}, \\ e_q &= 0.040^\circ/\text{s}, \\ e_r &= 0.006^\circ/\text{s}. \end{aligned} \tag{4.32}$$

The resultant $\Delta u(t)$ can be approximated by noting the difference between the plots in Fig. 4.24. When the $\Delta u(t)$ signal is active, the elevators deflect less, which would provide less pitch rate. Both ailerons deflect upward, which would reduce the lift near the wingtips, and the flaps deflect downward, increasing the lift near the fuselage. This matches the conclusions found in the literature for centrally-loaded aircraft [18]. One interesting result is the difference in load factor with the LA system active. The measured load factor comes from the INS sensor placed at the center of the wing box. The difference is small, but the value of the load factor is higher when

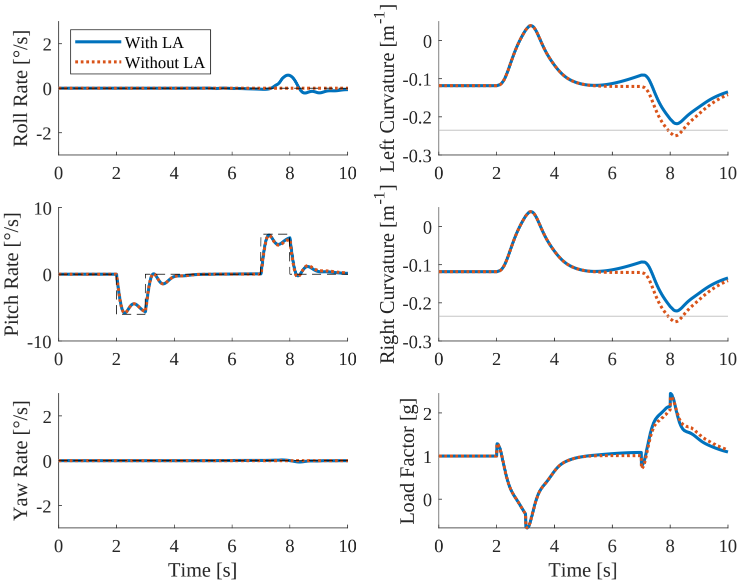

Figure 4.23: Responses of rigid body motion and wing root bending curvature for descent for an invariant null space filter applied to a nonlinear GTA model, with and without LA

the LA system is active, even while the wing bending curvature is being reduced. One way to understand this phenomenon is to first note that the pitch rate motion is approximately the same for both cases, meaning that the lifting force is staying the same. With that in mind, if the wings are not bent as much, then it means that the amount of force that would normally be absorbed by the wings flexing is instead being redirected to the fuselage, thus increasing the load factor measured there by the INS.

The state results for test case 2, both with and without LA, are shown in Fig. 4.25. The time histories of the elevator, aileron, and flap inputs are shown in Fig. 4.26. The flexible state constraint was equal to the case without gust, which now represents a flexible output correction factor of $y_{f,\text{correction}} = 36.8\%$ of the bending, compared to the results without LA.

The plot for the bending curvature shows that the constraint is satisfied with plenty margin. The resultant bending trajectory satisfied the constraints by an extra

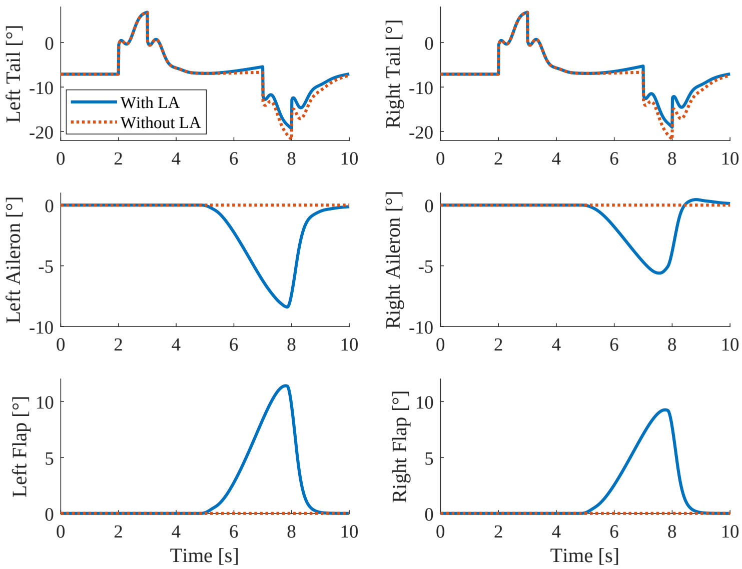

Figure 4.24: Time histories of elevator, aileron, and flap inputs for descent for an invariant null space filter applied to a nonlinear GTA model, with and without LA

21%, showing an overall attenuation of 58%, compared to the results without LA:

$$\begin{aligned} \kappa_{L,\text{integrity}} &= 28.1\%, \\ \kappa_{R,\text{integrity}} &= 21.3\%. \end{aligned} \tag{4.33}$$

The LA objective is achieved, but the response is excessive, showing some areas for future improvement of the system. There is some extraneous motion in the roll and pitch axes, but it is still less than 0.2°/s:

$$\begin{aligned} e_p &= 0.156°/\text{s}, \\ e_q &= 0.153°/\text{s}, \\ e_r &= 0.023°/\text{s}. \end{aligned} \tag{4.34}$$

The resultant $\Delta u(t)$ can be approximated by noting the difference between the plots in Fig. 4.26. Compared to the observations for test case 1, the elevators deflect less, both ailerons deflect upward, and the flaps deflect downward, to reduce the out-of-plane wing bending. The relative increase in load factor is observed again.

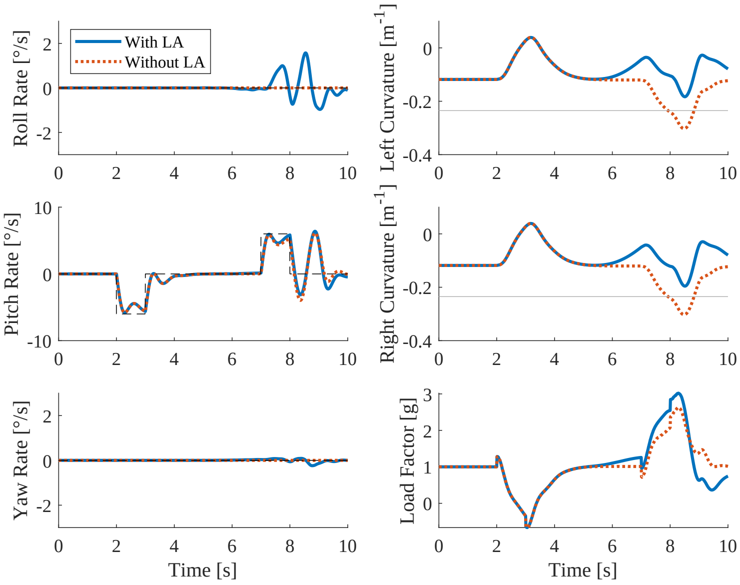

Figure 4.25: Responses of rigid body motion and wing root bending curvature for descent with discrete gust for an invariant null space filter applied to a nonlinear GTA model, with and without LA

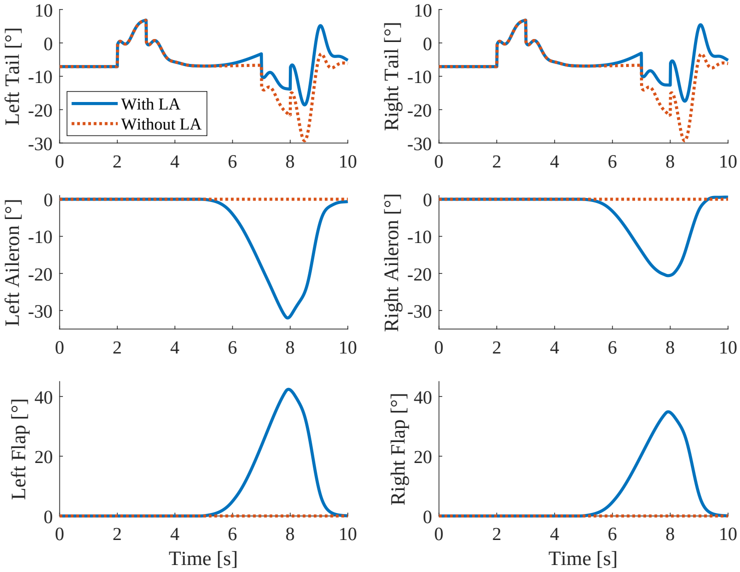

Figure 4.26: Time histories of elevator, aileron, and flap inputs for descent with discrete gust for an invariant null space filter applied to a nonlinear GTA model, with and without LA

CHAPTER 5

Characterization of Load Alleviation System Applied to Nonlinear Systems

After developing the methods for the LA system, it is important to understand its limitations with respect to effectiveness when applied to a physical system. Therefore, the following case study was designed to characterize the system, which is based on linear systems theory and models, and determine its limits of applicability when implemented on a nonlinear system. A collection of variants of the GTA model are used to study the effect of aircraft flexibility level, preview horizon length, and load alleviation level on the performance of the LA system.

5.1 System Under Evaluation

The final configuration of the LA system using CA for a nonlinear aircraft model is described in Section 3.5. It consists of a CA function using MPC that is called by the nominal controller of the aircraft at every time step. The CA function uses an assumed $\Delta u_a(t)$ trajectory for the given T_p and a preview of $r(t)$ and $g(t)$ in a linear simulation to predict the flexible output trajectory $y_f(t)$ for the preview horizon. If the prediction shows that $y_f(t)$ will exceed the constraints, then the optimization function is triggered in order to find $\Delta u(t)$ that constrains $y_f(t)$. Otherwise, $\Delta u_a(t)$ is sufficient and is returned as $\Delta u(t)$. This process repeats every time step.

The value of the preview horizon, T_p, is identified as a parameter of the LA system which may affect its performance. Therefore, four different time durations will be used in each application of the system: three, two, one, and one-half second. All test methods below which use the preview horizon will be repeated for each of these four values.

5.2 Objectives

There are two objectives for this study.

1. Determine limits of applicability of linear-time-invariant null space filter coupled with nonlinear system
2. Evaluate limits of applicability of linear-based system for load alleviation through control allocation when applied to a nonlinear system

5.3 Objective Nonlinear System

The nonlinear system chosen for this study is the GTA model, which is described in Section 4.1.3. Five variants of the GTA are used in order to evaluate the impact of wing stiffness on the LA system. The stiffness values of the wings are reduced for out-of-plane bending, in-plane bending, and torsion. The extensional stiffness values are unchanged and all other components of the model are treated as rigid elements in the UM/NAST framework (see Appendix C for details). With this relaxed stiffness of the wings, at an equilibrium flight condition of 160 m/s at 20,000 ft, each variant of the GTA will have unique characteristics for static vertical wingtip deflection (δz_{wt}), the first out-of-plane bending frequency (f_{oopb}), the short period frequency (f_{sp}), and static wing bending curvature (κ_{static}). The notable characteristics for each variant at this flight condition are presented in Table 5.1. Note that wingtip deflection is

Table 5.1: Notable characteristics for each GTA variant at flight condition of 160 m/s at 20,000 ft

Model No.	δz_{wt} (%)	f_{oopb} (Hz)	f_{sp} (Hz)	κ_{static} (1/m)
1	11.5	1.81	0.893	-0.067
2	20.0	1.37	0.862	-0.118
3	28.5	1.15	0.833	-0.171
4	34.0	1.05	0.820	-0.206
5	39.2	0.977	0.813	-0.242

presented as a percentage of aircraft half-span. All variants use the same nominal controller which uses PI control to minimize the error between the measured roll-, pitch-, and yaw-rates and the corresponding reference commanded angular rates, as described in Section 4.1.4. All test methods below will be repeated for each of these variants.

5.4 Evaluation Method

The objectives of this study are accomplished by collecting and analyzing specific Measures of Performance (MOPs), which measure system-specific characteristics connected to a requirement. Each one of the MOPs aids in characterizing the system as a whole, and provides the necessary data for accurate conclusions and recommendations from the study.

5.4.1 Objective 1: Determine limits of applicability of linear-time-invariant null space filter coupled with nonlinear system

5.4.1.1 MOP 1.1: Spill-over frequency

The null space filter is designed to exploit the null space that exists between the control effectors and the rigid body output of the aircraft, as explained in Section

3.1.1. However, since the null space filter is generated from a linearized model, about an equilibrium point of the nonlinear aircraft model, there will be some point at which the assumptions for linearization are no longer valid, thus affecting the rigid body output. The spill-over frequency of the null space filter is the frequency of the null space variable signal beyond which the rigid body output is adversely affected.

- Test Method

  The combined model of the aircraft with null space filter will be subjected to a 20-second chirp (or frequency sweep) signal at each condition listed in the test point matrix for this objective in Table 5.2. The chirp signal is commonly used for system identification applications and consists of a sinusoidal signal, for which the instantaneous frequency is increasing over the duration of the signal. A chirp signal with a linearly increasing frequency is designed using the following function:

  $$v(t) = \sin\left[2\pi\left(\frac{f_1 - f_0}{2T}t^2 + f_0 t\right)\right], \tag{5.1}$$

  where f_0 is the starting frequency of the signal, in Hz, f_1 is the final frequency of the signal, also in Hz, and T is the duration of the signal, in seconds [59]. The lower-limit of the starting frequency is dependent on the duration of the chirp signal, because it needs to be long enough to include one full period at the starting frequency (i.e., $f_0 \geq 1/T$). The upper-limit of the final frequency is dependent on the time discretization and Nyquist frequency principle. The final frequency can be no higher than one half of the sampling rate, or time discretization (i.e., $f_1 \leq 2/\Delta t$). The frequency values in Table 5.2 are listed in units of Hertz and also nondimensional frequencies, scaled by the first out-of-plane bending frequency, f_{oopb}, of the respective aircraft model (shown in Table 5.1). The test signal may be applied to each individual input channel of the null space variable, or to a combination of individual channels. Additional test methods include the use of a single-frequency sinusoidal signal to check the spill-over frequency candidate value. In all cases, the original sinusoidal signal for $v(t)$ must be processed through the null space filter to generate a $\Delta u(t)$ signal, which is then given as the input to the aircraft model for an open-loop dynamic simulation.

- Data Requirement

  A time history of the rigid body output of the aircraft model obtained from a numerical simulation of the $\Delta u(t)$ signal derived from the $v(t)$ chirp signal processed through the null space filter will be recorded in a data log.

- Exit Criteria

  One simulation run of the chirp signal including each input channel of each model number is needed to find an estimate of the spill-over frequency. Additional simulation runs using a narrower range of frequencies, or a single frequency, may be needed in order to identify a spill-over frequency with single-digit precision within a given order of magnitude. This will be done at each condition noted in the test point matrix in Table 5.2.

- Algorithm/Process

  The rigid body output data will be monitored to identify excursions or departures from the trim value throughout the time history data log. Any excursions of departures of the rigid body output will be noted and analyzed through a Fourier transform to identify the corresponding frequency. The most dominant frequency (highest power rating from the Fourier transform analysis) from the results of each channel of the rigid body output will first be identified as candidates for the spill-over frequency for a specific input channel. Then the highest power among those frequencies shows the principal response and corresponding

Table 5.2: Test Point Matrix for Objective 1

Test Point	Model No.	f_0 (Hz)	f_1 (Hz)	f_0/f_{oopb}	f_1/f_{oopb}
1.1	1	0.05	50	0.028	27.6
1.2	2	0.05	50	0.036	36.5
1.3	3	0.05	50	0.043	43.5
1.4	4	0.05	50	0.048	47.6

spill-over frequency for that input channel. In cases where two output channels have approximately equal power ratings, then the one with the lower frequency is determined to be the spill-over frequency for that input channel. When comparing the spill-over frequency for each input channel of a model number, the most common spill-over frequency is determined to be the spill-over frequency for the model number. For cases where two spill-over frequencies have the same number of dominant channels, then the lower frequency is determined to be the spill-over frequency for the model number.

- Evaluation Criteria

  None. Only determine the value of the spill-over frequency with single-digit precision within a given order of magnitude.

- Final Data Product

  The spill-over frequency for each model number will be listed in a table.

5.4.2 Objective 2: Evaluate limits of applicability of linear-based system for load alleviation through control allocation when applied to a nonlinear system

5.4.2.1 MOP 2.1: Constraint integrity of flexible output of aircraft model during maneuvering flight

The primary objective of the system under evaluation is to alleviate the loads borne by the aircraft structure during maneuvering flight and when encountering gust disturbances. These loads must be kept within constraints in order to maintain the integrity of the aircraft structure. The loads may be measured directly, or indirectly, by a structural output at key locations on the model of the aircraft.

- Test Method

  The objective model will perform a MVS maneuver in order to excite the out-of-plane bending deflection of the wing. The MVS is a commonly used test technique [60] to meet the minimum $2.5g$ load required for airworthiness certification, as detailed in Title 14 of the CFR, section 25.337 [47]. The maneuver begins with the aircraft flying at 1g and applying the following stick trajectory: (i) move the pilot stick with a sinusoidal shape until a load factor of $2.5g$ is reached, then (ii) reversing with a sinusoidal shape until a load factor of -0.5g is reached, then (iii) completing the sinusoidal shape to return to a load factor of 1g. For the case of the aircraft model used in this study, providing the nominal controller with a sinusoidal input for the pitch-rate reference signal yields the desired sinusoidal response in load factor. The period of the maneuver shall be six seconds, as this period allows each variant of the GTA to attain $2.5g$ ($\pm 0.1g$) without having significant saturation of the elevators. The maximum magnitude of the sinusoidal pitch-rate reference signal, $r_{q,\max}$ needed to achieve the $2.5g$ load factor for each model variant of the GTA is shown in Table 5.3, along

Table 5.3: The MVS design which results in a 2.5g load factor for each GTA variant at flight condition of 160 m/s at 20,000 ft

Model No.	$r_{q,\max}$ (°/s)	$\kappa_{\min}$ (1/m)	$\hat{n}_{z,\max}$ (g)
1	6.5	-0.174	2.53
2	8.5	-0.300	2.56
3	9.0	-0.382	2.55
4	9.3	-0.419	2.52
5	9.1	-0.443	2.43

with the minimum observed wing bending curvature, $\kappa_{\min}$, and the maximum load factor attained without the LA system, $\hat{n}_{z,\max}$. Note that because the flexible output for this case study is bending curvature, and that a more negative value of curvature denotes an increase in upward bend, the minimum value of the flexible output with the LA system provides the maximum displacement from the static value and, thus, the maximum upward bending of the wing.

The amount of correction needed by the LA system is identified as a significant parameter of this study. This parameter is quantified as the desired attenuation of the flexible output when performing the MVS maneuver without the LA system, expressed as a percentage of the maximum flexible output displacement from the static value prior to the maneuver, i.e.,:

$$y_{f,\text{correction}} = \frac{y_f^- - \hat{y}_{f\min}}{\hat{y}_{f\min} - y_{f\text{static}}}, \tag{5.2}$$

where $\hat{y}_{f\min}$ is the flexible output from the MVS without the LA system. This parameter can be used to define a threshold between a low correction (10% ±1%) and a high correction (30% ±1%). For a given GTA variant, the value of the flexible output constraint shall be set such that the test case falls within the desired correction value, as shown in Table 5.4.

- Data Requirement

A time history of the flexible output of the aircraft model obtained from a numerical simulation of the MVS maneuver will be recorded in a data log. The data log should start from at least three seconds prior to the initiation of the maneuver and include at least three seconds of data after the completion of the maneuver. The user-defined constraint on the flexible output, y_f^-, and its static value prior to the maneuver, $y_{f\text{static}}$, are also needed, for reference.

- Exit Criteria

  One simulation run of the MVS maneuver with the LA system active, collecting the required data, at each test point noted in the test point matrix in Table 5.4 is required. Also, one simulation run of the MVS maneuver without the LA system is required, for the same test points.

- Algorithm/Process

  The minimum observed value of the flexible output will be compared to the user-defined constraint. This results in a flexible output integrity metric, expressed as a percentage of the maximum flexible output displacement from the static value:

  $$y_{f,\text{integrity}} = \frac{y_f^- - y_{f\text{min}}}{\hat{y}_{f\text{min}} - y_{f\text{static}}}. \tag{5.3}$$

  Any instance where the integrity metric has a value less than zero represents a constraint violation.

- Evaluation Criteria

  The desired performance for the integrity metric defined in Eq. (5.3) is to maintain a non-negative value throughout the maneuver, but to also keep the integrity metric less than or equal to 20%. Acceptable performance for the integrity metric is any value greater than 20%. The reason this level of performance is not desirable is that it represents an excessive use of control by the LA system, which is much more than necessary to prevent a constraint violation, therefore showing that the system could be improved. Undesirable performance for the integrity metric is any value less than zero, which represents a constraint violation.

- Final Data Product

  The values of the constraint integrity metric for both the right and left wing for each test point of maneuvering flight will be listed in a table. A plot of the flexible output compared to the user-defined bound and the flexible output of a simulation without the LA system may also be presented for a selection of test points.

5.4.2.2 MOP 2.2: Rigid body output error of aircraft model during maneuvering flight

A distinguishing feature of the system under evaluation is the exploitation of the null space of the aircraft model. Generating and using a null space filter to build the $\Delta u(t)$ signal enables changes to the flexible output without affecting the rigid body output. However, this feature relies on the property of superposition present in linear systems, which may no longer be valid when applying the linear-based LA system to a nonlinear aircraft model. Errors arising from the linearization of the nonlinear aircraft model may result in changes to the rigid body output, when compared to maneuvers executed without the LA system active.

- Test Method

  The objective model will perform an MVS maneuver in order to excite the out-of-plane bending deflection of the wing. The same test method described in Section 5.4.2.1 will be sufficient for this MOP.

- Data Requirement

Table 5.4: Test Point Matrix for Objective 2

Test Point	Model No.	T_p(s)	$y_{f,\text{correction}}$ (%)
2.1	1	3	-10
2.2	1	3	-30
2.3	1	2	-10
2.4	1	2	-30
2.5	1	1	-10
2.6	1	1	-30
2.7	1	0.5	-10
2.8	1	0.5	-30
2.9	2	3	-10
2.10	2	3	-30
2.11	2	2	-10
2.12	2	2	-30
2.13	2	1	-10
2.14	2	1	-30
2.15	2	0.5	-10
2.16	2	0.5	-30
2.17	3	3	-10
2.18	3	3	-30
2.19	3	2	-10
2.20	3	2	-30
2.21	3	1	-10
2.22	3	1	-30
2.23	3	0.5	-10
2.24	3	0.5	-30
2.25	4	3	-10
2.26	4	3	-30
2.27	4	2	-10
2.28	4	2	-30
2.29	4	1	-10
2.30	4	1	-30
2.31	4	0.5	-10
2.32	4	0.5	-30
2.33	5	3	-10
2.34	5	3	-30
2.35	5	2	-10
2.36	5	2	-30
2.37	5	1	-10
2.38	5	1	-30
2.39	5	0.5	-10
2.40	5	0.5	-30

A time history of the rigid body output of the aircraft model obtained from a numerical simulation of the MVS maneuver with the LA system active will be recorded in a data log. The rigid body output used for this MOP must be the same ones used by the nominal controller of the aircraft. The data log should start from at least three seconds prior to the initiation of the maneuver and include at least three seconds of data after the completion of the maneuver. A similar data log from a numerical simulation of the MVS maneuver without the LA system is also needed, for reference.

- Exit Criteria

  One simulation run of the MVS maneuver with the LA system active, collecting the required data, at each test point noted in the test point matrix in Table 5.4 is required. Also, one simulation run of the MVS maneuver without the LA system is required, for the same test points.

- Algorithm/Process

  The rigid body output data with the LA system active will be compared to the output data without the LA system throughout the time history data log. Specifically, starting from the first point in time where the mean $\Delta u(t)$ value of all input channels is greater than zero until the end of the data log, the difference between the rigid body output values will be calculated. The mean of the absolute value of these differences will be calculated, resulting in a rigid body output mean absolute error:

$$e_{y_r} = \frac{1}{n}\sum_{i=1}^{n} |y_r(i) - \hat{y}_r(i)|, \tag{5.4}$$

  where n is the number of time steps in the sample and $\hat{y}_r(t)$ represents the data from the simulation without the LA system.

- Evaluation Criteria

  The desired performance for the rigid body output error metric defined in Eq. (5.4) is to have a mean pitch-rate absolute error less than or equal to 1°/s. Acceptable performance is a mean pitch-rate error greater than 1°/s, but less than or equal to 2°/s. Undesirable performance is a mean pitch-rate error greater than 2°/s.

  The desired performance for roll-rate or yaw-rate is to have a mean absolute error less than or equal to 2°/s. Acceptable performance is a mean absolute error greater than 2°/s, but less than or equal to 4°/s. Undesirable performance is a mean absolute error greater than 4°/s.

- Final Data Product

  The mean absolute error for each rigid body output for each test point will be listed in a table. A plot of the rigid body output compared to the rigid body output of a simulation without the LA system may also be presented for a selection of test points.

5.4.2.3 MOP 2.3: Constraint integrity of flexible output of aircraft model during gust disturbance

The primary objective of the system under evaluation is to alleviate the loads borne by the aircraft structure during maneuvering flight and when encountering gust disturbances.

- Test Method

  The objective model will be subjected to a discrete gust disturbance in order to excite the out-of-plane bending deflection of the wing. A discrete gust with a 1−cosine profile will be designed according to the specifications in Title 14 of the CFR, section 25.341 [47]. These specifications are given by the equations in

Section 2.3.1. With the aircraft flying at 20,000 ft and 160 m/s, one may make the following assumptions to define the duration and intensity of the gust:

$$\begin{aligned} Z_{mo} &= 40,000ft, \\ R_1 &= 0.8, \\ R_2 &= 0.75. \end{aligned} \tag{5.5}$$

With these assumed values, the other gust parameters are:

$$\begin{aligned} U_{ref} &= 12.6\text{m/s}, \\ F_{gz} &= 0.840, \\ F_{gm} &= 0.738, \Rightarrow \\ F_g(0\text{ft}) &= 0.789 \Rightarrow \\ F_g(20,000\text{ft}) &= 0.895 \Rightarrow \\ U_{\text{ds}} &= (12.6\text{m/s})(0.895)\left(\tfrac{H}{350\text{ft}}\right)^{1/6}. \end{aligned} \tag{5.6}$$

This last expression provides the design gust velocity, U_{ds}, and is now only a function of the size of the gust field, H, in feet, which are the two parameters needed for the spatial gust expression in Eq. 2.7. Given a starting velocity of 160 m/s and assuming that the forward velocity will remain approximately constant throughout the gust field, a given value for H will also provide the time duration of the gust, t_{gust}, used in the temporal gust expression in Eq. 2.6. The instruction from the CFR is to choose the value for H that provides the critical response, which happens for different values of H for each variant of the GTA used in this study. The values of H which provide the critical response for each model are presented in Table 5.5, along with the values for the design gust velocity, the temporal gust duration, and the minimum observed wing bending curvature, κ_{min}.

As noted for the maneuvering flight version of this MOP, the amount of cor-

Table 5.5: The gust design which results in a critical response for each GTA variant at flight condition of 160 m/s at 20,000 ft

Model No.	H (ft)	U_{ds} (m/s)	t_{gust} (s)	κ_{min} (1/m)
1	180	10.1	1.26	-0.1492
2	270	10.8	1.03	-0.2216
3	310	11.1	1.18	-0.2814
4	310	11.1	1.18	-0.3157

rection needed by the LA system is also identified as a significant parameter of this study. Therefore, each gust encounter will have two cases: a low correction (10% ±1%) and a high correction (30% ±1%), as shown in Table 5.4.

- Data Requirement

  A time history of the flexible output of the aircraft model obtained from a numerical simulation of the gust encounter will be recorded in a data log. The data log should start from at least three seconds prior to the gust encounter and include at least three seconds of data after the start of the gust encounter. The user-defined constraint on the flexible output, y_f^-, and its static value prior to the maneuver, $y_{f\text{static}}$, are also needed, for reference.

- Exit Criteria

  One simulation run of the gust encounter with the LA system active, collecting the required data, at each test point noted in the test point matrix in Table 5.4 is required. Also, one simulation run of the gust encounter without the LA system is required, for the same test points.

- Algorithm/Process

  The constraint integrity MOP for gust disturbance is defined in the same manner as for the maneuvering flight case described in Section 5.4.2.1.

- Evaluation Criteria

The evaluation criteria for gust disturbance is the same as for the maneuvering flight case described in Section 5.4.2.1.

- Final Data Product

  The values of the constraint integrity metric for both the right and left wing for each test point of gust disturbance will be listed in a table.

5.4.2.4 MOP 2.4: Rigid body output error of aircraft model during gust disturbance

A distinguishing feature of the system under evaluation is the exploitation of the null space of the aircraft model enabling changes to the flexible output without affecting the rigid body output.

- Test Method

  The objective model will subjected to a discrete gust disturbance in order to excite the out-of-plane bending deflection of the wing. The same test method described in Section 5.4.2.3 will be sufficient for this MOP.

- Data Requirement

  A time history of the rigid body output of the aircraft model obtained from a numerical simulation of the gust encounter with the LA system active will be recorded in a data log. The data log should start from at least three seconds prior to the gust encounter and include at least three seconds of data after the start of the gust encounter. A similar data log from a numerical simulation of the gust encounter without the LA system is also needed, for reference.

- Exit Criteria

  One simulation run of the gust encounter with the LA system active, collecting the required data, at each test point noted in the test point matrix in Table 5.4

is required. Also, one simulation run of the gust encounter without the LA system is required, for the same test points.

- Algorithm/Process

  The rigid body output error MOP for gust disturbance is defined in the same manner as for the maneuvering flight case described in Section 5.4.2.2.

- Evaluation Criteria

  The evaluation criteria for gust disturbance is the same as for the maneuvering flight case described in Section 5.4.2.2.

- Final Data Product

  The mean absolute error for each rigid body output for each test point will be listed in a table.

5.5 Results of Characterization

5.5.1 Objective 1: Determine limits of applicability of linear-time-invariant null space filter coupled with nonlinear system

The spill-over frequency for each model number was determined by performing a Fourier transform analysis of the rigid body output from the null space variable chirp simulation from UM/NAST. A simulation was run for each input channel of the null space filter for each model number. For each input channel simulation, the output of the three rigid body outputs was analyzed to determine the dominant frequency in the signal. The output channel frequency with the highest signal power was chosen as the spill-over frequency for that input channel. The input channel spill-over frequencies for each model number are presented in Table 5.6. Within each model number, the

Table 5.6: Results of spill-over frequency determination for Objective 1

Test Point	Model No.	Channel	Signal Power	f_{so} (Hz)	f_{so}/f_{oopb}
1.1	1	1	2.69×10^3	0.10	0.06
1.1	1	2	2.83×10^3	**0.11**	**0.06**
1.1	1	3	4.92×10^3	0.12	0.07
1.1	1	4	2.63×10^3	**0.11**	**0.06**
1.1	1	5	3.04×10^3	**0.11**	**0.06**
1.1	1	6	2.73×10^3	0.09	0.05
1.2	2	1	3.36×10^{-6}	**0.65**	**0.47**
1.2	2	2	3.20×10^{-9}	**0.65**	**0.47**
1.2	2	3	1.07×10^{-5}	**0.65**	**0.47**
1.2	2	4	1.85×10^{-6}	0.05	0.04
1.2	2	5	1.35×10^{-5}	0.05	0.04
1.2	2	6	4.71×10^{-6}	0.15	0.11
1.3	3	1	5.95×10^3	0.13	0.12
1.3	3	2	4.00×10^3	**0.11**	**0.10**
1.3	3	3	4.02×10^3	0.12	0.10
1.3	3	4	1.21×10^4	0.14	0.12
1.3	3	5	3.26×10^3	**0.11**	**0.10**
1.3	3	6	2.77×10^3	**0.11**	**0.09**
1.4	4	1	3.46×10^0	**0.15**	**0.14**
1.4	4	2	7.75×10^{-1}	**0.15**	**0.14**
1.4	4	3	6.26×10^1	**0.15**	**0.14**
1.4	4	4	8.88×10^{-1}	0.25	0.24
1.4	4	5	9.97×10^{-2}	**0.15**	**0.14**
1.4	4	6	1.74×10^0	**0.15**	**0.14**

frequency that appeared the most of the six channels is determined to be the spill-over frequency for that model number. This result is in bold font in Table 5.6.

One observation made during the determination process occurred while selecting the rigid body output channel with the most dominant signal power. In all cases, the output channel for the roll rate had the dominant signal power. The interpretation of this result is that using each of these null space filters will likely result in extraneous motion in the roll axis, more than in the pitch or yaw axes.

Note that the signal power for model 2 and model 4 was bounded, providing accurate results. However, the signal power for model 1 and model 3 grew unbounded, causing the simulation to quit. This happened even after reducing the amplitude of the chirp signal to only 0.001 and modifying the frequencies to start at $f_0 = 0.01$ Hz and increase to $f_1 = 0.015$ Hz. Therefore, only a partial chirp signal was tested and the results have a lower confidence. The most that can be said of these results is that the spill-over frequencies noted are an upper bound of the true spill-over frequency. This result shows that different null space filter can have different characteristics that may provide an improved performance for the LA system. Other methods of manipulating the objective model to generate a null space filter may produce better filters than the ones used for this study, but the ones used for this study provided the best result of the several potential null space filters investigated.

5.5.2 Objective 2: Evaluate limits of applicability of linear-based system for load alleviation through control allocation when applied to a nonlinear system

The results of MOPs 2.1 and 2.2, for maneuvering flight, are presented in Fig. 5.1. This includes the values of the constraint integrity metric for both the right and left wing and the rigid body output error for each test point. This tabular collection of results is color-coded to highlight whether the observed results are desirable (green), acceptable (yellow), or undesirable (red).

Note that the varying stiffness of the wings in each of these models results in differing levels of modeling error between the nonlinear and linearized versions of each model. All of the model variants have very little modeling error when given a low-magnitude maneuver, but that error increases for high-magnitude maneuvers. Furthermore, modeling error increases at a higher rate with increases in maneuver magnitude for the models with lower stiffness values. The MVS maneuver is a low-frequency maneuver, but has a high magnitude in order to attain a $2.5g$ load factor, which means modeling error will be amplified. Luckily, the modeling error for all

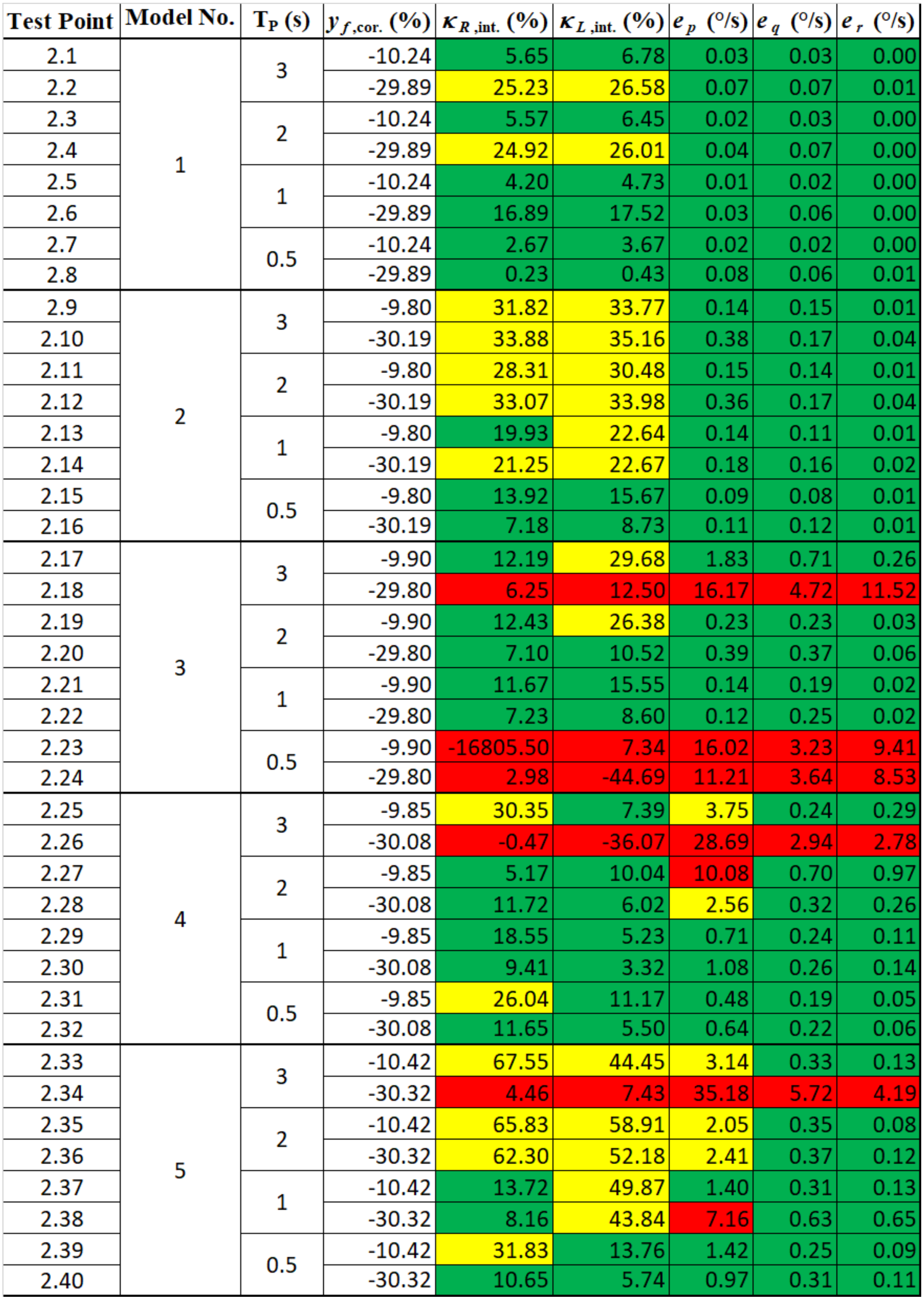

Test Point	Model No.	T_P (s)	$y_{f,\text{cor.}}$ (%)	$\kappa_{R,\text{int.}}$ (%)	$\kappa_{L,\text{int.}}$ (%)	e_p (°/s)	e_q (°/s)	e_r (°/s)
2.1	1	3	-10.24	5.65	6.78	0.03	0.03	0.00
2.2			-29.89	25.23	26.58	0.07	0.07	0.01
2.3		2	-10.24	5.57	6.45	0.02	0.03	0.00
2.4			-29.89	24.92	26.01	0.04	0.07	0.00
2.5		1	-10.24	4.20	4.73	0.01	0.02	0.00
2.6			-29.89	16.89	17.52	0.03	0.06	0.00
2.7		0.5	-10.24	2.67	3.67	0.02	0.02	0.00
2.8			-29.89	0.23	0.43	0.08	0.06	0.01
2.9	2	3	-9.80	31.82	33.77	0.14	0.15	0.01
2.10			-30.19	33.88	35.16	0.38	0.17	0.04
2.11		2	-9.80	28.31	30.48	0.15	0.14	0.01
2.12			-30.19	33.07	33.98	0.36	0.17	0.04
2.13		1	-9.80	19.93	22.64	0.14	0.11	0.01
2.14			-30.19	21.25	22.67	0.18	0.16	0.02
2.15		0.5	-9.80	13.92	15.67	0.09	0.08	0.01
2.16			-30.19	7.18	8.73	0.11	0.12	0.01
2.17	3	3	-9.90	12.19	29.68	1.83	0.71	0.26
2.18			-29.80	6.25	12.50	16.17	4.72	11.52
2.19		2	-9.90	12.43	26.38	0.23	0.23	0.03
2.20			-29.80	7.10	10.52	0.39	0.37	0.06
2.21		1	-9.90	11.67	15.55	0.14	0.19	0.02
2.22			-29.80	7.23	8.60	0.12	0.25	0.02
2.23		0.5	-9.90	-16805.50	7.34	16.02	3.23	9.41
2.24			-29.80	2.98	-44.69	11.21	3.64	8.53
2.25	4	3	-9.85	30.35	7.39	3.75	0.24	0.29
2.26			-30.08	-0.47	-36.07	28.69	2.94	2.78
2.27		2	-9.85	5.17	10.04	10.08	0.70	0.97
2.28			-30.08	11.72	6.02	2.56	0.32	0.26
2.29		1	-9.85	18.55	5.23	0.71	0.24	0.11
2.30			-30.08	9.41	3.32	1.08	0.26	0.14
2.31		0.5	-9.85	26.04	11.17	0.48	0.19	0.05
2.32			-30.08	11.65	5.50	0.64	0.22	0.06
2.33	5	3	-10.42	67.55	44.45	3.14	0.33	0.13
2.34			-30.32	4.46	7.43	35.18	5.72	4.19
2.35		2	-10.42	65.83	58.91	2.05	0.35	0.08
2.36			-30.32	62.30	52.18	2.41	0.37	0.12
2.37		1	-10.42	13.72	49.87	1.40	0.31	0.13
2.38			-30.32	8.16	43.84	7.16	0.63	0.65
2.39		0.5	-10.42	31.83	13.76	1.42	0.25	0.09
2.40			-30.32	10.65	5.74	0.97	0.31	0.11

Figure 5.1: Test Point Matrix with Results for Maneuvering Flight, Objective 2

cases of the GTA provides an overestimation of the flexible output. This means that, in general, the nominal simulations used to predict the behavior of the flexible output portray a worse situation than will actually happen for the nonlinear model. This overestimation results in a more conservative response of the LA system, which is observed in the results in Fig. 5.1.

Another observation from the results is with respect to the rigid body output error. The first axis that would start to show increased error was the roll axis. This was an interesting observation, since the MVS maneuver is purely longitudinal, but it agrees with the observations from Objective 1 of this study, where the output channel for roll rate always had a higher signal power from the Fourier transform spectral analysis. The result validates the interpretation that using each of the null space filters will likely result in extraneous motion in the roll axis, more than in the pitch or yaw axes.

For all model variants, a shorter preview horizon yields less rigid-body error and satisfied the flexible constraints with smaller margins (less excessive control use). These are desirable qualities, but one may expect that the LA system would do better when there is more time to prepare for predicted constraint violations. The reason for this improved performance likely stems from the overestimation of the linearized model, where a larger preview horizon allows that overestimation to have more influence.

Note that there are a few test points where having a long preview horizon led to instability. This occurred in the more flexible model variants with a three-second preview horizon and a desired flexible output correction of -30% (i.e., test points 2.18, 2.16, and 2.34). The interpretation for these results is that the predicted response is based on linearized models with high error, and when that high error is propagated over a longer time prediction, then the control effort is based on bad predictions, which drive the whole system unstable.

There were also two test points (2.23 and 2.24) where a 0.5-second preview horizon resulted in a high frequency, high amplitude response, which drove the system unstable. The interpretation for this result is that the very short preview coupled with the high modeling error predicted a very large constraint violation with very little time to correct, which then resulted in an unrecoverable over-correction. However, the system did not go unstable for the corresponding test points with the more flexible wings. This may be a result of the null space filter for model 4 having a higher spill-over frequency than the one for model 3, as discussed in Section 5.5.1. Another possible explanation is that the more flexible wings may absorb the energy of the high frequency, high amplitude response so that the system does not go unstable.

The results of MOPs 2.3 and 2.4, for gust disturbance are presented in Fig. 5.2. This tabular collection of results is color-coded in the same manner as for maneuvering flight.

Note that the gust disturbance represents a different kind of input for the aircraft and the LA system. This is a high-frequency disturbance, but the magnitude of the response without LA is not as high as for the MVS. This can be observed by comparing the minimum observed flexible output without LA given in Tables 5.3 and 5.5. As with results for maneuvering flight, the performance for gust disturbance was driven by the linear models, but this time the linear model of the gust effects on the aircraft is very influential. As described in Section 4.2, the current linear model of the gust effects on the aircraft model directly impacts only the rigid body velocity. The gust disturbance effect on the structure is only propagated through the dynamics from changes in the rigid body velocity. This model adds lag to the structural response, which can be compensated by using a correction factor for the linear model. For all model variants in this study, a correction factor was set to provide an overshoot of 20% for the prediction of the flexible output. As observed in Fig. 5.2, for all model variants, too short of a preview horizon yielded undesirable results, as the system could not maintain structural constraints. This is due to the

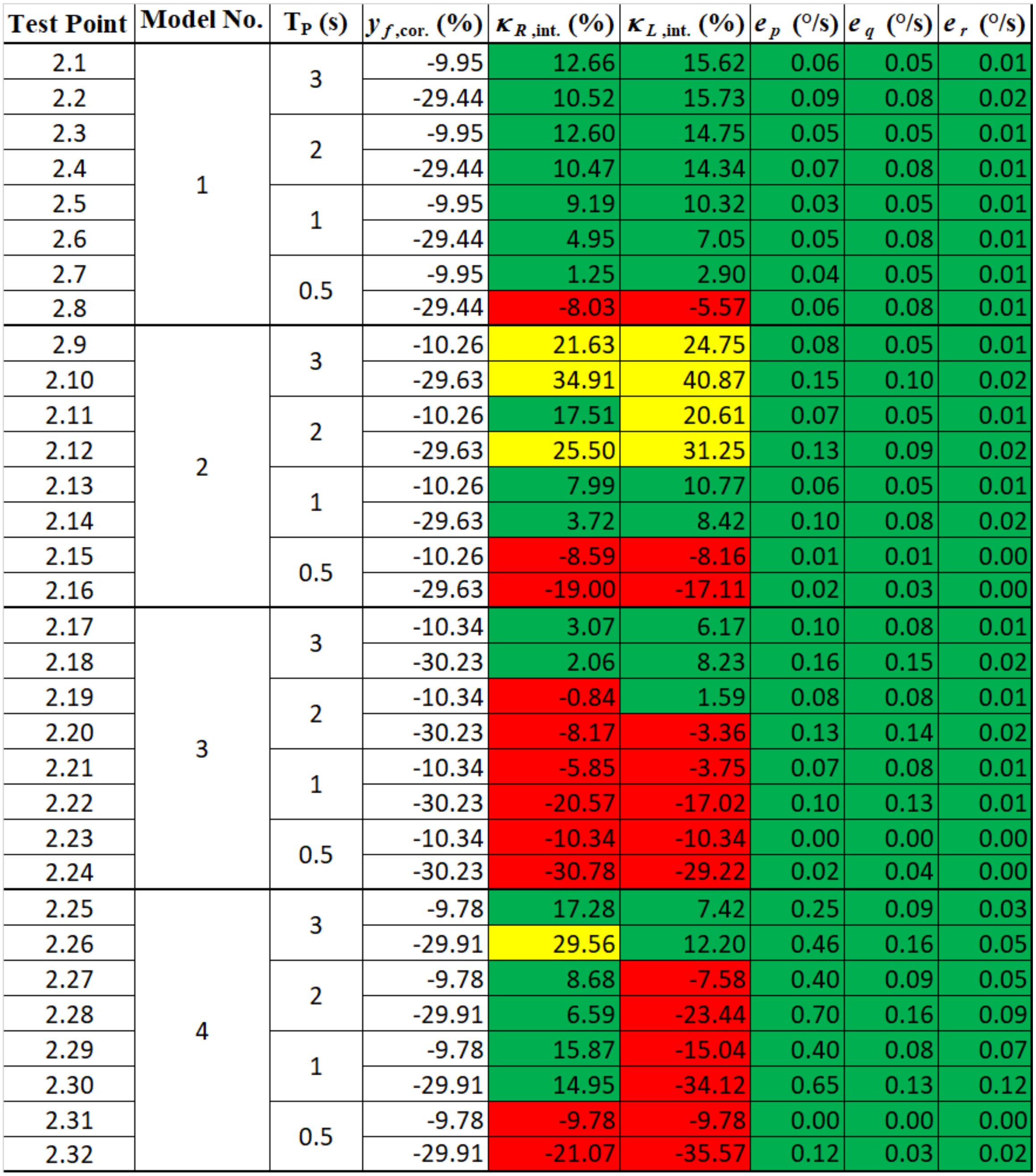

Test Point	Model No.	T_P (s)	$y_{f,\text{cor.}}$ (%)	$\kappa_{R,\text{int.}}$ (%)	$\kappa_{L,\text{int.}}$ (%)	e_p (°/s)	e_q (°/s)	e_r (°/s)
2.1	1	3	-9.95	12.66	15.62	0.06	0.05	0.01
2.2			-29.44	10.52	15.73	0.09	0.08	0.02
2.3		2	-9.95	12.60	14.75	0.05	0.05	0.01
2.4			-29.44	10.47	14.34	0.07	0.08	0.01
2.5		1	-9.95	9.19	10.32	0.03	0.05	0.01
2.6			-29.44	4.95	7.05	0.05	0.08	0.01
2.7		0.5	-9.95	1.25	2.90	0.04	0.05	0.01
2.8			-29.44	-8.03	-5.57	0.06	0.08	0.01
2.9	2	3	-10.26	21.63	24.75	0.08	0.05	0.01
2.10			-29.63	34.91	40.87	0.15	0.10	0.02
2.11		2	-10.26	17.51	20.61	0.07	0.05	0.01
2.12			-29.63	25.50	31.25	0.13	0.09	0.02
2.13		1	-10.26	7.99	10.77	0.06	0.05	0.01
2.14			-29.63	3.72	8.42	0.10	0.08	0.02
2.15		0.5	-10.26	-8.59	-8.16	0.01	0.01	0.00
2.16			-29.63	-19.00	-17.11	0.02	0.03	0.00
2.17	3	3	-10.34	3.07	6.17	0.10	0.08	0.01
2.18			-30.23	2.06	8.23	0.16	0.15	0.02
2.19		2	-10.34	-0.84	1.59	0.08	0.08	0.01
2.20			-30.23	-8.17	-3.36	0.13	0.14	0.02
2.21		1	-10.34	-5.85	-3.75	0.07	0.08	0.01
2.22			-30.23	-20.57	-17.02	0.10	0.13	0.01
2.23		0.5	-10.34	-10.34	-10.34	0.00	0.00	0.00
2.24			-30.23	-30.78	-29.22	0.02	0.04	0.00
2.25	4	3	-9.78	17.28	7.42	0.25	0.09	0.03
2.26			-29.91	29.56	12.20	0.46	0.16	0.05
2.27		2	-9.78	8.68	-7.58	0.40	0.09	0.05
2.28			-29.91	6.59	-23.44	0.70	0.16	0.09
2.29		1	-9.78	15.87	-15.04	0.40	0.08	0.07
2.30			-29.91	14.95	-34.12	0.65	0.13	0.12
2.31		0.5	-9.78	-9.78	-9.78	0.00	0.00	0.00
2.32			-29.91	-21.07	-35.57	0.12	0.03	0.02

Figure 5.2: Test Point Matrix with Results for Gust Disturbance, Objective 2

lag in the linear prediction of the gust response. As the flexibility of the aircraft model increases, the linear prediction has more lag and a longer preview is needed to maintain structural constraints.

Note also that all test points for gust disturbance had desirable rigid body error. This is because the gust disturbance does not excite as high of a structural response as the MVS, which means that there is less modeling error in the predictions from the linearized system.

5.6 Conclusions of Load Alleviation System Characterization

When considering the results of this study as a whole, the limitations of the LA system, based on invariant linear systems theory, influence the results in multiple ways. The influence on performance begins with the null space filter generated for the aircraft model. A null space filter with a higher spill-over frequency can provide desirable results for more flexible systems. This is observed between model 3 (with an estimated spill-over frequency of less than 0.1 Hz, or less than 10% of its first out-of-plane bending frequency) and model 4 (with an estimated spill-over frequency of 0.15 Hz, or 14% of its first out-of-plane bending frequency). Both of these models would be considered as *very flexible aircraft*, but there are some test cases where model 3 had poor performance, while model 4 had better performance for its equivalent test points. However, both of these models mark the amount of flexibility for the aircraft wings where this LA system starts to degrade in its ability to meet its primary and secondary objectives. Model 5 is more flexible than these two and shows a significant degradation in performance. For example, the gust disturbance test points for model 5 were not performed because the degraded performance observed in models 3 and 4, along with the undesirable performance of model 5 for maneuvering flight, showed that this level of flexibility is beyond the limits of applicability of this LA system. Therefore, in terms of an applicability limit on the flexibility of the wings, models 3 and 4 mark that limit. The LA system developed and demonstrated in this work can be applied to aircraft with wing flexibility high enough that the vertical wingtip deflection in a modest cruise is around 28-34% of half-span and the first out-of-plane bending frequency is around 1.05-1.15 Hz.

When considering the test variable of the preview horizon length, the results show that a longer preview horizon may not provide the best performance. However, this statement must be qualified by the given properties of this LA system. For very flexible aircraft models, the linearized models are known to have high modeling error when predicting the flexible wing bending curvature. In this situation, a preview that is too long drives a response that is too conservative, but it could also lead to instability. Therefore, for maneuvering flight, a shorter preview horizon performed better for this system. However, for gust response, a longer preview performed better. But once again, this statement must be taken within the context of the rudimentary method of generating the gust influence matrix (B_g) for the linear model. The B_g matrices used for these models all added significant lag to the predicted structural response to gust, so it follows that an LA system using these B_g matrices for prediction would perform poorly with only a short preview horizon. In fact, in two test points (points 2.23 and 2.31), the lag in the prediction was so high that the LA system did not even engage until the constraints were already violated. One more thing to keep in mind is that the structural response to gust is not as large as the response from maneuvers, so the gust disturbance response can have a lower weight compared to maneuver performance. With the system as it is, a 1-2 second preview horizon appears to be a good compromise for handling both low-frequency maneuvers of high-frequency gust disturbances.

CHAPTER 6

Conclusions and Recommendations

This chapter provides a summary of this work, including the main conclusions and key contributions of the LA system. Recommendations are given for future work.

6.1 Summary and Main Conclusions

This research presents the development and demonstration of a dynamic control allocation method for maneuver and gust load alleviation for flexible aircraft. The flexible aircraft is assumed to have distinct output channels for the rigid body and for the flexible dynamics. The aircraft has a nominal controller which enables it to track a specified reference trajectory by using feedback from only the rigid body output. This results in a rigid body output trajectory and a flexible output trajectory for a given reference input. The aircraft is assumed to have more control effectors than the dimension of the controlled rigid body output, which qualifies it as an over-actuated system with weak input redundancy. It follows that the rigid body output trajectory for a given reference input can be realized by multiple different selections of control effector input combinations.

The LA method developed in this work exploits the null space between the reference input and the rigid body output to control the flexible output without affecting the tracking performance. By using the null space, the control architecture decouples the two objectives of load alleviation and rigid body trajectory tracking. For a given aircraft linearized model, a null space filter is generated so that its output signal can be sent to the aircraft control effectors without affecting the rigid body output. A reduced-dimension null space variable is defined as the input to the null space filter and its trajectory is determined so that it can control the flexible output to remain within given constraints. The null space variable trajectory is found using quadratic programming and a full-horizon preview of the trajectory of the flexible output for a given reference signal.

The LA system was then enhanced, adding a method to alleviate the loads from gust disturbances on the aircraft. Then a receding horizon approach was developed to improve the robustness of the LA system to the uncertainty in the preview of the reference command and gust disturbance. With the receding horizon implementation, the preview horizon used for optimization can be shorter than the full maneuver time and chosen so that it provides a more accurate preview. This enhancement reframes the QP formulation so that it can be used iteratively for the limited preview horizon, which recedes as time moves forward. The robustness is improved as the solution is recomputed at discrete time instants.

To represent a build-up for more realism in the models used for the LA system, the impacts and modifications needed to adapt the LA system for use with LPV systems were discussed. Specifically, either an invariant null space filter based upon the initial equilibrium condition can be used, or an LPV null space filter can be used to adapt to changes in the parameter-varying aircraft dynamics. Some issues are encountered with design and use of an LPV null space filter and solutions are presented to overcome these issues. Of two solutions presented, the one involving a shift to maintain system continuity between iterations by means of the Δu signal sufficiently overcame the identified issues. Numerical investigations showed the feasibility of both the invariant and LPV null space filters, when applied to an LPV aircraft model, even as the aircraft operates away from the equilibrium condition. However, the simpler design of using the invariant null space filter, with the increased robustness of maintaining continuity with the Δu signal, was sufficient for alleviating loads for an LPV aircraft model.

Further modifications were made to adapt the LA system for use with nonlinear aircraft models. The receding horizon approach was successfully translated to a model predictive control-based control allocator function which can run on top of a nominal controller for nonlinear models and simulations. Different methods for disengaging the LA system were set forth with their respective benefits and disadvantages.

Numerical simulations have been used throughout the development to demonstrate the operation of this LA system using two aircraft models (i.e., the X-HALE and the GTA). Each aircraft model was described generally, and then in more detail for the flight conditions used to investigate the feasibility of the LA system concept. Numerical results using the full preview method with an LTI X-HALE model were presented as a proof of the LA system concept. As the system was enhanced to account for gust loads and to utilize a limited preview with receding horizon, additional numerical results showed the effect of these features. Results of LTI models using the receding horizon approach demonstrated attenuation of the flexible output by 50-80% while keeping mean absolute errors of the rigid body outputs to less than 0.25°/s. Numerical results were used to show the efficacy of the modifications made to the system while adapting it for the LPV X-HALE model. Results using the an invariant null space filter for an LPV X-HALE model demonstrated attenuation of the flexible output by 50% while keeping mean absolute errors of the rigid body outputs to less than 0.1°/s. Finally, numerical results showed the effect of the last modifications, using an MPC-based LA system on top of a nominal controller while running nonlinear dynamic simulations with the X-HALE and GTA models. Results using the an invariant null space filter for a nonlinear X-HALE model overshot a 25% goal to attenuate the flexible output by an additional 50% and yielded mean absolute errors of the rigid body outputs near 1°/s. Results using the an invariant null space filter for a nonlinear GTA model overshot a 35% goal to attenuate the flexible output by an additional 20% while keeping mean absolute errors of the rigid body outputs to less than 0.2°/s. These demonstrations showed that the LA system can successfully avoid the violation of flexible output constraints resulting from both gust disturbances and maneuvers with minimal effect on the trajectory tracking performance.

A case study to characterize this linear-based LA system identified limits of applicability for nonlinear aircraft models and resulted in recommended design parameters. The case study observed the effect of: (1) different values of wing flexibility, (2) the length of the preview horizon used by the MPC-based system, and (3) the amount of alleviation required of the system. The results of the case study showed that the LA system developed and demonstrated in this work can be applied to aircraft with wing flexibility high enough that the vertical wingtip deflection is around 28-34% of half-span in cruise and the first out-of-plane bending frequency is around 1.05-1.15 Hz. The case study also showed that a preview horizon of 1-2 seconds provides a good compromise for handling both low-frequency maneuvers of high-frequency gust disturbances.

6.2 Key Contributions

The key contributions of this dissertation can be summarized as follows:

- Development of a new method for MLA and GLA using linear and parameter-varying systems to modify the control allocation of an aircraft to alleviate loads. This method exploits the structure of input redundancy to decouple the rigid body and flexible response in order to alleviate loads during maneuvers and gusts while also keeping desired rigid-body trajectory.
- Introduction of a receding horizon approach as part of the LA system to account

for stochastic gust disturbances and maneuvers with limited preview. The robustness of the system improved as the solution was iteratively recomputed at discrete time instants.

- Successful translation of the load alleviation system to a model predictive control-based control allocator function which can run on top of a nominal controller for nonlinear models and simulations. Numerical demonstrations showed that the system can be added to an aircraft with nominal controller to successfully avoid the violation of flexible output constraints resulting from both gust disturbances and maneuvers with minimal effect on the trajectory tracking performance.
- Characterization of the limits of applicability for this linear-based LA system when applied to nonlinear aircraft models. This characterization showed a limit with respect to the aircraft stiffness and resulted in a recommendation for a time preview horizon.

6.3 Recommendations for Future Work

Over the course of this study, some aspects of the performance of this LA system revealed areas for needed improvement.

- Applying the linear-based LA system to nonlinear aircraft models often resulted in excessive control use to get an overly-conservative result. The system performance may be improved through some sort of scaling factor on the predicted trajectory of the flexible output from the linear model when there is a known modeling error. This issue may be approached by adjusting the constraint of the QP problem to compensate for modeling error. Another idea is to use a weak slack variable penalty, but not so weak that it actually results in constraint violation.

- The LA system developed in this work utilized an MPC-based control allocator which found optimal control trajectories based on flexible output dynamics from linear simulation predictions. The prediction portion of this system can be improved through the use of nonlinear models and simulations. This shift to nonlinear MPC would provide less modeling error of the flexible output trajectory, which would also help to decrease the excessive control use observed in this work. Nonlinear MPC requires a program which can run dynamic simulations for any given initial condition of aircraft states and inputs. The dynamic simulation module in Ver. 4.2.0 of UM/NAST contains some underlying assumptions that the initial condition of the model is static. The capability to run dynamic simulations with non-static initial conditions is recommended for development and integration into UM/NAST.

- The null space filters found by the methods described in this work did not always result in stable systems which exploited the null space throughout a frequency band of interest. Theoretically, the null space filter should prevent null space variable trajectories from spilling over into the rigid body output. In practice, the degree of attenuation between null space variable and rigid body output varied with input frequency and sometimes resulted in amplification for certain input frequencies. Null space filter generation may be improved by techniques similar to feed-forward model matching.

- The LA system developed in this work used an LTI null space filter applied to nonlinear aircraft models. The development of a nonlinear null space filter may improve the performance of this system as it would provide a better exploitation of the nonlinear null space of the aircraft. Some alternate approach of output decoupling may provide opportunities to develop such a nonlinear way to decouple the flexible output control from the rigid body output tracking performance.

- As aircraft flexibility increases, more states may be needed to provide an accurate representation of the flexible structure in free flight. This increase in model size would result in increased computation time for the predictions used by the LA system in this work. This computation time is a key limitation for applying MPC to physical systems. Therefore, model reduction techniques should be utilized in order to increase the technological readiness of this system for eventual application to physical aircraft.

- This LA system used a full aircraft state (or estimated state) for the predictions needed to determine the optimal null space variable trajectory. Methods to accurately model and predict the flexible output at key locations on the structure based on a few measurements would decrease the model size and computation time needed for prediction.

- The gust influence matrix used for predicting the aircraft response to gust disturbance was based on rigid body dynamics and not on direct aerodynamic influence on the aircraft structure. This resulted in lag for the flexible response, compared to the nonlinear simulation results. A more accurate linearization of the gust influence matrix would improve the performance of the LTI-based LA system on nonlinear aircraft.

APPENDIX A

Considerations for Implementing Load Alleviation System with Unique X-HALE Controller

As shown in Fig. 4.3, the architecture for the nominal controller of the X-HALE is not based solely on an error signal of the difference between a measured output and the reference signal. Therefore, the closed loop system derivation differs slightly from the one presented in Sections 3.1.2 and 3.2.1. Specifically, the nominal controller has two inputs, r and y_r, instead of only one. Observing the pitch control law helps to clarify this point:

$$\begin{aligned} \tau_q &= \left(K_{qp} + \tfrac{K_{qi}}{s}\right)\left[K_\theta\left(\tfrac{1}{s}r_q - \tfrac{1}{s}y_{r_q}\right) - y_{r_q}\right] \Rightarrow \\ &= \left(K_{qp} + \tfrac{K_{qi}}{s}\right)\tfrac{K_\theta}{s}r_q - \left(K_{qp} + \tfrac{K_{qi}}{s}\right)\left(\tfrac{K_\theta}{s} + 1\right)y_{r_q}. \end{aligned} \tag{A.1}$$

Therefore, the nominal control controller can be expressed as two components, one for each input:

$$u_0 = C_r(s)r + C_y(s)y_r. \tag{A.2}$$

With this understanding, one can follow the guideline of the steps used in Section 3.2.1 to relate the flexible output to the reference command and the null space variable. First, the closed loop rigid output response of the X-HALE with its nominal controller (Eq. (A.2) is calculated as

$$\begin{aligned} y_r &= G_{ru}(s)[u_0 + \Delta u] + G_{rg}(s)g, \Rightarrow \\ &= G_{ru}(s)[C_r(s)r + C_y(s)y_r] + G_{rg}(s)g, \Rightarrow \\ &= [I - G_{ru}(s)C_y(s)]^{-1}G_{ru}(s)C_r(s)r \\ &+[I - G_{ru}(s)C_y(s)]^{-1}G_{rg}(s)g. \end{aligned} \tag{A.3}$$

Then the flexible output response of the X-HALE is

$$\begin{aligned} y_f &= G_{fu}(s)\left[u_0 + \Delta u\right] + G_{fg}(s)g \Rightarrow \\ y_f &= G_{fu}(s)\left[C_r(s)r + C_y(s)y_r + N(s)v\right] + G_{fg}(s)g \end{aligned} \tag{A.4}$$

Inserting Eq. (A.3) into Eq. (A.4) yields

$$\begin{aligned} y_f &= G_{fu}(s)C_r(s)r \\ &+G_{fu}(s)C_y(s)\left(I - G_{ru}(s)C_y(s)\right)^{-1}G_{ru}(s)C_r(s)r(s) \\ &+G_{fu}(s)C_y(s)\left(I - G_{ru}(s)C_y(s)\right)^{-1}G_{rg}(s)g \\ &+G_{fu}(s)N(s)v + G_{fg}(s)g, \Rightarrow \\ y_f &= \underbrace{\left[G_{fu}(s)C_r(s) + G_{fu}(s)C_y(s)\left(I - G_{ru}(s)C_y(s)\right)^{-1}G_{ru}(s)C_r(s)\right]}_{H_{fr,\mathrm{X}}(s)} r \\ &+ \underbrace{\left[G_{fg}(s) + G_{fu}(s)C_y(s)\left(I - G_{ru}(s)C_y(s)\right)^{-1}G_{rg}(s)\right]}_{H_{fg,\mathrm{X}}(s)} g \\ &+ \underbrace{G_{fu}(s)N(s)}_{H_{fv}(s)} v, \end{aligned} \tag{A.5}$$

which is expressed as the following state space representation of the closed loop system:

$$\begin{aligned}\dot{x}_{\mathrm{CL,X}}(t) &= A_{\mathrm{CL,X}}x_{\mathrm{CL,X}}(t) + B_{r,\mathrm{CL,X}}r(t) + B_{g,\mathrm{CL,X}}g(t) + B_{v,\mathrm{CL,X}}v(t) \\ y_f(t) &= C_{f,\mathrm{CL,X}}x_{\mathrm{CL,X}}(t).\end{aligned} \tag{A.6}$$

This last expression is the same form as Eq. (3.24), meaning that it conforms to the remaining derivations and formulations for the QP problem in Section 3.2.1.

One other unique characteristic of the X-HALE control system is that it has roll spoilers for its roll control, which can only deflect in one direction. In order to restrict the QP problem to only find physically feasible solutions for the X-HALE roll spoiler input channel, the deflection limitation must be included in the QP constraints. This is accomplished by first establishing a relationship between the null space variable and the roll spoiler channels of the $\Delta u(t)$ signal. Observing the control architecture in Fig. 3.2, the desired relationship is expressed by the roll spoiler output channels of the null space filter, i.e.,

$$\Delta u_R = N_{Rv}(s)v. \tag{A.7}$$

The next step is to determine the control signal used for the roll spoiler channels as part of the predicted response to r and g from the nominal controller. This can be accomplished by augmenting the flexible output from the aircraft model with channels to observe the roll spoiler input channels. In state space format, this would utilize a feed-forward D matrix and extra rows with zero value to the output C matrix. Let $u_{0,R}$ express the nominal roll spoiler input signal from the closed loop response to r and g. Then setting the sum of $u_{0,R}$ and Eq. (A.7) in relation to the deflection bounds yields the following constraints:

$$\begin{aligned} &LB_R \leq u_{0,R} + \Delta u_r \leq UB_R \Leftrightarrow \\ &N_{Rv}(s)v \geq LB_R - u_{0,R}, \\ &N_{Rv}(s)v \leq UB_R - u_{0,R}. \end{aligned} \tag{A.8}$$

When using a discrete-time format, the trajectory $\Delta u_R(t)$ is represented by the multiplication of Toeplitz matrix $\mathbf{N}_{Rv}$ and $\mathbf{v}$ (sampled $v(t)$ arranged in a single-column vector). Combining this with the total nominal roll spoiler trajectory, $u_{0,R}(t)$, sampled and arranged in a single-column vector, $\mathbf{u}_{0,R}$, the constraints for the deflection bounds can be included in the QP problem to find the optimal $v(t)$, e.g.,

$$\begin{aligned} \min_{\mathbf{v}} \quad & \mathbf{v}^{\mathrm{T}}\mathbf{v}, \\ \text{s.t.} \quad & \mathbf{H}_{fv}\mathbf{v} \leq y_f^+ - \mathbf{y}_{fr}, \\ & -\mathbf{H}_{fv}\mathbf{v} \leq -y_f^- + \mathbf{y}_{fr}, \\ & \mathbf{N}_{Rv}\mathbf{v} \leq UB_R - \mathbf{u}_{0,R}, \\ & -\mathbf{N}_{Rv}\mathbf{v} \leq -LB_R + \mathbf{u}_{0,R}. \end{aligned} \tag{A.9}$$

This QP formulation has the same disclaimers as explained in the main text. This same structure can be used to include the constraints of all control surfaces, but it was most important to include the roll spoiler constraints because of the one-directional nature of the control surface. The other option is to leave these constraints out of the QP problem and just limit the total input signal $u(t) = u_0(t) + \Delta u(t)$ after solving the QP problem. However, this option does not utilize the QP solver to find a realistic optimal solution, which may result in suboptimal performance.

APPENDIX B

Augmenting the Reference Signal with the Gust Disturbance Signal

As described in Section 3.4.1, the adaptation process of the LA system for the MPC framework included a switch for the prediction method. This involved a change from using Simulink to simulate the preview horizon to using standard linear simulation functions with closed loop representations of the system. Adding the gust disturbance signal to the closed loop system requires special consideration because the gust signal and the reference signal have different insertion points to the system. The reference signal is an input to the nominal controller and the gust signal is an input directly to the state of the aircraft, but the rigid body response of both these signals is then fed back through the nominal controller which then continues to influence to aircraft. Standard linear simulation functions can handle multiple inputs, but often all channels need to have the same insertion point for the system. Therefore, in order for the system developed in this work to conform to the linear simulation function, the gust disturbance signal needs to be augmented to the reference signal and then augmented to the input signal to the aircraft. In order to derive an equivalent system, the portion for the nominal controller would need to be adjusted so that it processes the error signal of the difference between the reference and the rigid body output, but that it does not influence the gust disturbance signal, i.e.,

$$\begin{aligned} y_r &= G_{ru}(s)C(s)[r - y_r] + G_{rg}(s)Ig, \Rightarrow \\ &= [I + G_{ru}(s)C(s)]^{-1}G_{ru}(s)C(s)r + [I + G_{ru}(s)C(s)]^{-1}G_{rg}(s)g, \Rightarrow \\ &= [I + G_{ru}(s)C(s)]^{-1}G_{rug}(s)C_{ueg}(s) \begin{bmatrix} r \\ g \end{bmatrix}, \end{aligned} \tag{B.1}$$

where the aircraft system has the gust influence portion augmented to the control signal input portion (i.e., $y_r = G_{rug}(s)[u, g]^{\mathrm{T}}$). Considering the controller portion, handling the augmented signal can be accomplished with a block diagonal form using an identity matrix, i.e.,

$$\begin{bmatrix} u \\ g \end{bmatrix} = \underbrace{\begin{bmatrix} C(s) & 0 \\ 0 & I \end{bmatrix}}_{C_{ueg}(s)} \begin{bmatrix} r \\ g \end{bmatrix}, \tag{B.2}$$

where $C(s)$ is the nominal controller and the augmented block diagonal form is $C_{ueg}(s)$. When considering the state space form of the controller, the $C_{ueg}(A)$ matrix would be unchanged from the original $C(A)$ matrix, the $C_{ueg}(B)$ matrix would have three additional columns of zeros on the right (because $g \in \mathbb{R}^3$), the $C_{ueg}(C)$ matrix would have three additional rows of zeros on the bottom, and the $C_{ueg}(D)$ matrix would be a block diagonal matrix of the original $C(D)$ and I_3. The flexible output in this case is

$$\begin{aligned} y_f &= G_{fu}(s)\left[u_0 + \Delta u\right] + G_{fg}(s)g \Rightarrow \\ y_f &= G_{fu}(s)\left[C(s)r - C(s)y_r + N(s)v\right] + G_{fg}(s)g \end{aligned} \tag{B.3}$$

Inserting Eq. (B.1) into Eq. (B.3) yields

$$\begin{aligned}
y_f &= G_{fu}(s)C(s)r \\
&\quad -G_{fu}(s)C(s)[I+G_{ru}(s)C(s)]^{-1}G_{rug}(s)C_{ueg}(s)\begin{bmatrix} r \\ g \end{bmatrix} \\
&\quad +G_{fu}(s)N(s)v+G_{fg}(s)g, \Rightarrow \\
y_f &= G_{fug}(s)C_{ueg}(s)\begin{bmatrix} r \\ g \end{bmatrix} \\
&\quad -G_{fu}(s)C(s)[I+G_{ru}(s)C(s)]^{-1}G_{rug}(s)C_{ueg}(s)\begin{bmatrix} r \\ g \end{bmatrix} \\
&\quad +G_{fu}(s)N(s)v,
\end{aligned} \tag{B.4}$$

where, as with the rigid aircraft case, the system with the flexible output has the gust influence portion augmented to the control signal input portion (i.e., $y_f = G_{fug}(s)[u, g]^{\mathrm{T}}$). This system is decoupled between the augmented reference and gust signal and the input signal from v. Therefore, the first portion is now in an acceptable form for linear simulation predictions. Because the system is decoupled and by taking advantage of the superposition property, the second portion, with the input signal from v, can be run in a separate linear simulation and added to the results to obtain the full flexible response.

APPENDIX C

UM/NAST Model Properties for X-HALE and GTA

Details for the properties of the models used in this study are presented here. The reference axes are defined with the origin in the center of the aircraft, the x-axis pointing along the right wing, the y-axis pointing to the front of the aircraft, and the z-axis pointing upward, according to the "right-hand rule." The locations of the keypoints are first established and then used to define the various structural members, which contain the structural elements and properties for the structural dynamics of the aircraft. The labels for the structural members use a W for wings, an F for fuselage, and a T for tails. Subscripts for the labels distinguish between the right and left sides of the aircraft, or top and bottom, or fore and aft, and numerical subscripts for multiple elements of similar type (when necessary) increase in value from the center of the aircraft.

The locations of the keypoints used to establish the X-HALE model are listed in Table C.1 and its members are listed in Table C.2. For the X-HALE model, a B is used for booms, which extend aft from the five fuselage-like pods to the all-movable tails. A V is used for ventral fins, which extend downward from the three middle booms. An R is used for roll spoiler control surfaces on the outboard wing sections. For the purposes of load alleviation, the wings are identified as the critical structural components and are therefore, the only structural members treated and analyzed for their flexible structural response. The structural stiffness values of the wing members are listed in Table C.3. Note that these values are twice the stiffness, with respect to the actual aircraft, as explained in Section 4.1.1. Also note that the furthest outboard wing members have some unique stiffness values on account of having an unclamped boundary condition at the wingtip.

The locations of the keypoints used to establish the GTA model are listed in Table C.4 and its members are listed in Table C.5. For the GTA model, AIL is used for ailerons, ELV is used for elevators, FLP is used for flaps, and RDR is used for rudder control surfaces. As was the case with the X-HALE, for the purposes of load alleviation, the wings are identified as the critical structural components and are therefore, the only structural members treated and analyzed for their flexible structural response. The structural stiffness values of the wing members vary along the wingspan. For example, there is one structural element from keypoint one to keypoint five for W_R and then 16 more elements, spaced one every half-meter, till the wingtip. The stiffness values for each of these elements from the wing root to the wingtip are listed in Table C.6. Note that all off-diagonal stiffness values are equal to zero.

For the characterization study of the LA system described in Chapter 5, five variants of the GTA were established, with varying wing stiffness values. The baseline stiffness in Table C.6 corresponds with model number two of the characterization study. Model number one was defined by multiplying the baseline stiffness values for K_{11}, K_{33}, and K_{44} by a factor of 1.750, while leaving K_{22} unchanged. Similarly, for model numbers three through five, stiffness values were multiplied by a factor of 0.700, 0.583, and 0.500, respectively.

Table C.1: Keypoint locations for the beam reference axes of the X-HALE (units: meters)

Keypoint	x	y	z	Description
1	0.0000	0.0000	0.0000	Body center
2	1.0000	0.0000	0.0000	Right tip of W_{R1}
3	-1.0000	0.0000	0.0000	Left tip of W_{L1}
4	2.0000	0.0000	0.0000	Right tip of W_{R2}
5	-2.0000	0.0000	0.0000	Left tip of W_{L2}
6	2.9848	0.0000	0.1737	Right tip of W_{R3}
7	-2.9848	0.0000	0.1737	Left tip of W_{L3}
8	1.0000	0.0000	-0.2010	Bottom of F_{R1}
9	-1.0000	0.0000	-0.2010	Bottom of F_{L1}
10	2.0000	0.0000	-0.2010	Bottom of F_{R2}
11	-2.0000	0.0000	-0.2010	Bottom of F_{L2}
12	1.0000	-0.6970	0.0000	End of B_{R1}
13	0.7600	-0.6970	0.0000	Left tip of T_{R1}
14	1.2400	-0.6970	0.0000	Right tip of T_{R1}
15	-1.0000	-0.6970	0.0000	End of B_{L1}
16	-0.7600	-0.6970	0.0000	Right tip of T_{L1}
17	-1.2400	-0.6970	0.0000	Left tip of T_{L1}
18	2.0000	-0.6970	0.0000	End of B_{R2}
19	1.7600	-0.6970	0.0000	Left tip of T_{R2}
20	2.2400	-0.6970	0.0000	Right tip of T_{R2}
21	-2.0000	-0.6970	0.0000	End of B_{L2}
22	-1.7600	-0.6970	0.0000	Right tip of T_{L2}
23	-2.2400	-0.6970	0.0000	Left tip of T_{L2}
24	0.0000	0.0000	-0.2010	Bottom of F_0
25	0.0000	-0.9440	0.0000	End of B_0
26	0.0000	-0.9440	0.2400	Top tip of T_0
27	0.0000	-0.9440	-0.1480	Bottom tip of T_0
28	2.2482	0.0000	0.0438	Left tip of R_R
29	2.7347	0.0000	0.1295	Right tip of R_R
30	-2.2482	0.0000	0.0438	Right tip of R_L
31	-2.7347	0.0000	0.1295	Left tip of R_L
32	0.0000	-0.9440	-0.1400	Bottom aft corner of V_0
33	1.0000	-0.6970	-0.1400	Bottom aft corner of V_{R1}
34	-1.0000	-0.6970	-0.1400	Bottom aft corner of V_{L1}

Table C.2: Structural member definitions for finite element model of the X-HALE

Member	Keypoints	No. of Elements	Flexible Element?	Lifting Surface?
F_0	1, 24	1	No	Yes
B_0	1, 25	1	No	No
$T_{0,t}$	25, 26	1	No	Yes
$T_{0,b}$	25, 27	1	No	Yes
W_{R1}	1, 2	1	Yes	Yes
F_{R1}	2, 8	1	No	Yes
B_{R1}	2, 12	1	No	No
$T_{R1,l}$	12, 13	1	No	Yes
$T_{R1,r}$	12, 14	1	No	Yes
W_{R2}	2, 4	1	Yes	Yes
F_{R2}	4, 10	1	No	Yes
B_{R2}	4, 18	1	No	No
$T_{R2,l}$	18, 19	1	No	Yes
$T_{R2,r}$	18, 20	1	No	Yes
W_{R3}	4, 6	1	Yes	Yes
W_{L1}	1, 3	1	Yes	Yes
F_{L1}	3, 9	1	No	Yes
B_{L1}	3, 15	1	No	No
$T_{L1,r}$	15, 16	1	No	Yes
$T_{L1,l}$	15, 17	1	No	Yes
W_{L2}	3, 5	1	Yes	Yes
F_{L2}	5, 11	1	No	Yes
B_{L2}	5, 21	1	No	No
$T_{L2,r}$	21, 22	1	No	Yes
$T_{L2,l}$	21, 23	1	No	Yes
W_{L3}	5, 7	1	Yes	Yes
V_0	25, 32	1	No	Yes
V_{R1}	12, 33	1	No	Yes
V_{L1}	15, 34	1	No	Yes

Table C.3: Structural stiffness definitions for wing members of the X-HALE model

Stiffness	Value	Applicable Members
K_{11}	4.2816×10^6	all
K_{12}	0.0000×10^1	all
K_{13}	3.0882×10^3	all
K_{14}	-9.8113×10^4	all
K_{22}	1.1400×10^2	W_{L1}, W_{L2}, W_{R1}, W_{R2}
K_{22}	1.0800×10^2	W_{L3}, W_{R3}
K_{23}	0.0000×10^1	all
K_{24}	0.0000×10^1	all
K_{33}	2.1000×10^2	W_{L1}, W_{L2}, W_{R1}, W_{R2}
K_{33}	1.5800×10^2	W_{L3}, W_{R3}
K_{34}	-9.2689×10^1	all
K_{44}	1.2702×10^4	all

Table C.4: Keypoint locations for the beam reference axes of the GTA (units: meters)

Keypoint	x	y	z	Description
1	0.00	0.00	0.00	Body center
2	0.00	8.00	0.00	Foremost tip of F_f
3	0.00	-12.00	0.00	Root of T_v
4	0.00	-14.00	0.00	Aftmost tip of F_a
5	1.50	0.00	1.00	Root of W_R and left tip of FLP_R
6	2.00	0.00	1.00	Intermediate point of W_R
7	2.50	0.00	1.00	Intermediate point of W_R
8	3.00	0.00	1.00	Intermediate point of W_R
9	3.50	0.00	1.00	Right tip of FLP_R
10	4.00	0.00	1.00	Intermediate point of W_R
11	5.00	0.00	1.00	Intermediate point of W_R
12	6.00	0.00	1.00	Left tip of AIL_R
13	6.50	0.00	1.00	Intermediate point of W_R
14	7.00	0.00	1.00	Intermediate point of W_R
15	7.50	0.00	1.00	Intermediate point of W_R
16	8.00	0.00	1.00	Intermediate point of W_R
17	8.50	0.00	1.00	Intermediate point of W_R
18	9.00	0.00	1.00	Right tip of AIL_R
19	9.50	0.00	1.00	Wingtip of W_R
20	-1.50	0.00	1.00	Root of W_L and right tip of FLP_L
21	-2.00	0.00	1.00	Intermediate point of W_L
22	-2.50	0.00	1.00	Intermediate point of W_L
23	-3.00	0.00	1.00	Intermediate point of W_L
24	-3.50	0.00	1.00	Left tip of FLP_L
25	-4.00	0.00	1.00	Intermediate point of W_L
26	-5.00	0.00	1.00	Intermediate point of W_L
27	-6.00	0.00	1.00	Right tip of AIL_L
28	-6.50	0.00	1.00	Intermediate point of W_L
29	-7.00	0.00	1.00	Intermediate point of W_L
30	-7.50	0.00	1.00	Intermediate point of W_L
31	-8.00	0.00	1.00	Intermediate point of W_L
32	-8.50	0.00	1.00	Intermediate point of W_L
33	-9.00	0.00	1.00	Left tip of AIL_L
34	-9.50	0.00	1.00	Wingtip of W_L
35	0.00	-12.00	3.00	Lower tip of RDR
36	0.00	-12.00	9.00	Upper tip of T_v and RDR
37	2.00	-12.00	9.00	Left tip of ELV_R
38	4.00	-12.00	9.00	Right tip of T_h and ELV_R
39	-2.00	-12.00	9.00	Right tip of ELV_L
40	-4.00	-12.00	9.00	Left tip of T_h and ELV_L

Table C.5: Structural member definitions for finite element model of the GTA

Member	Keypoints	No. of Elements	Flexible Element?	Lifting Surface?
F_f	1, 2	40	No	No
F_a	1, 3-4	7	No	No
W_R	1, 5-19	17	Yes	Yes
W_L	1, 20-34	17	Yes	Yes
T_v	3, 35-36	9	No	Yes
$T_{h,r}$	36-38	7	No	Yes
$T_{h,l}$	36, 39-40	7	No	Yes

Table C.6: Structural stiffness definitions for elements along wingspan of the baseline GTA model

Element	K_{11}	K_{22}	K_{33}	K_{44}
1	2.00×10^{12}	1.16×10^{9}	8.60×10^{7}	8.60×10^{9}
2	1.94×10^{10}	5.20×10^{7}	8.60×10^{6}	3.86×10^{9}
3	1.90×10^{9}	5.09×10^{6}	8.60×10^{5}	3.77×10^{8}
4	1.84×10^{9}	4.93×10^{6}	8.60×10^{5}	3.66×10^{8}
5	1.78×10^{9}	4.77×10^{6}	8.60×10^{5}	3.54×10^{8}
6	1.70×10^{9}	4.58×10^{6}	8.60×10^{5}	3.40×10^{8}
7	1.62×10^{9}	4.36×10^{6}	8.60×10^{5}	3.23×10^{8}
8	1.54×10^{9}	4.09×10^{6}	8.60×10^{5}	3.03×10^{8}
9	1.42×10^{9}	3.82×10^{6}	8.60×10^{5}	2.84×10^{8}
10	1.30×10^{9}	3.50×10^{6}	8.60×10^{5}	2.60×10^{8}
11	1.18×10^{9}	3.18×10^{6}	8.60×10^{5}	2.36×10^{8}
12	1.04×10^{9}	2.80×10^{6}	8.60×10^{5}	2.08×10^{8}
13	9.00×10^{8}	2.40×10^{6}	8.60×10^{5}	1.78×10^{8}
14	7.40×10^{8}	1.97×10^{6}	8.60×10^{5}	1.46×10^{8}
15	5.80×10^{8}	1.53×10^{6}	8.60×10^{5}	1.14×10^{8}
16	4.00×10^{8}	1.05×10^{6}	8.60×10^{5}	7.80×10^{7}
17	2.00×10^{8}	5.38×10^{5}	8.60×10^{5}	4.00×10^{7}

BIBLIOGRAPHY

[1] White, R. J., "Improving the Airplane Efficiency by Use of Wing Maneuver Load Alleviation," *Journal of Aircraft*, Vol. 8, No. 10, 1971, pp. 769–775.

[2] Hoblit, F. M., *Gust Loads on Aircraft: Concepts and Applications*, American Institute of Aeronautics and Astronautics, Inc., Washington, DC, 1988.

[3] Harpoothian, E. and Oswald, W. B., "Use of Ailerons to Reduce Wing Loads," U.S. Pat. 2,742,24, 1949, Douglas Aircraft Co., Santa Monica, Calif.

[4] Komoda, M., "Optimality Study of a Gust Alleviation System for Light Wing-loading STOL Aircraft," Tech. Rep. NASA-TN-D-8180, NASA, Feb 1976.

[5] Regan, C. D. and Jutte, C. V., "Survey of Applications of Active Control Technology for Gust Alleviation and New Challenges for Lighter-weight Aircraft," Tech. Rep. NASA/TM-2012-216008, NASA, Apr 2012.

[6] Guo, S., Fu, Q., and Sensburg, O. T., "Optimal Design of a Passive Gust Alleviation Device for a Flying Wing Aircraft," *12th AIAA Aviation Technology, Integration, and Operations (ATIO) Conference and 14th AIAA/ISSM*, AIAA, Indianapolis, Indiana, Sep 2012, p. 5625.

[7] Guo, S. and Sensburg, O. T., "Wind Tunnel Model and Test to Evaluate the Effectiveness of a Passive Gust Alleviation Device for a Flying Wing Aircraft," Tech. Rep. FA9550-14-1-0408, Cranfield University, Mar 2016.

[8] Fonte, F., Toffol, F., and Ricci, S., "Design of a Wing Tip Device for Active Maneuver and Gust Load Alleviation," *2018 AIAA/ASCE/AHS/ASC Structures, Structural Dynamics, and Materials Conference*, 2018, p. 1442.

[9] Nguyen, N. T., "Elastically Shaped Future Air Vehicle Concept," *NASA Innovation Fund Award 2010 Report*, Submitted to NASA Innovative Partnerships Program, Oct 2010.

[10] Nguyen, N., Trinh, K., Reynolds, K., Kless, J., Aftosmis, M., Urnes, J., and Ippolito, C., "Elastically Shaped Wing Optimization and Aircraft Concept for Improved Cruise Efficiency," *51st AIAA Aerospace Sciences Meeting*, Jan 2013, p. 0141.

[11] Urnes, J., Nguyen, N., Ippolito, C., Totah, J., Trinh, K., and Ting, E., "A Mission Adaptive Variable Camber Flap Control System to Optimize High Lift and Cruise Lift to Drag Ratios of Future N+3 Transport Aircraft," *51st AIAA Aerospace Sciences Meeting*, Jan 2013, p. 0214.

[12] Nguyen, N., Ting, E., Chaparro, D., Drew, M., and Swei, S., "Multi-Objective Flight Control for Drag Minimization and Load Alleviation of High-Aspect Ratio Flexible Wing Aircraft," *AIAA Scitech 2017 Forum*, Jan 2017, p. 1589.

[13] Nguyen, N., Swei, S., and Ting, E., "Adaptive Linear Quadratic Gaussian Optimal Control Modification for Flutter Suppression of Adaptive Wing," *AIAA Scitech 2015 Forum*, Jan 2015, p. 0118.

[14] Nguyen, N. and Hashemi, K., "Multi-Objective Flight Control for Ride Quality Improvement for Flexible Aircraft," *AIAA Scitech 2020 Forum*, Jan 2020, p. 1623.

[15] Precup, N., Mor, M., and Livne, E., "Design, Construction, and Tests of an Aeroelastic Wind Tunnel Model of a Variable Camber Continuous Trailing Edge Flap (VCCTEF) Concept Wing," *32nd AIAA Applied Aerodynamics Conference*, AIAA AVIATION Forum, Jun 2014, p. 2442.

[16] Nguyen, N. T., Precup, N., Urnes, J. M., Nelson, C., Lebofsky, S., Ting, E., and Livne, E., "Experimental Investigation of a Flexible Wing with a Variable Camber Continuous Trailing Edge Flap Design," *32nd AIAA Applied Aerodynamics Conference*, AIAA AVIATION Forum, Jun 2014, p. 2441.

[17] Hargrove, W. J., "The C-5A Active Lift Distribution Control System," Tech. Rep. NASA-N76-31148, NASA, Aug 1976.

[18] Yang, Y., Wu, Z., and Yang, C., "Control Surface Efficiency Analysis and Utilization of an Elastic Airplane for Maneuver Loads Alleviation," *54th AIAA/ASME/ASCE/AHS/ASC Structures, Structural Dynamics, and Materials Conference*, 2013, pp. 1–7.

[19] Xu, J. and Kroo, I., "Aircraft Design with Active Load Alleviation and Natural Laminar Flow," *Journal of Aircraft*, Vol. 51, No. 5, 2014, pp. 1532–1545.

[20] Dillsaver, M. J., Cesnik, C. E. S., and Kolmanovsky, I. V., "Gust Load Alleviation Control for Very Flexible Aircraft," *AIAA Atmospheric Flight Mechanics Conference*, AIAA, Portland, Oregon, Aug 2011, p. 6368.

[21] Li, H., Zhao, Y., and Hu, H., "Adaptive Maneuver Load Alleviation via Recurrent Neural Networks," *Journal of Guidance, Control, and Dynamics*, Vol. 40, No. 7, 2017, pp. 1824–1831.

[22] Yagil, L., Raveh, D. E., and Idan, M., "Deformation Control of Highly Flexible Aircraft in Trimmed Flight and Gust Encounter," *Journal of Aircraft*, Vol. 55, No. 2, 2018, pp. 829–840.

[23] García, C. E., Prett, D. M., and Morari, M., "Model Predictive Control: Theory and Practice—A Survey," *Automatica*, Vol. 25, No. 3, 1989, pp. 335–348.

[24] Giesseler, H.-G., Kopf, M., Varutti, P., Faulwasser, T., and Findeisen, R., "Model Predictive Control for Gust Load Alleviation," *4th IFAC Nonlinear Model Predictive Control Conference*, Aug 2012, pp. 27–32.

[25] Kopf, M., Bullinger, E., Giesseler, H.-g., Adden, S., and Findeisen, R., "Model Predictive Control for Aircraft Load Alleviation: Opportunities and Challenges," *2018 Annual American Control Conference (ACC)*, Milwaukee, USA, 2018, pp. 2417–2424.

[26] Haghighat, S., Liu, H. H. T., and Martins, J. R. R. A., "Model-Predictive Gust Load Alleviation Controller for a Highly Flexible Aircraft," *Journal of Guidance, Control, and Dynamics*, Vol. 35, No. 6, 2012, pp. 1751–1766.

[27] Wang, Y., Wynn, A., and Palacios, R., "Model-Predictive Control of Flexible Aircraft using Nonlinear Reduced-Order Models," *AIAA Scitech 2016 Forum*, Jan 2016, p. 0711.

[28] Krag, B., Rohlf, D., and Wunnenberg, H., "OLGA. A Gust Alleviation System for Improvement of Passenger Comfort of General Aviation Aircraft," *Proceedings of the 12th Congress of the International Council of the Aeronautical Sciences (ICAS)*, Munich, Germany, Oct 1980, pp. 219–231.

[29] Rabadan, G. J., Schmitt, N. P., Pistner, T., and Rehm, W., "Airborne Lidar for Automatic Feedforward Control of Turbulent In-Flight Phenomena," *Journal of Aircraft*, Vol. 47, No. 2, 2010, pp. 392–403.

[30] Vrancken, P. S., "Airborne Remote Detection of Turbulence with Forward-Pointing LIDAR," *Aviation Turbulence: Processes, Detection, Prediction*, Springer International Publishing, Cham, 2016, pp. 443–464.

[31] Fezans, N., Joos, H.-D., and Deiler, C., "Gust Load Alleviation for a Long-Range Aircraft with and without Anticipation," *CEAS Aeronautical Journal*, Vol. 10, No. 4, 2019, pp. 1033–1057.

[32] Johansen, T. A. and Fossen, T. I., "Control Allocation—a Survey," *Automatica*, Vol. 49, No. 5, May 2013, pp. 1087–1103.

[33] Zaccarian, L., "Dynamic Allocation for Input Redundant Control Systems," *Automatica*, Vol. 45, No. 6, Jun 2009, pp. 1431–1438.

[34] Durham, W., Bordignon, K. A., and Beck, R., *Aircraft Control Allocation*, John Wiley & Sons, Ltd, Chichester, UK, Dec 2016.

[35] Frost, S. A., Bodson, M., Burken, J. J., Jutte, C. V., Taylor, B. R., and Trinh, K. V., "Flight Control with Optimal Control Allocation Incorporating Structural Load Feedback," *Journal of Aerospace Information Systems*, Vol. 12, No. 12, 2015, pp. 825–835.

[36] Miller, C. J. and Goodrick, D., "Optimal Control Allocation with Load Sensor Feedback for Active Load Suppression, Experiment Development," *AIAA Guidance, Navigation, and Control Conference*, 2017, p. 1719.

[37] Gaulocher, S. L., Roos, C., and Cumer, C., "Aircraft Load Alleviation During Maneuvers Using Optimal Control Surface Combinations," *Journal of Guidance, Control, and Dynamics*, Vol. 30, No. 2, 2007, pp. 591–600.

[38] Pereira, M. d. V., Kolmanovsky, I., Cesnik, C. E. S., and Vetrano, F., "Model Predictive Control Architectures for Maneuver Load Alleviation in Very Flexible Aircraft," *AIAA Scitech 2019 Forum*, Jan 2019, p. 1591.

[39] Hashemi, K. E. and Nguyen, N. T., "Adaptive Maneuver Load Alleviation for Flexible Wing Aircraft with Nonminimum Phase Zeros," *2018 AIAA Guidance, Navigation, and Control Conference*, 2018, p. 619.

[40] Cocetti, M., Serrani, A., and Zaccarian, L., "Dynamic Input Allocation for Uncertain Linear Over-actuated Systems," *2016 Annual American Control Conference (ACC)*, Boston, USA, Jul 2016, pp. 2906–2911.

[41] Duan, M. and Okwudire, C., "Proxy-Based Optimal Dynamic Control Allocation for Multi-Input, Multi-Output Over-Actuated Systems," *Proceedings of the ASME 2017 Dynamic Systems and Control Conference*, ASME, Tyson, VA, Oct 2017, p. V001T03A005.

[42] Duan, M. and Okwudire, C., "Proxy-Based Optimal Control Allocation for Dual-Input Over-Actuated Systems," *IEEE/ASME Transactions on Mechatronics*, Vol. 23, No. 2, 2018, pp. 895–905.

[43] Cesnik, C. E. S., Senatore, P. J., Su, W., Atkins, E. M., and Shearer, C. M., "X-HALE: A Very Flexible Unmanned Aerial Vehicle for Nonlinear Aeroelastic Tests," *AIAA Journal*, Vol. 50, No. 12, 2012, pp. 2820–2833.

[44] Karpel, M., Shousterman, A., Maderuelo, C., and Climent, H., "Dynamic Aeroservoelastic Response with Nonlinear Structural Elements," *AIAA Journal*, Vol. 53, No. 11, 2015, pp. 3233–3239.

[45] Diederich, F. W., "Response of an Airplane to Random Atmospheric Disturbances," Tech. Rep. TN3910, NACA, Apr 1957.

[46] Duan, M. and Okwudire, C. E., "Connections between Control Allocation and Linear Quadratic Control for Weakly Redundant Systems," *Automatica*, Vol. 101, 2019, pp. 96–102.

[47] FAA, *Title 14 of the Code of Federal Regulations: Aeronautics and Space PART 25*, Government Publishing Office, Washington, DC, Dec 1964.

[48] MATLAB, *version 9.0.0 (R2016a)*, The MathWorks Inc., Natick, Massachusetts, 2016.

[49] MATLAB, “Simulink Aerospace Blockset, Environment, Wind,” `https://www.mathworks.com/help/aeroblks/wind.html?s_tid=CRUX_lftnav`, Nov 2020.

[50] Oppenheimer, M. W., Doman, D. B., and Bolender, M. A., “Control Allocation,” *The Control Handbook*, edited by W. S. Levine, chap. 8, CRC Press, Boca Raton, 2nd ed., 2010, pp. 8–24.

[51] Yildiz, Y. and Kolmanovsky, I., “Stability Properties and Cross-Coupling Performance of the Control Allocation Scheme CAPIO,” *Journal of Guidance, Control, and Dynamics*, Vol. 34, No. 4, 2011, pp. 1190–1196.

[52] Kailath, T., *Linear Systems*, Vol. 156, Prentice-Hall Englewood Cliffs, NJ, 1980.

[53] Bareiss, E. H., “Numerical solution of linear equations with Toeplitz and Vector Toeplitz matrices,” *Numerische Mathematik*, Vol. 13, 1969, pp. 404–424.

[54] Cesnik, C. E. S. and Su, W., “Nonlinear Aeroelastic Simulation of X-HALE: a Very Flexible UAV,” *49th AIAA Aerospace Sciences Meeting Including the New Horizons Forum and Aerospace Exposition*, 2011, p. 1226.

[55] Pang, Z. Y., *Modeling, Simulation and Control of Very Flexible Unmanned Aerial Vehicle*, Ph.D. thesis, University of Michigan, Ann Arbor, 2018.

[56] Lupp, C., *Inclusion of Geometrically Nonlinear Aeroelastic Effects into Gradient-Based Aircraft Optimization*, Ph.D. thesis, University of Michigan, Ann Arbor, 2020.

[57] Sanghi, D., Riso, C., Cesnik, C. E. S., and Vetrano, F., “Impact of Control-Surface Flexibility on the Dynamic Response of Flexible Aircraft,” *AIAA Scitech 2020 Forum*, Jan 2020, p. 1185.

[58] MATLAB, *version 9.8.0 (R2020a)*, The MathWorks Inc., Natick, Massachusetts, 2010.

[59] Easton, R., *Fourier Methods in Imaging*, The Wiley-IS&T Series in Imaging Science and Technology, Wiley, 2010.

[60] Burlion, L., Poussot-Vassal, C., Vuillemin, P., Leitner, M., and Kier, T., “Longitudinal Manoeuvre Load Control of a Flexible Large-Scale Aircraft,” *19th World Congress - The International Federation of Automatic Control (IFAC)*, IFAC, Cape Town, South Africa, Aug 2014, pp. 3413–3418.